Julius-Maximilians-
UNIVERSITÄT
WÜRZBURG

UNIVERSITÄT WÜRZBURG
PHYSIKALISCHES INSTITUT
epVI

Quantum Sensing with Highly Coherent Spin Centers in Silicon Carbide

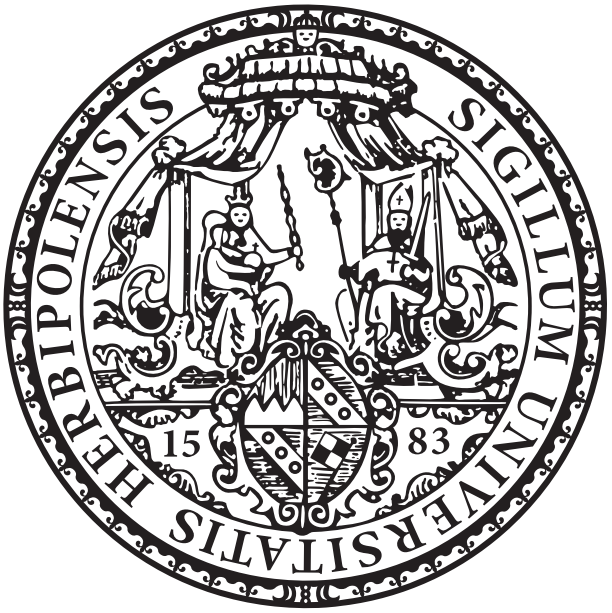

Dissertation zur Erlangung
des naturwissenschaftlichen Doktorgrades
der Julius-Maximilians-Universität Würzburg

vorgelegt von
Dmitrij Simin
aus Jekaterinburg

Würzburg, 2017

Eingereicht am 28. Juni 2017
bei der Fakultät für Physik und Astronomie

1. Gutachter: Prof. Dr. Vladimir Dyakonov
2. Gutachter: Prof. Dr. Peter Jakob
der Dissertation.

Vorsitzende(r)

1. Prüfer: Prof. Dr. Vladimir Dyakonov
2. Prüfer: Prof. Dr. Peter Jakob
3. Prüfer: Prof. Dr. Björn Trauzettel
im Promotionskolloquium.

Tag des Promotionskolloquiums: 29.11.2017

Doktorurkunde ausgehändigt am

Contents

1. Introduction

For already over two decades, quantum information processing has been the hot topic in the field of information theory. While great progress was achieved, both on the theoretical and experimental field, to recognize and to employ the most suitable material and information carrier from the vast amount of possibilities is still the main goal of ongoing research activities all over the world. Whereas a wide availability and easy handling are crucial for an industrial manufacturing of devices, long-preserving spin coherence is the major prerequisite for such a system.

The NV-center -a nitrogen atom substituting a carbon atom, plus an adjacent lattice vacancy- in diamond has been leading the headlines of solid-state based quantum processing for the last years [1], pushing the coherence time [2] and manipulation possibilities [3] steadily further, ultimately reaching a coherence time of 600 milliseconds by utilizing the optically detected magnetic resonance (ODMR) technique [4]. Consequently, the NV-center shows an exceptional performance in the already established new generation magnetometers [5, 6, 7, 8], bio-sensors [9, 10] and single-photon sources [11].

While having impressive quantum-mechanical properties, making the NV defect in diamond almost the ideal qubit, the fabrication process of both the diamond wafers, as well as of diamond devices is still a challenging and cost-consuming task. Therefore, a material system with the advantages of diamond, but more versatile and industrially accessible could once again revolutionize the field of quantum processing [12].

The point defects in silicon carbide are very promising candidates for this task: with over 250 known polytypes and an even larger variety of defects [13], it seems to have a proper configuration for every demand. In recent years, SiC is attracting continuously growing interest as a technologically perspective platform for quantum spintronics [14, 15] with the ability for single spin engineering and control [16, 17], as well as for creation of single-photon sources [18]. The V_{Si} defect, i.e. a silicon vacancy, is one of the best examples: While emitting in the easily detectable near infrared range, the spins can be manipulated via radio frequencies in the MHz range [19]. Using the ODMR technique, spin control has been successfully conducted at ambient conditions [17, 20, 21] and the potential of this defect as a temperature sensor, as well as a magnetic field sensor have been demonstrated [22] by our group.

For this reasons, the following thesis is dedicated to the task to reinforce the V_{Si} defect in SiC as a system perfectly suitable for various quantum applications. By the means of the ODMR technique, the true energetic structure of the defect will be revealed for the first time (Chapter 4.2), enabling novel implementations in the field of quantum metrology. Also, two magnetometry schemes (Chapters 4.1 and 4.3) utilizing the unique properties of the V_{Si} defect will be introduced and quantitatively analyzed in regard to achievable resolution and implementation. Furthermore, a protocol for temperature sensing will be elaborated (Chapter 4.4), allowing for simultaneous magnetometry and thermometry.
On the other hand, the crucial determination of achievable spin coherence times will be thoroughly conducted by pulsed ODMR. The relaxation times will be analyzed in dependence on the ambient conditions, i.e. an external magnetic field and temperature (Chapter 5.1). Furthermore, the dependence of the coherence on the defect origin and density (Chapter 5.2), which is decisive for industrial implementation, where a perfect balance between signal-to-noise ratio and sensitivity must be achieved, is analyzed.
Last but not least, a substantial prolongation of the coherence time up to 75 milliseconds by means of spin-locking is achieved (Chapter 5.3), making the V_{Si} defect in silicon carbide quite competitive to the already established quantum systems.
Finally, it is not the aim of this thesis to excel the values of the NV-center, but to introduce a higher-than-average alternative quantum system with exceedingly good coherence properties, a much more cost-efficient production potential and a wide-spread implementation in a technologically useful material.
Before the presentation of the results, the material silicon carbide will be introduced. Also, the occurring defects are described, with the focus on the silicon vacancy. Subsequently, the technical properties of the ODMR technique are established.

2. Silicon Carbide and Defects

End of the 19th century, American inventor Edward G. Acheson was the first to successfully synthesize silicon carbide [23]. Since then, it has been subject of extensive research. Though the natural occurrence is confirmed only in some types of meteorites [24], due to its excellent mechanical and electrical robustness, high thermal conductivity and a wide bandgap, silicon carbide is nowadays utilized in a very broad application range [25]. From automobile parts [26], to high-power electronic devices [27]: silicon carbide is an essential component in modern electrical engineering and electronics. The high stability of the covalent Si-C bonding makes SiC resistant to chemicals, radiation, high temperatures and other extreme conditions [28]. Recognizing these advantages, the European Space Agency ESA fabricated the primary mirror for its Herschel's space telescope from silicon carbide [29]. Due to a well established wide-scale manufacturing process [30], and hence competitive production costs, silicon carbide is becoming a feasible alternative to the market leader silicon [31].
In Table 2.1 distinct properties of silicon carbide are listed, along with the attributes of its "direct relatives" silicon and diamond.

	Silicon [32]	Silicon carbide [25]	Diamond [33]
Hardness [Mohs]	6	9	10
Thermal conductivity [$Wcm^{-1}K^{-1}$]	1.5	4.9	23.1
Breakdown field [$10^5\,Vcm^{-1}$]	3	20 - 30	
Band gap [eV] (indirect)	1.1	2.4 - 3.3	5.4

Table 2.1.: Comparison of physical parameters of silicon, silicon carbide and diamond. The SiC-values are polytype dependent.

2.1. Crystallographic Characterization

Silicon carbide is a material consisting of silicon and carbon atoms, bonded to a tetrahedral structure by sp^3 hybrid orbitals. In order to compose a macroscopic crystal, one imagine hexagonal layers with a two atomic basis (one Si and one C atom) stacked over each other, as depicted in Figure 2.1. If a layer is to be put in the dents of the previous one, there are two non-equivalent stacking possibilities to do that: if the first layer is in position A, the second one can take positions B or C, in accord with Figure 2.1b. Assuming, the second layer settles to position B, there are again two options for the third layer, A and C. This variability of the stacking order evolves into one of the distinguishing properties of silicon carbide, its polytypism. While a single layer has always a hexagonal structure with a two atomic base, the stacking sequence along the symmetry axis of the layers (c-axis) is decisive for the physical properties of the material [34].

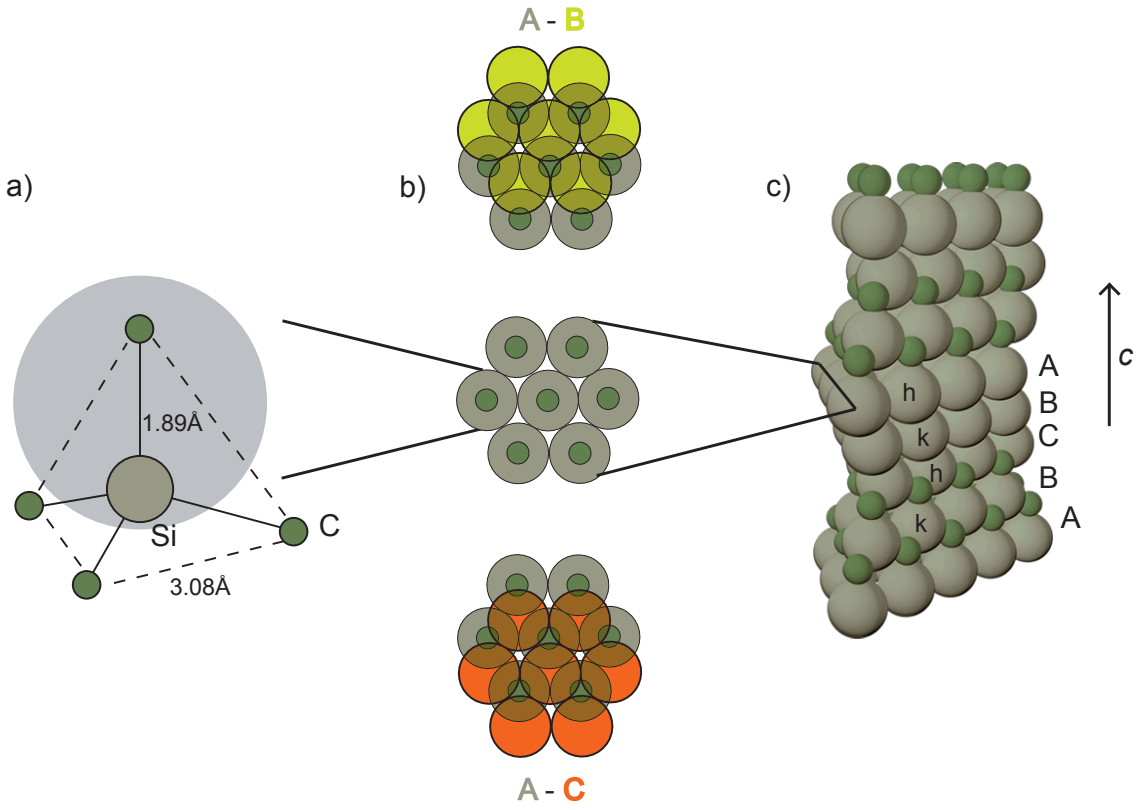

Figure 2.1.: a) Every silicon atom is surrounded by four carbon atoms and vice versa, establishing a tetrahedral structure. A two atomic basis with one silicon and one carbon atom (gray, transparent circle) is defined. b) A crystal is built out of layers with a hexagonal structure, with every new layer having two different positioning options, here B and C. c) The 4H-SiC polytype consists of layers with an ABCB stacking sequence along the c-axis. The two non-equivalent crystallographic positions are denoted as k for cubic and h for hexagonal environment.

There are more than 250 known polytypes, which are classified according to the Ramsdell notation [13, 35]: in order to describe a specific SiC type, the number of layers after which the sequence repeats is declared together with the present crystal structure. The latter can be cubic, hexagonal or rhomboidal. The three most common polytypes -due to simple and well established manufacturing processes- are 3C-, 4H- and 6H-SiC. Hence, 3C-SiC is a cubic crystal system (C), which stacking order repeats after every three layers (ABC). 4H- and 6H-SiC are hexagonal systems with a sequence of four (ABCB) and six (ABCACB) layers, respectively [36].
All polytypes have slightly different properties (e.g. bandgap width) [25] and since all the measurements presented in this work were conducted on 4H-SiC crystals, we will focus on this polytype from now on. Its crystal structure is depicted in Figure 2.1c. The crystal has an indirect band gap of 3.23 eV [34].
Due to the alternating stacking sequence, a silicon atom can be located at two non-equivalent crystallographic positions, which are surrounded by the same amount of next nearest neighbors (carbon atoms), but differ in the number of and the distance to the next-but-one neighbors. Thus, a Si-C bilayer can be either in a locally cubic (k, German for kubisch) or a locally hexagonal (h) environment, in dependence to its position within the sequence [13, 25, 37]. Both positions are denoted in Figure 2.1c.
Hence, there are also two distinct sites for creation of silicon vacancies, the point defect of interest in this work. In the following chapter, the attributes of these defects are characterized.

2.2. Point Defects

As for every crystal, there is a variety of different imperfections that can occur in SiC during the crystallization. Structural defects like voids (3D), stacking faults (2D) and dislocations (1D) influence the electrical and mechanical performance of the material and are crucial for device engineering [38, 39].
In our investigations, however, we are interested in zero dimensional point defects, i. e. localized imperfections at or around one single lattice site. These can be of extrinsic or intrinsic nature. In the first case, an element unrelated to the material is involved, like the ever-present nitrogen atom in SiC [40].
The impurity is often introduced on purpose as a dopand, to modify the electrical properties of the crystal [41]. The NV-center in diamond is a prominent example of such an extrinsic defect.
An intrinsic defect, on the other hand, does not consist of a foreign atom, but embodies a displacement of a present one.

This might lead to one of the four basic kinds of intrinsic defects [42]:

- A carbon or silicon vacancy, where an atom is missing at its initial lattice site (Schottky defect);
- An interstitial, where an atom is located between the lattice positions;
- A bound vacancy-interstitial pair, mostly occurring when an atom breaks out of its lattice site and stays in the near environment (Frenkel pair);
- An antisite, where an atom occupies the site of an another atom, e.g. carbon on a silicon site or vice versa.

Also, compositions of these forms are possible, like a divacancy or a vacancy-antisite pair [43]. Bearing the polytypism of SiC in mind, there is seemingly an infinite amount of different point defect configurations with different attributes [44].
While the structural defects described in the beginning of the chapter are aimed to be avoided [45], the point defects often introduce unique beneficial properties to the material, which are utilized in a broad range of applications. Hence, despite being created in some amount during the growth of the crystal, they are also purposefully introduced into the crystal through irradiation, e.g. with neutrons or electrons. This will be described in detail in Chapter 5.2. In most cases, point defects introduce deep levels to the energy gap, allowing absorption of additional light and making investigations via optical spectroscopy possible. These defects are also called color centers, since the color of the crystal changes due to additional light absorption. In Figure 2.2, a pristine and a heavily doped SiC crystals are depicted.

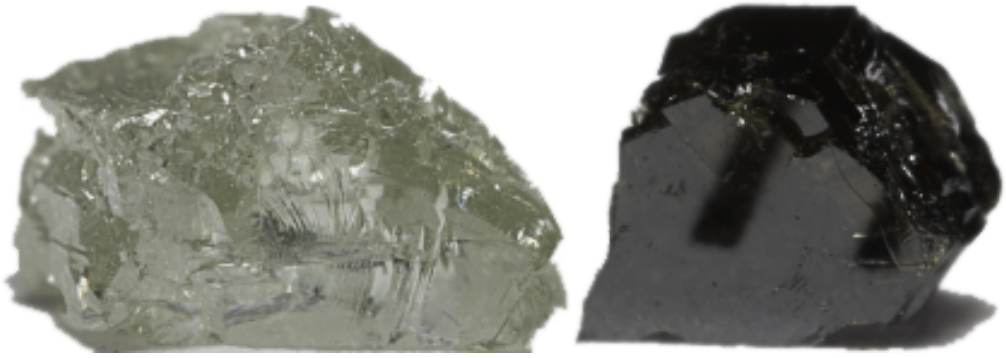

Figure 2.2.: While a pristine silicon carbide crystal (left) is transparent, creating point defects changes it to opaque. Photo made by Klaus Kister.

Point defects are used among others as bio-sensors, single-photon sources as well as magnetic field and temperature sensors [46].

As for bio-sensors, the biological inertness, non-toxicity and chemical stability of SiC ensures bio-compatibility [47], while the impurities enable the utilization as bio-marker, i.e. by embedding the crystal into the human body and monitoring the photoluminescence (PL) of the point defects [48, 49].
Especially in the fields of quantum communication and cryptography, single-photon sources are regarded as most necessary for further development [50]. The requirement for a successful implementation is creation of single defect centers that emit indistinguishable photons with a minimal probability of their bunching per time unit[51]. Recently, such a single-photon source from a point defect in SiC was demonstrated at room temperature [18].
The application of color centers in SiC as a magnetic field and temperature sensor constitutes a major part of this thesis and will be introduced and discussed in great detail in Chapter 4. The implementation was shown on a specific point defect, namely a silicon vacancy. Its distinct properties will be elaborated in the following chapter.

2.3. The Silicon Vacancy

The silicon vacancy (V_{Si}) is one of the simpler intrinsic defects, namely a missing silicon atom on the lattice site. A scheme of such a vacancy and its nearest environment are depicted in Figure 2.3a.

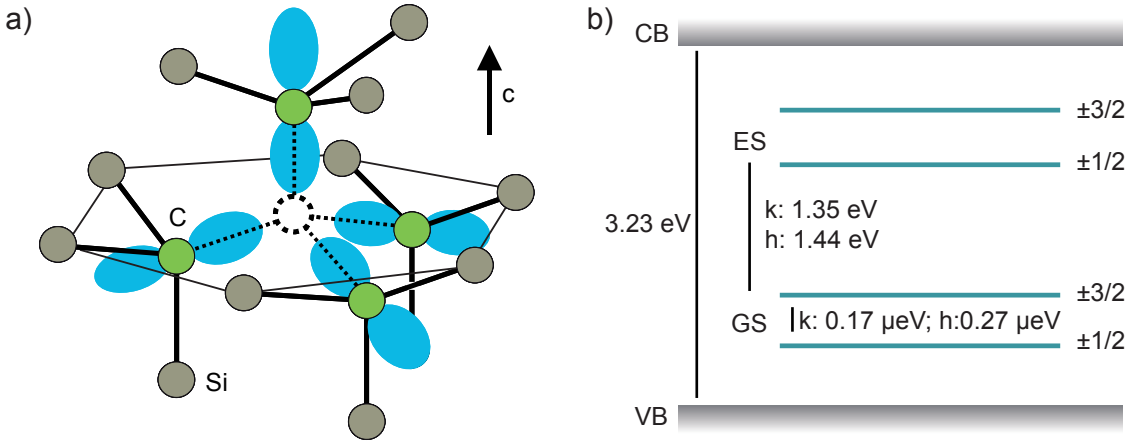

Figure 2.3.: a) Schematic of a silicon vacancy in a hexagonal (h) environment with the four sp^3 dangling bonds at the tetrahedral aligned carbon atoms (adapted from [52]). b) Energy diagram of the silicon vacancy embedded in a 4H-SiC crystal.

There are two non-equivalent crystallographic positions for a silicon vacancy in 4H-SiC: Due to the stacking sequence, there are layers with cubic and hexagonal environments, as denoted in Figure 2.1c, with k and h, respectively.

Hence, the defects introduced into each environment have slightly different properties, e.g. different energy gaps: 1.352 eV for k and 1.438 eV for h [53]. Therefore, the photoluminescence (PL), i.e. the radiative recombination of electrons after optical excitation from the ground state (GS) into the excited state (ES), lies in the near infrared [19].

In Figure 2.4, the photoluminescence of the two silicon vacancies at 4 Kelvin and room temperature is denoted, after an excitation with a 1.959 eV (633 nm) laser. In the spectrum at low temperature, the zero phonon lines (ZPL), i.e. the non-vibrational ES → GS transitions, are clearly pronounced as sharp lines. With increasing temperature, the interaction with crystal phonons increases, adding a wide-range radiation spectrum called the phononic sideband [14]. Also, the presence of several unmarked lines in the 4 K graph attests the creation of various other types of point defects during the crystal growth and/or irradiation.

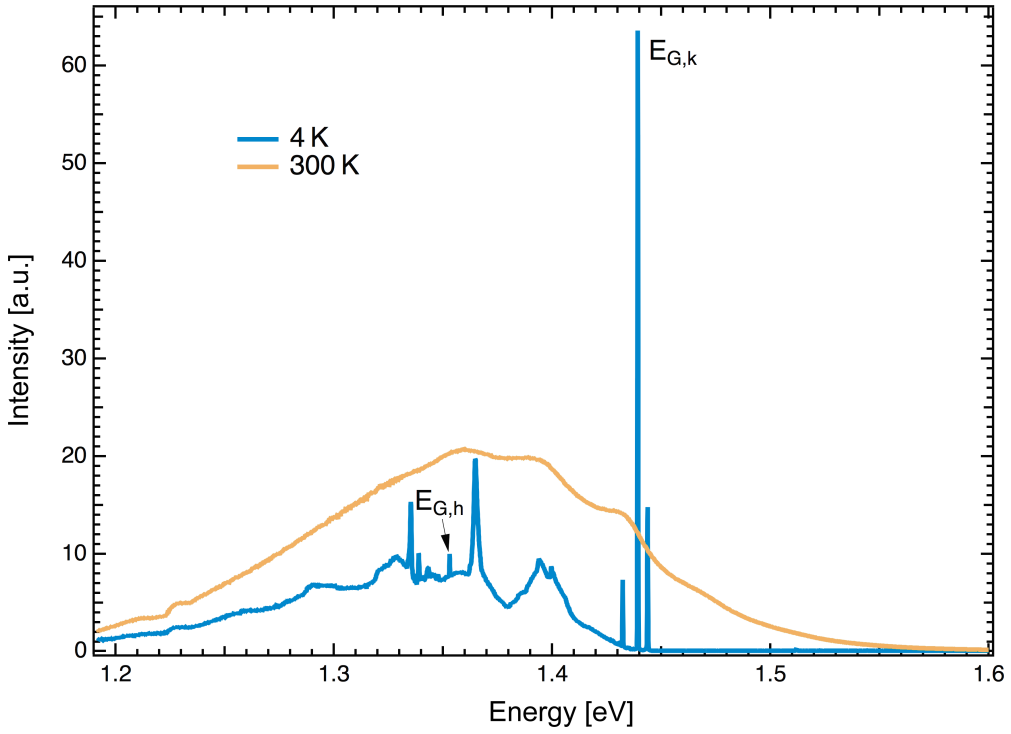

Figure 2.4.: Photoluminescence of an irradiated 4H-SiC sample at 4 K and 300 K, excited with a 1.959 eV laser. The ZPL $E_{G,k}$, $E_{G,h}$ of the V_{Si} defects are clearly distinguishable at 4K and disappear for 300K due to increased radiation from the phononic sideband, in accord with the Franck-Condon-principle [54].

An another distinct property of this defect is its spin state: As have been unambiguously proven by our group, the electron system of the optically active silicon vacancies possesses an overall spin of $S = 3/2$ [21]. As depicted in Figure 2.3a, a neutral silicon vacancy holds four electrons, coming from the four sp^3 dangling bonds of the surrounding carbon atoms [55].

This configuration leads to a $S = 1$ system, which means that the optically active V_{Si} with $S = 3/2$ must be negatively charged, with an additional electron coming for example from a nitrogen dopand [56].

As has been experimentally shown, the ground and exciting states of the V_{Si} are split by their magnetic quantum number into $M_S = \pm 3/2$ and $M_S = \pm 1/2$ states. This so called zero field splitting (ZFS) lies in the µeV range and is different for the two distinct crystallographic positions: 0.27 µeV for h and 0.17 µeV for k site [56].

The origin of ZFS is still under controversial debate: Mizuochi et al. ascribe its existence to a Jahn-Teller distortion and a consequent reduction of the group symmetry from C_{6v} to C_{3v}, which also has been proven experimentally [56]. Baranov et al. argue that a crystal field deformation by a near-by carbon vacancy along the c-axis is responsible for the lifted degeneracy[57]. Other groups see the many-electron effects as the main reason for the favored high spin state [58, 59].

Also, the value and the origin of the ZFS seems to be polytype dependent, which makes it even more complicated to create a general theory [52]. Nevertheless, the energetic favorization of the $\pm 1/2$ levels over the $\pm 3/2$ levels has been experimentally shown by Orlinski et al. [60] for the V_{Si} in 4H-SiC.

Luckily, this controversy does not affect the results obtained in this thesis, which will become clear in Chapter 3.

The so far discussed energetic properties of the negatively charged silicon vacancies in 4H-SiC are depicted in Figure 2.3b.

A crucial property of the negatively charged silicon vacancy in regard to our measurements is the occurrence of spin polarization of the ground state by optical excitation. This process will be described in detail in the following chapter.

2.3.1. Optical Pumping

As has been seen in experiments [14] and confirmed by theoretical calculations [59], negatively charged silicon vacancies exhibit a favored population of a spin state within the ground state under optical excitation. This is made possible by presence of metastable states (MS) between the ground states and excited states. Which state is favored, depends on the SiC polytype and the vacancy site; for the here discussed $V_{Si}(h)$ it is $M_S = \pm 1/2$ [14].

If an electron is excited (e.g. by laser light of suitable energy) from one of the GS spin levels into a corresponding ES (spin preservation holds), two relaxation mechanisms come into question, whose transition rates depend on the magnetic quantum number of the ES.

The direct luminescent relaxation is favored by the $M_S = \pm 3/2$, while non-luminescent relaxation into the MS is more probable from $M_S = \pm 1/2$. If an electron relaxes subsequently from MS to GS, inter-system crossing can take place, resulting in a preferred population of the $M_S = \pm 1/2$ ground state [21]. This optical cycle is depicted in Figure 2.5, with continuous lines representing luminescent transitions and dashed lines the non-luminescent ones. The thickness of the lines symbolizes qualitatively the transition probability.

The here depicted spin alignment (preferred population of the $\pm 1/2$-state) and the spin state dependent luminescence, are the basis for our measurement technique, namely the optically detected magnetic resonance, whose principles will be elaborated in Chapter 3. Before that the most important statements will be recapped.

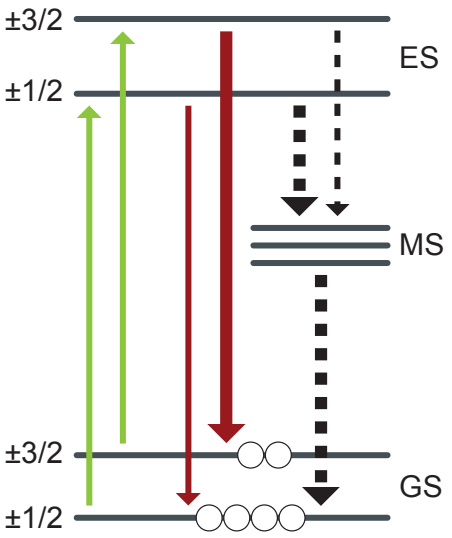

Figure 2.5.: Energy diagram of $V_{Si}(h)$ with possible transitions after excitation (green arrows). The red solid lines represent luminescent transitions, while gray dashed lines denote non-luminescent relaxation via metastable states and occurring inter-system crossing. The transition rates are coded by the line width.

2.4. Silicon Carbide and Defects: Summary

So far, silicon carbide has been introduced as an appealing host for point defects, with a focus on the negatively charged silicon vacancy in a 4H-SiC polytype, with which quantum sensing and other applications are possible.
As a final summary, the key points are listed:

- Wide-scale production of high quality SiC wafers is well established and hence cost-effective.
- The excellent mechanical and electrical properties, like high robustness, thermal conductivity and breakdown field make silicon carbide to a perfect material for high-power electronics and other applications in extreme conditions.
- Due to a vast amount of different polytypes with distinct properties, a high degree of flexibility is ascertained.

- The intrinsic nature of the negatively charged silicon vacancy ensures a simple and straightforward creation via irradiation with neutrons or electrons, which can even be accomplished by an electron microscope.
- Due to distinct energetic properties of V_{Si}, which vary with the polytype and defect site, a quantum point with suitable attributes for a certain application can be found.
- The emission spectrum of V_{Si} lies in the near infrared range, making it suitable for processing via fiber-optic communication as well as for utilization as biomarker. Furthermore, optical excitation and read-out with widespread technology is possible.
- The optically active, negatively charged silicon vacancy possesses an overall spin of $S = 3/2$, with the $M_S = \pm 1/2$ as well as the $M_S = \pm 3/2$ levels being degenerated. As described by the Kramers theorem, the energetic states of a half-integer spin system remains at least doubly degenerate in presence of purely electric fields [61]. Hence, the degenerate spin levels of the V_{Si} cannot be further split by strain or other mechanical influences, which would alter the crystal field.
- Due to the zero field splitting between the $M_S = \pm 3/2$ and $M_S = \pm 1/2$ spin states lying in the convenient MHz range, and the spin alignment in the $M_S = \pm 1/2$ state via optical pumping, measurements by optically detected magnetic resonance can be conducted.

All in all, from the properties listed above it is evident that the silicon vacancy in silicon carbide deserves a closer look in regard to its potential for quantum sensing and other quantum applications.

3. Optically Detected Magnetic Resonance

The distinct properties of V_{Si}, especially its spin state, can be analyzed and utilized in a convenient way by optically detected magnetic resonance. This technique will be introduced in the following on exemplary measurements.

3.1. Basic Principles

Optically detected magnetic resonance can be regarded as a subset of the electron paramagnetic resonance (EPR), which, together with nuclear magnetic resonance (NMR) belong to the family of magnetic resonance techniques. While having some similarities to the other two, ODMR is an indirect detection method, meaning that the spin state is concluded from the detection of spin sensitive photoluminescence.
Here, the main properties of the measurement technique will be presented on the concrete example of the $V_{Si}(h)$ in 4H-SiC, the defect of interest in this thesis. In contrast to the well established high-field (hf-) ODMR, which relies on a strong external magnetic field and is elaborated in [62], in this work, only zero field ODMR and low field ODMR are utilized.
The basis of ODMR is the measurement of photoluminescence, which evolves from the luminescent relaxation of the electrons, after being lifted from the ground state into the excited state. By continuous optical pumping, the spins align in the $M_S = \pm 1/2$ GS, as depicted in Figure 2.5. From the same Figure it is evident, that the luminescent relaxation into the $M_S = \pm 3/2$ GS is more probable than into $M_S = \pm 1/2$ GS. Therefore, if one is transferring an electron from the favorably populated $M_S = \pm 1/2$ GS into the $M_S = \pm 3/2$ GS, there are more electrons relaxing via the luminescent path in the subsequent pumping cycle. By monitoring the photoluminescence, one ought to detect an increase in luminescent emission. This electron transition between the GS spin states can be executed by applying radio waves (RF) to the sample, whose frequency corresponds to the zero field splitting. For the $V_{Si}(h)$ defect, it has a value of around ZFS = 0.27 µeV, which corresponds to around 70 MHz [60].

This change in photoluminescence is the quantity detected by ODMR: Ensuring continuous optical pumping, the photoluminescence is monitored, while the radio frequency is swept in an iterative manner. When the radio frequency hits the resonance condition RF = ZFS, a change in emission intensity is detected.

This is the main difference to EPR, where absorption or emission of radio waves is detected directly. While the ODMR contrast does depend on radio wave energy, the signal is created by changing the number of electrons, participating in the luminescent relaxation cycle of the pumping process.

In a typical ODMR graph, the relative change in photoluminescence ΔPL/PL is plotted against the applied radio frequency. The outcome of such an exemplary measurement is depicted in Figure 3.1. Beside the main peak at around 70 MHz, there are also two satellite peaks at distances of circa ±5 MHz to the main peak.

These result from the hyperfine splitting of the ground states due to the interaction of the defect electron spins with the nucleus spin of the neighboring ^{29}Si isotope. This property is stated here to clarify the signal in Figure 3.1, and will be elaborated further in Chapter 3.3.

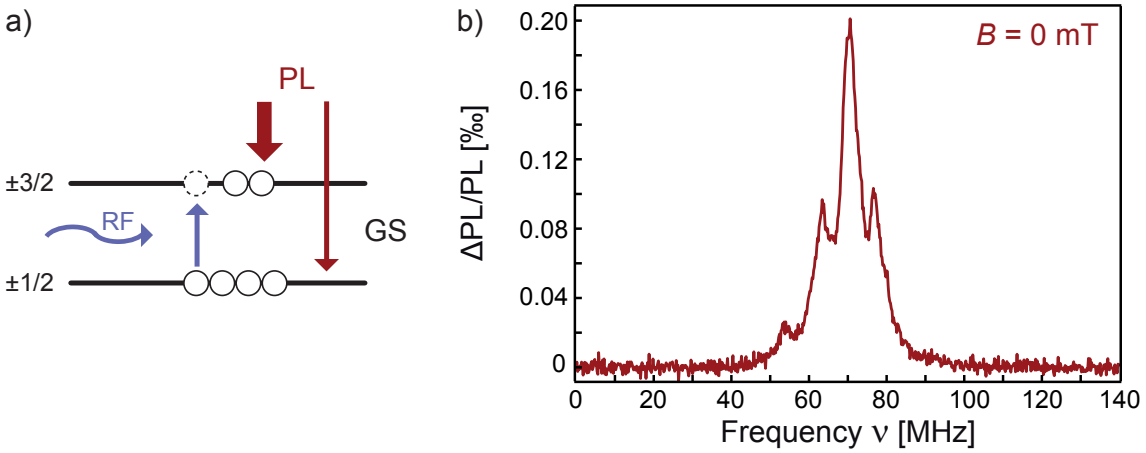

Figure 3.1.: a) By applying resonant radio waves, an energetic transition of the electrons can be induced over the ZFS from the pumped $M_S = \pm 1/2$ GS state into the $M_S = \pm 3/2$ GS state, resulting in a change of photoluminescence. b) If the detected change in radiation intensity is plotted against the frequency of radio waves, one sees a resonant peak at RF = ZFS.

One of the main utilizations of ODMR on silicon vacancies described in this thesis is the magnetic field sensing. Therefore, the behavior of the signal with a static external magnetic field will be explained in the following.

3.2. Evolution with the Magnetic Field

In this chapter, the behavior of the energy states and consequently of the ODMR spectra is described in dependence on an external magnetic field B along the c-axis of the crystal, since this alignment is relevant for all measurements and results of this thesis. The effect of general B-field alignment and its sensing technique will be discussed in the corresponding results chapter.

If the V_{Si} defect is influenced by an external magnetic field B, the degeneracy of the $M_S = \pm 1/2$ and the $M_S = \pm 3/2$ states is lifted by the Zeeman effect [63]. If B is aligned along the c-axis of the crystal, which is also the symmetry axis of the V_{Si} defect, the energetic levels split linearly with the magnetic field strength. The additional energy E_{Zeeman} can be described as follows:

$$E_{Zeeman}^{M_S} = g_e \mu_B B \cdot M_S, \tag{3.1}$$

with $g_e = 2$ being the Landé-factor of the electrons and μ_B the Bohr-magneton.

From this it follows that the splitting of the $M_S = \pm 3/2$ states is three times larger than the splitting of the $M_S = \pm 1/2$ states. This is depicted in Figure 3.2a.

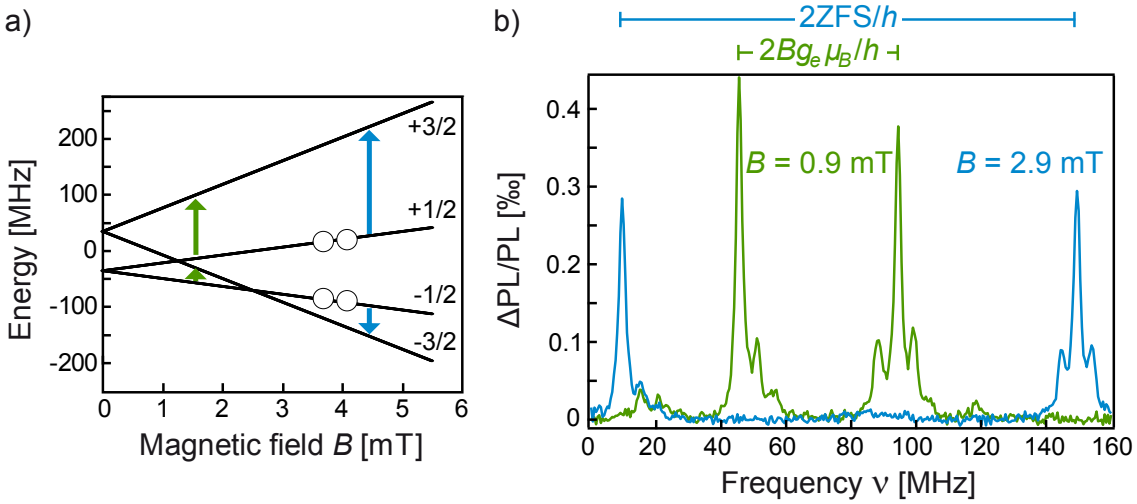

Figure 3.2.: a) Zeeman splitting of the primary degenerate $M_S = \pm 1/2$ and $M_S = \pm 3/2$ states in an external magnetic field B along the c-axis. By applying resonant radio waves two allowed transitions with $\Delta M_S = \pm 1$ can be induced for every B. b) For every magnetic field there are two ODMR peaks with distinct spectral positions, from which the magnetic field strength can be calculated.

It is important to note that while all four spin states have different energies, it does not affect the pumping cycle of the defect: In $V_{Si}(h)$ the spins are still aligned into the (not any more degenerate) $M_S = \pm 1/2$ states, with the electrons spread according to Boltzmann-distribution between these two levels [20].

If ODMR measurements are conducted, a change in photoluminescence is expected every time the radio frequency is resonant with a spin flip $\Delta M_S = \pm 1$. The corresponding transition energy ΔE for $M_{S,1} \rightarrow M_{S,2}$ can be described as follows:

$$\Delta E = \text{ZFS} + (M_{S,2} - M_{S,1}) \cdot g_e \mu_B B = \text{ZFS} \pm 1 \cdot g_e \mu_B B. \tag{3.2}$$

Therefore, the resonance condition is:

$$h\nu_{RF} \stackrel{!}{=} \left|\Delta E_{2,1}\right|. \tag{3.3}$$

Here, ν_{RF} is the radio frequency and h the Planck constant.

If Equation 3.2 is inserted into Equation 3.3, one expects an ODMR signal at two different frequencies: one at

$$\nu_{RF}^{+1} = \left|\frac{\text{ZFS} + g_e \mu_B B}{h}\right|, \tag{3.4}$$

for the $1/2 \rightarrow 3/2$ transition and one at

$$\nu_{RF}^{-1} = \left|\frac{\text{ZFS} - g_e \mu_B B}{h}\right|, \tag{3.5}$$

for the $-1/2 \rightarrow -3/2$ transition.

Though the $-1/2 \leftrightarrow 1/2$ transition has also $\Delta M_S = 1$, it cannot be detected with the ODMR technique, since on the one hand the states are almost equally populated via pumping, and on the other hand the luminescent relaxation rates to the $M_S = \pm 1/2$ GS states are the same. Hence, no change in photoluminescence is expected for this transition.

By Equations 3.4 and 3.5, as well as Figure 3.2a, the behavior of the two peak frequencies with changing magnetic field can be illustrated. The ν_{RF}^{+1} peak moves monotonously to higher frequencies, while the ν_{RF}^{-1} peak goes the opposite way, until it reaches zero at the intersection of the $-3/2$ and $-1/2$ levels (ZFS $= g_e \mu_B B$). From here, the $-1/2$ level lies above the $-3/2$ level, leading to induced emission of radio frequencies rather than absorption. This would cause a phase shift in an EPR spectrum, but does not affect the ODMR signal at all, since the pumping scheme as well as the photoluminescence rates stay unchanged. With further increase of the magnetic field, both peaks move towards higher frequencies in a spectral distance of $2 \cdot \text{ZFS}/h$, roughly 140MHz for the $V_{Si}(h)$ defect. In Figure 3.2b, two exemplary measurements are presented, one for $g_e \mu_B B < \text{ZFS}$ and one for $g_e \mu_B B > \text{ZFS}$. Therefore, the magnetic field strength B can be determined by means of ODMR from the spectral positions of the transitions.

3.3. Signal Composition

There are several contributions to the signal that have to be considered. For this reason, the attributes of the ODMR spectra in a magnetic field should be discussed now in more detail. The applied static magnetic field ensures that the ODMR peaks corresponding to different transitions are well separated and that magnetic disturbances, like peak broadening due to earth magnetic field, can be neglected. In Figure 3.3, the high frequency peak at $B = 3.5\,\mathrm{mT}$ is shown, along with a Gaussian and a Lorentzian fit curve. While both fitting curves describe the signal almost equally, which is in accord with earlier considerations [64], in both cases there are five contributing peaks. The shape of a single peak will be elaborated later in this chapter, but first the appearance of five peaks should be explained.

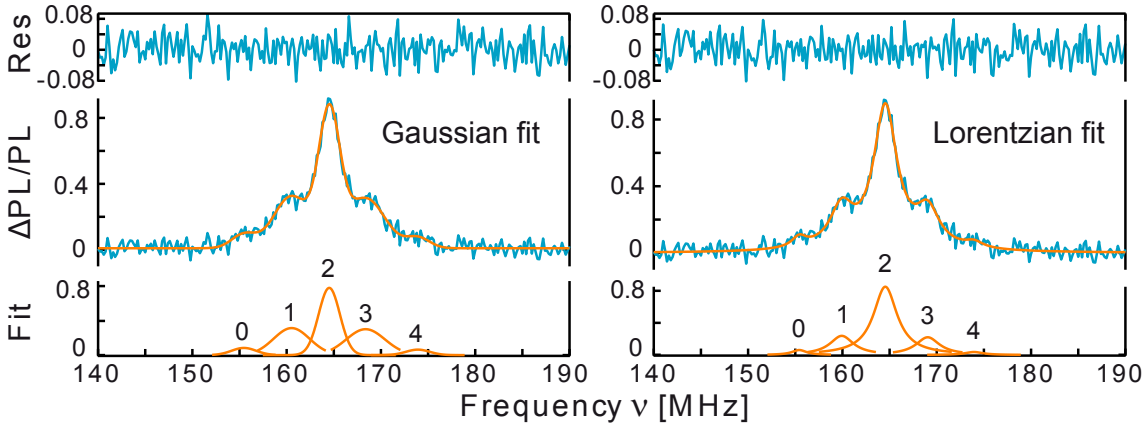

Figure 3.3.: High frequency ODMR signal at $B = 3.5\,\mathrm{mT}$, fitted with a Gaussian (left) and Lorentzian (right) function, consisting of five peaks.

The (Lorentzian) fit parameters of the five peaks are summed up in Table 3.1.

Peak (as in Figure 3.3)	Position [MHz]	Amplitude $\cdot 10^{-5}$	FWHM [MHz]
0	155.42 ± 0.27	0.61 ± 0.17	1.88 ± 0.83
1	159.93 ± 0.09	2.38 ± 0.11	3.05 ± 0.13
2	164.55 ± 0.03	8.51 ± 0.11	3.05 ± 0.13
3	169.04 ± 0.10	2.20 ± 0.11	3.05 ± 0.13
4	173.95 ± 0.50	0.36 ± 0.15	2.32 ± 1.58

Table 3.1.: Parameter of the Lorentzian fits for the high frequency signal at $B = 3.5\,\mathrm{mT}$.

As mentioned in Chapter 3.1, the origin of the satellite peaks lies in the hyperfine splitting of the $\pm 3/2$ and $\pm 1/2$ states. While the majority of the silicon atoms in a crystal are ^{28}Si with zero spin, around 4.7% of the silicon atoms are ^{29}Si isotopes, which have one more neutron and hence a nuclear spin $I = 1/2$.
If one of the twelve Si atoms around the vacancy is a ^{29}Si isotope, the electron spin and the nuclear spin with $M_I = \pm 1/2$ interact, which results in an energy shift [65]. Spin-spin interaction with isotopes that are further away can be neglected, since the interaction strength scales with distance as $1/r^3$ [66].
Hence, depending on the relative alignment of the M_S and M_I of the electronic and nuclear spins, as well as on the amount of contributing nuclei n, the corresponding energy level E_{M_S} of the vacancy is lifted or lowered by an energy hf_{M_S}.
From an interaction with n equivalent nuclei, there are $(2nI+1)$ possible, energetically diverse transitions [56]. These energy shifts are depicted in Figure 3.4, for the relevant case of $n = 1$, $I = 1/2$ and $S = 3/2$.
From the diagram it is evident that for $n = 1$ the $1/2 \rightarrow 3/2$ transition is contributing two signals at an energetic distance $\pm(hf_{3/2} - hf_{1/2})$ relative to the $n = 0$ case. For $n = 2$, three peaks are expected, due to the three possible alignments of the two ^{29}Si spins $M_{I,1} + M_{I,2} \in \{-1, 0, +1\}$. Two of them are at a doubled distance as for $n = 1$ and the third one is at the position of the $n = 0$ peak. As listed in Table 3.1 the inner peaks 1 and 3 are separated by circa 4.6 MHz from the main peak 2. The outer peaks 0 and 4 have a two times larger spectral distance to each other than peaks 1 and 3. These spectral values are in good agreement with previously reported ones in [37, 56] where these splittings are ascribed to presence of one and two ^{29}Si isotopes.
For an unambiguous identification, the measured relative intensities of the satellite peaks in regard to the main peak have to match the theoretical probability to find one or two ^{29}Si atoms among the 12 Si atoms next to the defect. As has been calculated in previous work [67], the relative intensity ought to be 0.2730 for $n = 1$ and 0.0369 for $n = 2$.
The relative intensities of the inner peaks 1 and 3 are calculated from Table 3.1 to 0.27 ± 0.01, and the ones for 0 and 4 to 0.038 ± 0.011, which coincides very well with the theoretical prediction.
All in all, the signal composition of five peaks can be unambiguously ascribed to the interaction with the ^{29}Si isotopes in the direct neighborhood of the vacancy.
Note, that in a SiC crystal also a natural abundance of the ^{13}C isotope of about 1.1% is expected, which might result in an additional splitting of the ODMR spectra. However, due to the small probability to be among the four nearest C atoms, this interaction cannot be resolved among the much more pronounced signals described above [56].

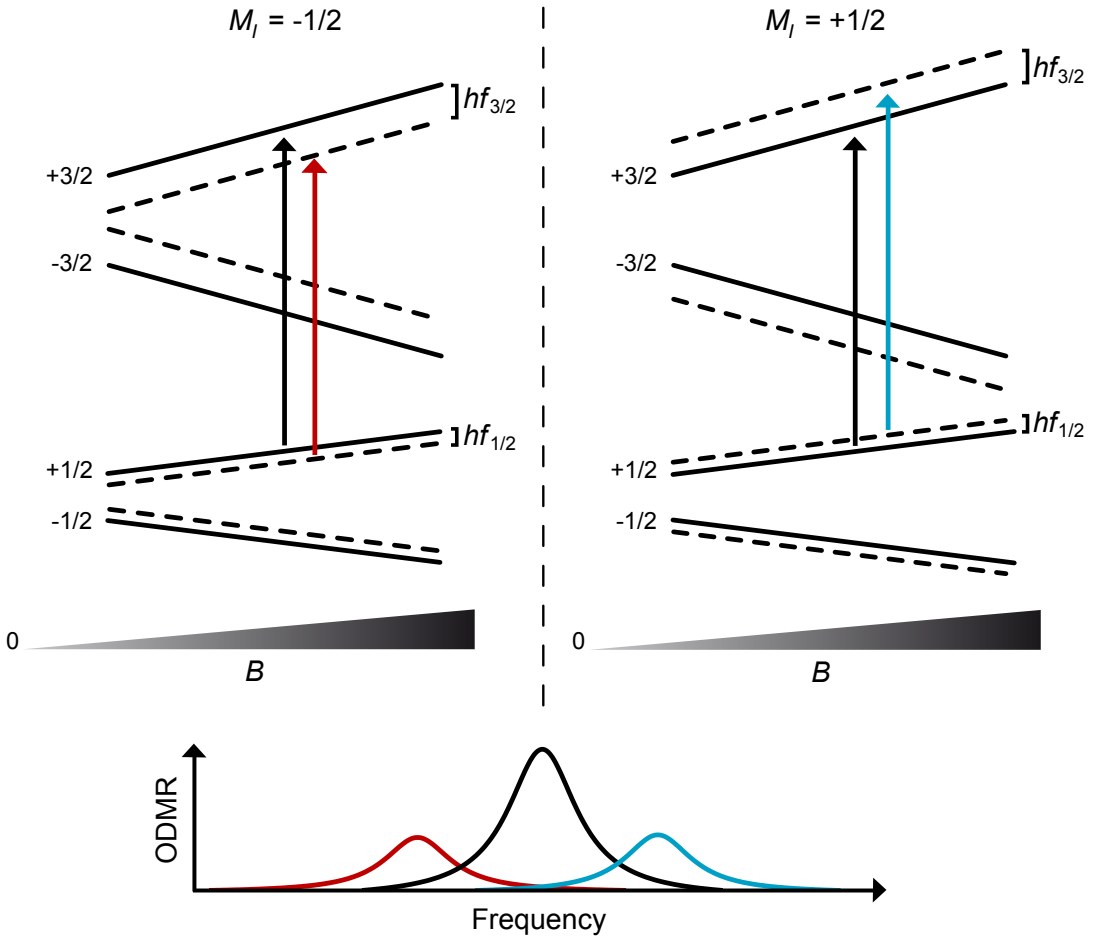

Figure 3.4.: Due to interaction between the electron spin and the nuclear spin of a neighboring ^{29}Si-isotope, the initial energy levels (solid lines) are shifted to higher or lower energies (dashed lines) depending on the relative alignment of the nuclear spin. Therefore, also the resonance frequency is shifted by $f_{3/2} - f_{1/2}$ (blue) and $-f_{3/2} + f_{1/2}$ (red) relative to the case of no spin carrying isotopes (black). The corresponding signal amplitudes can be calculated from the probability of a ^{29}Si isotope being among the nearest Si-atoms to the vacancy.

After clarifying the signal composition, the shape of the main line is analyzed. As elaborated in great detail by [64] the full width at half maximum (FWHM) $\Delta\nu$ of the signal can be derived as follows:

$$\Delta\nu \propto \sqrt{\frac{P_{RF} \cdot 1/T_2}{cP_L + 1/T_1}}, \tag{3.6}$$

with P_{RF} being the power of the radio waves, P_L the laser power, c the velocity of light and T_1, T_2 the spin-lattice and spin-spin relaxation times, respectively. Hence, the shape of the main peak is dependent on measurement properties like laser intensity and radio wave power, which define the pumping and transition rates, respectively.

Furthermore, the intrinsic coherence times T_1, T_2 of the electronic spins in $V_{Si}(h)$ are crucial for the linewidth.
For the actual measurement of these intrinsic properties, whose identification is one of the main tasks of this thesis, linewidth analysis alone is not sufficient due to several error sources from the dependence on setup properties like homogeneity of the radio waves over the defect distribution inside the sample or the laser power fluctuations. Therefore, a pulsed version of the ODMR technique is used, which will be introduced in the following.

3.4. Pulsed ODMR

Pulsed ODMR (pODMR) is a technique, which basic principles originate from the well established nuclear magnetic resonance (NMR), where pulse sequences are used to rotate the nuclear spin by a desired angle and monitor its temporal evolution [68]. In pulsed ODMR, this is realized by radio wave pulses of a certain length and power. Whereas in primary established constant-wave ODMR (cwODMR) the radio frequency is swept, while monitoring the change in photoluminescence, in pODMR the frequency is fixed to the resonance condition, while the temporal evolution of the photoluminescence is recorded. The basic functionality will be in the following explained on a simple example, depicted in Figure 3.5, where one laser pulse and one RF-pulse are applied simultaneously.
As the laser is turned on, the pumping process starts and a certain value of photoluminescence is established. When also the resonant radio waves are applied, the electron is excited from the pumped $M_S = \pm 1/2$ into the $M_S = \pm 3/2$ GS state and the photoluminescence increases.
With high temporal resolution, one can detect the spin flip process from the oscillations in the RF induced signal, the so-called Rabi oscillations [69]. The maxima of these oscillations imply a spin up position (spin in the $M_S = \pm 3/2$ state -> higher intensity) and the minima the spin down (spin in the $M_S = \pm 1/2$ state -> lower intensity) case. Due to inhomogeneities in the RF-field and spin-spin decoherence, these oscillations are damped, ultimately reaching the equal population of both states for long RF influence. Exactly this final value is measured by cwODMR as the change in photoluminescence. When the RF-pulse is off again, the photoluminescence decays due to ongoing laser excitation and spin-lattice relaxation back to the initial level.
Adjusting laser and RF-pulses with distinct durations into a sequence, the coherence properties of the defect can be studied. For a clear arrangement, these pulse sequences will be introduced in Chapter 5.

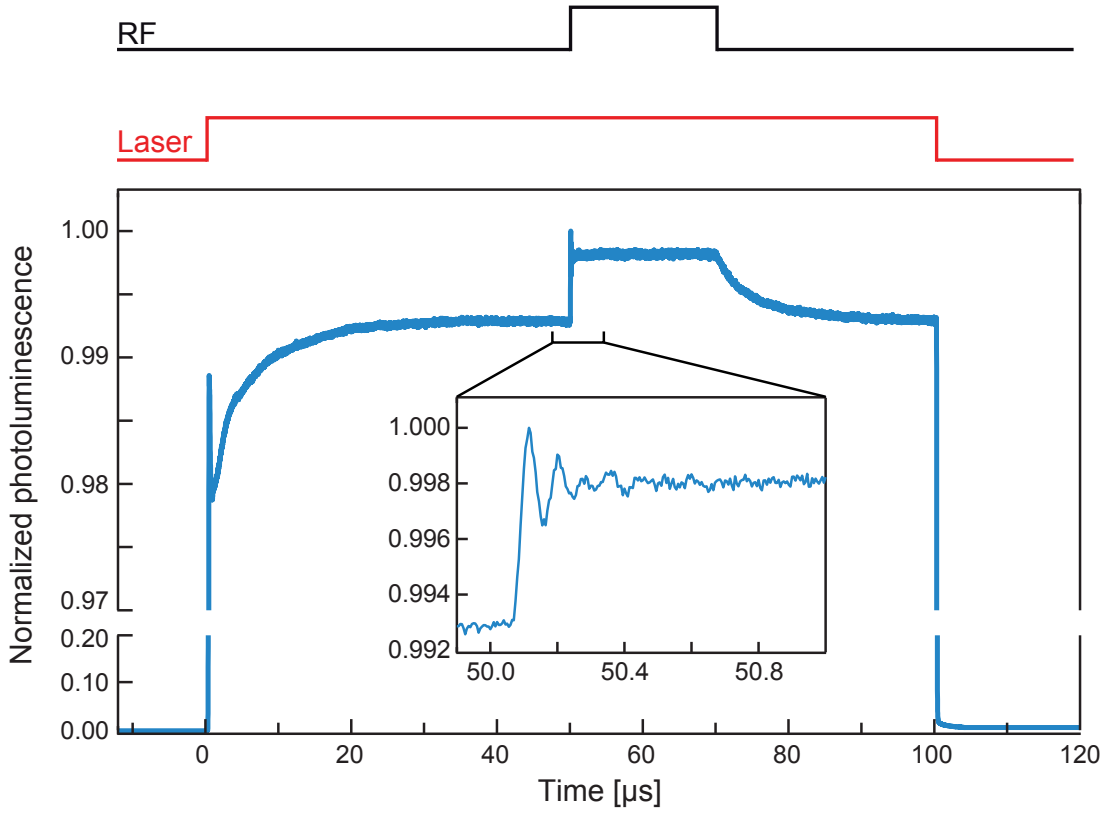

Figure 3.5.: Example of pulsed ODMR with one laser pulse and one radio wave pulse. One can directly observe the temporal change in photoluminescence when the RFs are switched on. Also, the spin transitions can be seen directly in the oscillations of the RF induced signal (inset).

By modifying the power and the length of the radio wave pulses, the spin state can be driven continuously between $M_S = \pm 3/2$ (spin up) and $M_S = \pm 1/2$ (spin down) until the decoherence prevails. By monitoring the temporal evolution of the photoluminescence, this so-called coherent control is achieved.

To sum up, all the measurements presented in this thesis are conducted using two different versions of ODMR: continuous-wave and pulsed ODMR. The first one, as described in Chapter 3.2, implies a continuous impact of both laser irradiation and radio waves on the defects and is used to realize sensing applications, which will be introduced in Chapter 4. In pODMR, both laser and radio waves are shaped into pulses with a distinct length and distance in order to derive intrinsic coherence times of the defect, as will be elaborated in Chapter 5.

3.5. Experimental Scheme

In order to carry out the described measurements, several hardware components are needed.
The heart of the setup is the custom assembled optical tower depicted in Figure 3.6, which is the link between the incoming laser, outgoing photoluminescence and sample illumination. These signals are transmitted via optical fibers.
The path of the laser light to the tower and subsequent path of the PL to the detector is as follows: First, the free space laser beam is coupled by several mirrors into a 50 µm optical fiber, which transfers the light to the optical tower. Here, the divergent beam is made parallel, to be focused by the 10× optical objective *Olympus LMPLN10XIR* on the 4H-SiC sample. The implemented cw laser *LD785-SE400* from *Thorlabs*, with a maximum power of 400 mW, has a wavelength of 785 nm, which coincides with the maximum of the absorption band of the defect [70] and hence is efficient in optical pumping. The objective (N.A. = 0.3) is focusing the laser onto the sample, resulting in an illuminated volume of roughly 300 μm^3. The induced photoluminescence from this volume is collected by the same objective, filtered from reflected laser light by 850 nm and 875 nm long pass filters and finally coupled into an optical fiber to be passed further to the avalanche photodiode *APD120A* from *Thorlabs*. With properly selected hot mirrors inside the tower, the camera on top provides a picture of the sample illuminated by a LED together with the laser spot. By using optical fibers with different cross-sections in front of the detector, the setup can also be used as a confocal microscope, since the fiber entrance acts like a pinhole. The main advantage of this construction is its modularity: by ensuring all beams to be parallel inside the tower, almost every component (fibers, mirrors, filters, objectives) can be exchanged or added without the need to recalibrate the whole scheme.
For cwODMR, the signal from the detector is processed by the lock-in amplifier *Signal Recovery DSP 7230*, while for pODMR it is fed in an oscilloscope card from *GaGe Compuscope* inside the laboratory PC. For both methods, custom-made data processing software is implemented.
In order to apply radio waves, the sample is placed on a 0.5mm copper stripline, to which the radio waves from the frequency generator *Stanford Research Systems SG384* are guided, additionally being amplified by the *Vectawave VBA1000-18* amplifier up to 18 W. This circuit is terminated by a 50 Ω resistor.

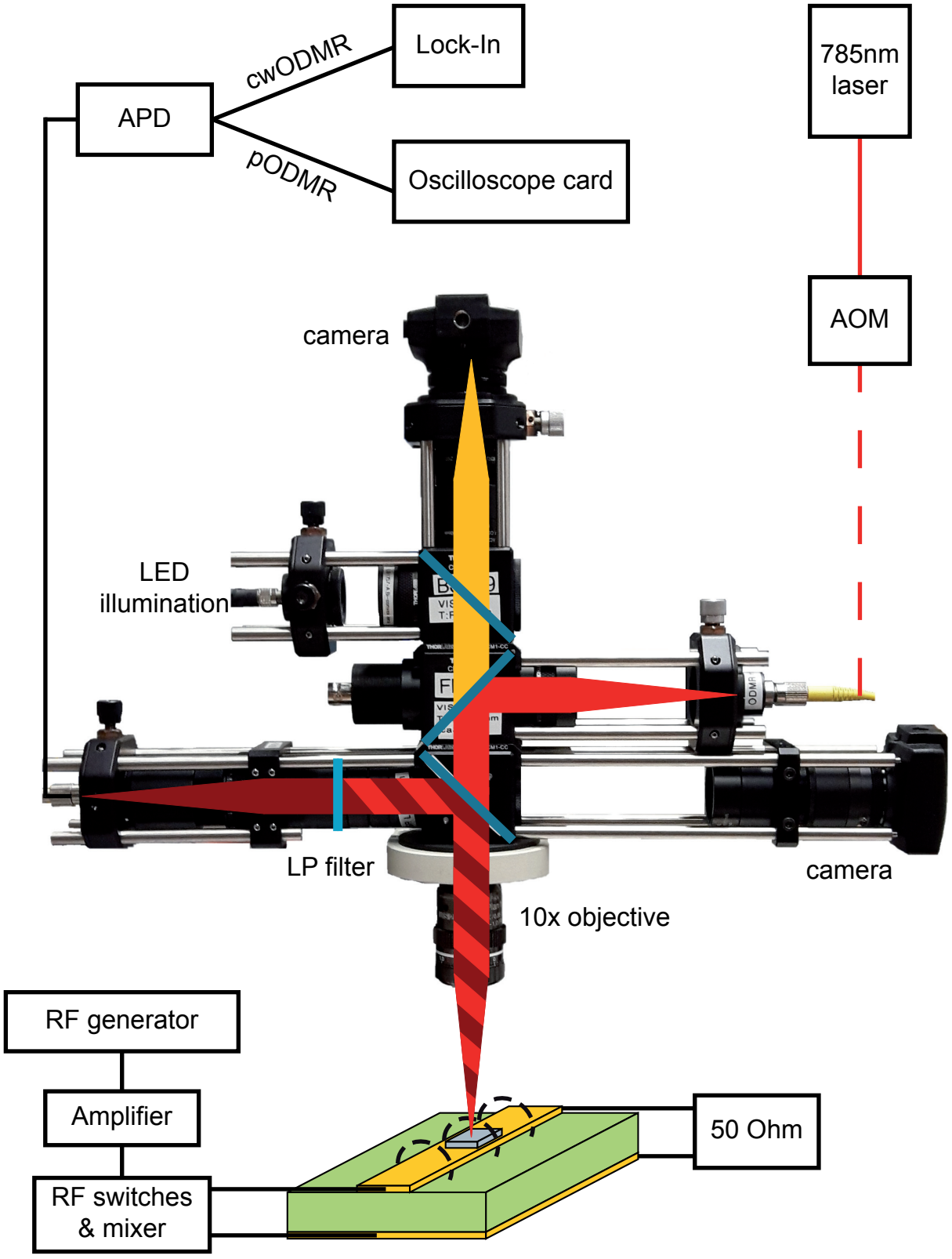

Figure 3.6.: A schematic of the general measurement setup with a focus on the custom designed optical tower. The path of the laser beam (bright red), photoluminescence (dark red) and imaging (yellow) inside the tower are denoted.

In order to conduct pulsed ODMR measurements, two modifications have to be further added to the setup: to create laser pulses, the acousto-optical modulator *A&A Opto-Electronic MT250-A02-800* is placed in the free space path of the laser beam. Furthermore, RF-switches *Mini-Circuits ZASWA-2-50DR+* and combiner *Mini-Circuits ZFSC-2-4-S+*, are used to shape the radio wave pulses. The pulse durations are defined by the TTL pulse generator card *PulseBlasterESR-PRO 500MHz* from *Spin-Core* inside the lab PC, which controls the mentioned components by sending differently shaped TTL pulses. This card can be programmed with an arbitrary pulse sequence by a self-made *LabView* software.

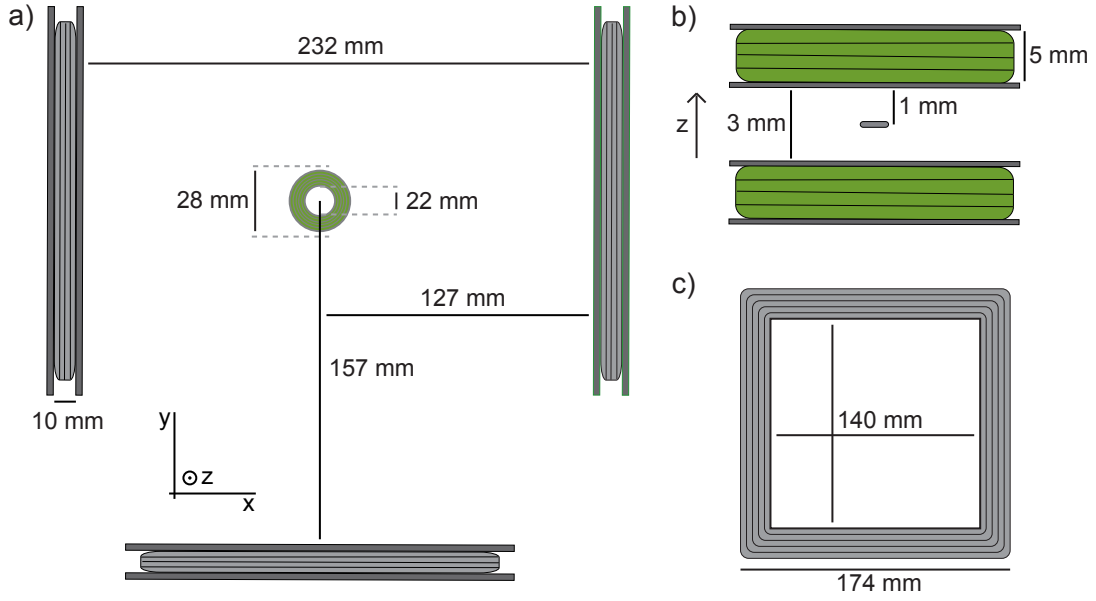

Figure 3.7.: a) Relative positions and dimensions of the custom-made coil arrangement, with a detailed scheme of the z-coils (b) and x,y-coils (c).

A major part of this thesis analyzes the behavior of the V_{Si} defects in an external magnetic field. The latter is established by a custom-made coil arrangement, depicted in Figure 3.7. Each coil (-pair) is driven by a separate voltage source, thus allowing for precise sweep of both the magnetic field strength as well as of the direction. The created field is calibrated by the 3D Hall-sensor *Honeywell HMC5883L*, with an angle sensitivity of 1° and magnetic field strength sensitivity of 0.5 µT [71].
Additionally, for magnetic field measurements up to 31 mT along the c-axis, a permanent NdFeB magnet of grade N42 is placed at a certain distance underneath the stripline.
Last but not least, in order to conduct temperature dependent measurements, the sample, as well as the stripline are placed into the cold finger helium cryostat *Oxford Instruments Microstat He*. The temperature is monitored by the resistive temperature sensor *Lakeshore DT-670B-SD*, placed next to the sample on the stripline.

4. Quantum Sensing

The discovery of the Hall effect by Edwin Herbert Hall in 1879, is the starting point for the triumphal procession of the Hall sensor technology [72]. As opposed to its predecessors, which relied on optical/mechanical detection methods, the Hall sensor is working electrically, by detecting a voltage proportional to the external magnetic field strength [73]. Nowadays, these sensors are by far dominating the market, being implemented in a variety of fields, from cell phones to spacecrafts [74]. Despite their popularity, Hall sensors are not impeccable, being susceptible to fluctuations in temperature, mechanical pressure or imprecision during manufacturing process [75].
Also, Hall sensors are so far quite limited in their sensitivity and spatial resolution, as seen in Figure 4.1.

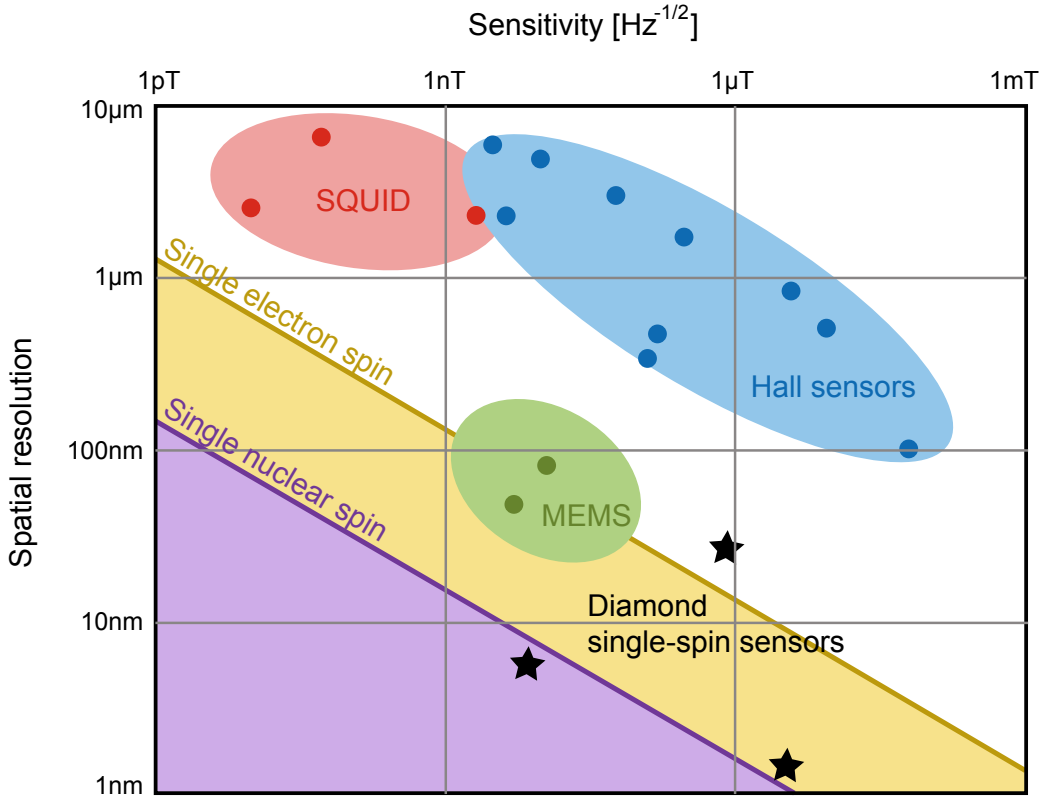

Figure 4.1.: Comparison of different magnetic field sensing methods in regard to their sensitivity and spatial resolution. The single electron/nuclear spin solid lines denote the limit in order to detect such a single spin (adapted from [76], diamond values from [43]).

For more accurate measurements, there are several complementary methods: Sensitivity on the order of femtotesla can be achieved with superconducting quantum interference devices (SQUIDS) [74], by using superconductivity effects. However, this requires extensive cooling down to a few Kelvin [77].
If the spatial resolution is the major aspect of interest, microelectromechanical (MEMS) magnetic field sensors are utilized, which detect the Lorentz force on a conducting cantilever, induced by a magnetic field [78].
To find a system with both outstanding spatial resolution and sensitivity is the major ongoing challenge in the field of magnetometry.
A relatively new method is magnetometry using optically addressable atomic-scale spin centers [7, 79]. Here, the magnetic field sensitive area can be as small as one atom, providing great spatial resolution. The most prominent example of successful implementation is the aforementioned NV-center in diamond. By using the ODMR technique, a sub-μT sensitivity and a spatial resolution on the nanometer scale can be achieved [8, 80].
Keeping in mind the advantages of silicon carbide elaborated in Chapter 2, the implementation of such an atomic-scale magnetometry based on spin centers in SiC is a warranted goal worth pursuing. The following chapters are dedicated to this task.
First, a vector magnetometry implementation is proposed and compared to the NV-center based ones, assuming the uniaxial model of the defect (Chapter 4.1). In Chapter 4.2, the fine structure is revealed and a magnetometry method for magnitudes in sub-100 nT range is introduced in Chapter 4.3. Finally, an application for simultaneous thermometry is demonstrated in Chapter 4.4.
Note that all the following proof-of-concept measurements were conducted on ensembles of defects, while the obtained results can be applied to single defects as well.

4.1. Vector Magnetometry

The evolution of the ODMR signal with the external magnetic field can be utilized in order to measure both the magnetic field strength, as well as its direction relative to the crystal axis, i.e. c-axis. As elaborated in Chapter 3.2 for the case of parallel alignment of the external magnetic field B and the c-axis, the magnetic field strength can be deduced solely from the spectral position and distance of the detected peaks. Here, a technique will be presented, with which the extraction of both the strength as well as the angle to the c-axis of an external magnetic field is possible from one single ODMR measurement. First, the theoretical principles will be established, with subsequent experimental verification and implementation as a vector magnetometer.

4.1.1. Theoretical Considerations

In this chapter the general case of an arbitrary direction of B with respect to the c-axis is analyzed. For this cause, the energetic structure of the defect will be described assuming an uniaxial model, which, as will be elaborated in the next Chapter 4.2, does not reflect the full complexity of the C_{3v} symmetry, but explains sufficiently the experimental results in order to understand the general concept.

In this model, the Spin-Hamiltonian of a spin 3/2 system in an external magnetic field B has the form [81]:

$$\mathscr{H} = g_e \mu_B \mathbf{BS} + D\left(S_z^2 - S(S+1)/3\right) + E(S_+^2 + S_-^2)/2. \tag{4.1}$$

Here, $\mathbf{S}$ is the spin operator, $g_e \approx 2.0$ is the electron g-factor, μ_B is the Bohr magneton, S_z is the projection of the total spin on the c-axis, $S_\pm = S_x \pm iS_y$ and D and E the longitudinal and transverse crystal field parameters, respectively. In the uniaxial model, only the longitudinal splitting parameter D is considered, while the transverse parameter $E << D$ is neglected. In accordance with the Kramers theorem, the $M_S = \pm 3/2$ and $M_S = \pm 1/2$ states remain doubly degenerated even in the presence of electric and strain fields, making $E = 0$ a good approximation.

The spin tensor $\mathbf{S}$ consists of one spin matrix for each of the three spacial coordinates:

$$S_x = \begin{vmatrix} 0 & \frac{\sqrt{3}}{2} & 0 & 0 \\ \frac{\sqrt{3}}{2} & 0 & 1 & 0 \\ 0 & 1 & 0 & \frac{\sqrt{3}}{2} \\ 0 & 0 & \frac{\sqrt{3}}{2} & 0 \end{vmatrix}, \; S_y = \begin{vmatrix} 0 & -\frac{\sqrt{3}}{2}i & 0 & 0 \\ \frac{\sqrt{3}}{2}i & 0 & -i & 0 \\ 0 & i & 0 & -\frac{\sqrt{3}}{2}i \\ 0 & 0 & \frac{\sqrt{3}}{2}i & 0 \end{vmatrix}, \; S_z = \begin{vmatrix} \frac{3}{2} & 0 & 0 & 0 \\ 0 & \frac{1}{2} & 0 & 0 \\ 0 & 0 & -\frac{1}{2} & 0 \\ 0 & 0 & 0 & -\frac{3}{2} \end{vmatrix}. \tag{4.2}$$

With the approximation $E = 0$, the eigenvalues λ can be deduced from the Hamiltonian 4.1 in polar coordinates as follows [81]:

$$\lambda^4 - (2D^2 + \frac{5}{2}\beta^2) \cdot \lambda^2 - 2\beta^2 \cdot D(3\cos^2(\theta) - 1) + \frac{9}{16}\beta^4 + D^4 - \frac{1}{2}D^2\beta^2 - D^2\beta^2(3\cos^2(\theta) - 1) = 0, \tag{4.3}$$

with $\beta = g_e \mu_B B$ and θ the polar angle of the B-field to the symmetry axis c of the crystal.

Thus, without an external magnetic field, the eigenvalues become $\lambda_{B=0} = \pm D$ and the zero field splitting between the energetic levels is equal to $2D$, with a distance $\pm D$ to the chosen energetic zero point.

For a magnetic field along the c-axis, the eigenvalues become:

$$\lambda_{1/2} = -D \pm \frac{1}{2} g_e \mu_B B, \tag{4.4}$$

$$\lambda_{3/2} = -D \pm \frac{3}{2} g_e \mu_B B. \tag{4.5}$$

From Equations 4.1 and 4.3, the eigenvalues λ are numerically deduced and the level splitting at different angles θ between B and the c-axis simulated. This is depicted exemplary for four different angles in Figure 4.2. It is evident that for $\theta \neq 0°$, the energy levels do not cross anymore, resulting in a so-called level anticrossing. The levels are denoted with $j = 1,2,3,4$, since the assignment of the spin states to each level is not explicit anymore due to state mixing, induced by the transverse component of the magnetic field.

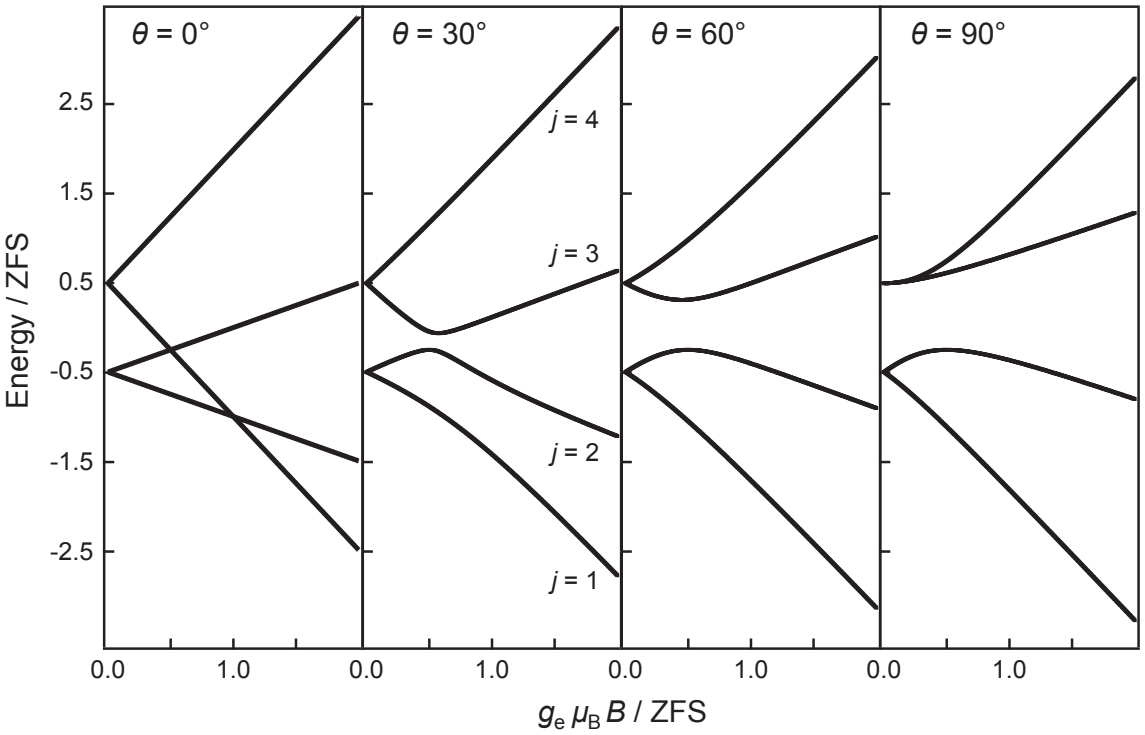

Figure 4.2.: Numerically calculated evolution of the eigenvalues from Equation 4.3 with the magnetic field, for an inclination from the c-axis of 0°, 30°, 60° and 90° (from left to right).

By applying resonant radio frequencies B_1, spin flipping is induced, with a probability $W_{j,k}$ for the $|j\rangle \rightarrow |k\rangle$ transition, which defines the intensity of the respective ODMR line [82]:

$$W_{j,k} \propto \left|\langle \Psi_j | \mathbf{B_1 S} | \Psi_k \rangle\right|^2. \tag{4.6}$$

The maximal intensity is therefore achieved for $B_1 \perp c$.
With the probability $W_{\pm 1/2,\pm 3/2}$ and the eigenvalues from Equation 4.3, both the position, as well as the relative intensity of the ODMR signal in dependence on the magnetic field strength and polar angle θ can be reconstructed. This is depicted in Figure 4.3b for $\theta = 0°$ ($B \| c$) and $\theta = 20°$, with the line thickness denoting the probability of the corresponding transition.

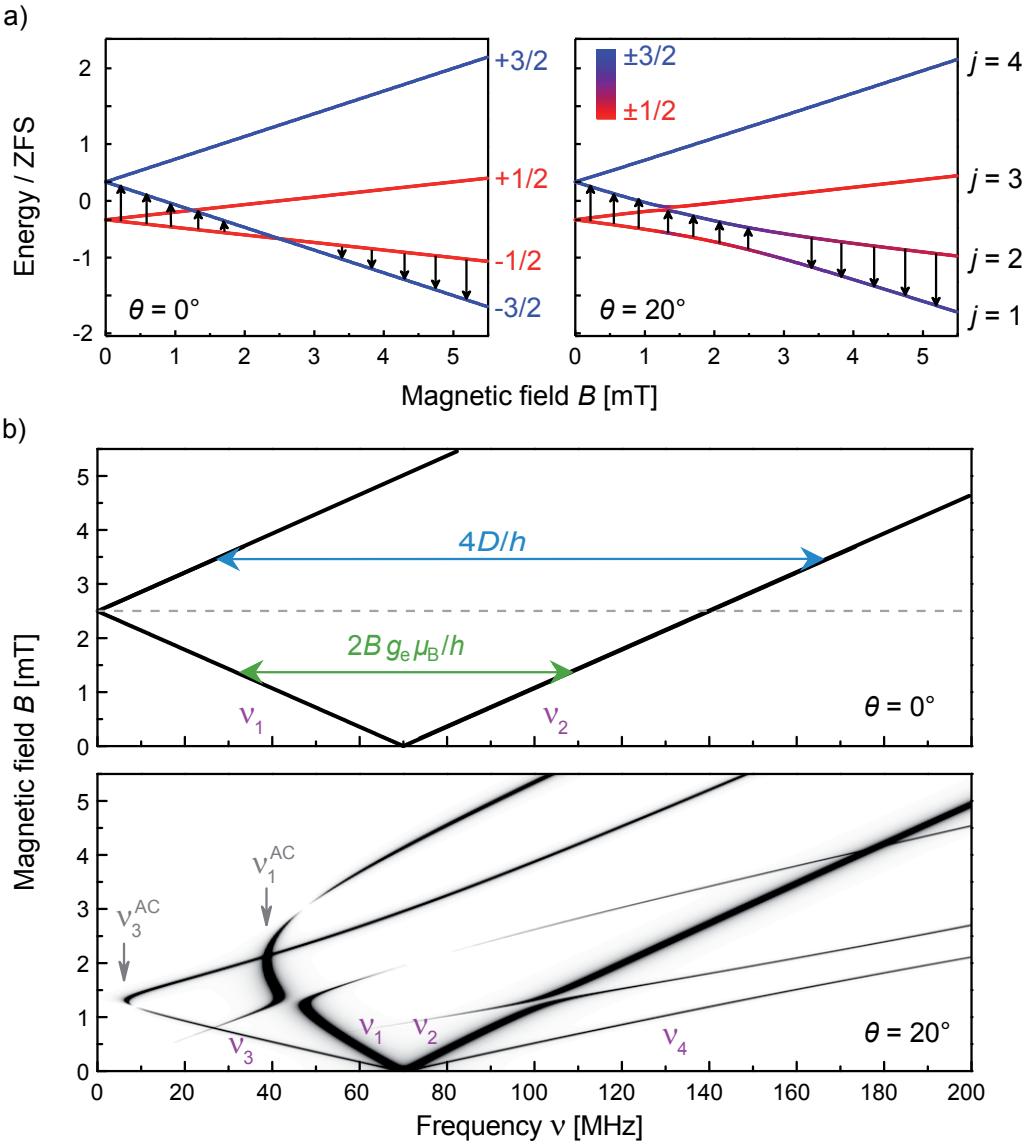

Figure 4.3.: a) Evolution of spin sub-levels in the ground state with magnetic field parallel (left) and at an angle of $\theta = 20°$ (right) to the c-axis, calculated with the Hamiltonian in Equation 4.1. While for parallel alignment the degeneracy is completely lifted, for $\theta = 20°$ a state mixing occurs. The arrows denote the transition associated with the ν_1 line. b) Simulated evolution of the ODMR signals for $\theta = 0°$ (top) and $\theta = 20°$ (bottom), with the line thickness denoting the ODMR contrast.

Hence, for $B \| c$, two ODMR lines are expected, originating from the $|-1/2\rangle \rightarrow |-3/2\rangle$ (ν_1 line in Figure 4.3b) and the $|+1/2\rangle \rightarrow |+3/2\rangle$ (ν_2 line) transitions.

It is evident that by presence of a transverse magnetic field component $B\sin(\theta)$ the evolution of the ODMR peaks cannot be explained in the same way as in the $B \| c$ case. On the one hand, the mixing of the $M_S = \pm 1/2$ states in the transverse component of the magnetic field $B\sin(\theta)$ (Figure 4.3a) results in the appearance of two additional ODMR lines ν_3, ν_4. On the other hand, the already mentioned anticrossings occur at 1.3 mT between the states j = 2 and j = 3, as well as at around 2.5 mT between j = 1 and j = 2. This manifests itself as "turning points" of the line evolutions at frequencies $\nu_3^{AC} = 6\,\text{MHz}$ and $\nu_1^{AC} = 39\,\text{MHz}$.

This energetic spin state mixing will be elaborated by analyzing the eigenfunctions $\Psi(\theta)$ for the low field approximation $g_e\mu_B B << \text{ZFS}$, hence for dominating crystal field.

Without loss of generality, it will be assumed that B is lying in the x-z plane, tilted by an angle θ in regard to the z-axis, which coincides with the c-axis of the defect. The Hamilton operator from Equation 4.1, can thus be written as:

$$\mathscr{H} = g_e\mu_B B \cdot (S_z \cos(\theta) + S_x \sin(\theta)) + D \cdot \left(S_z^2 - \frac{5}{4}\mathfrak{I}\right), \tag{4.7}$$

with S_x and S_z being the spin matrices from Equation 4.2 and $\mathfrak{I}$ the identity matrix. The resulting eigenfunctions Ψ are written in the basis of the spin number M_S as:

$$\Psi_a = \begin{pmatrix} a_{3/2} \\ a_{1/2} \\ a_{-1/2} \\ a_{-3/2} \end{pmatrix}. \tag{4.8}$$

For the case $g_e\mu_B B << \text{ZFS}$, the $M_S = \pm 3/2$ and $M_S = \pm 1/2$ levels can be considered as energetically independent.

For the $\pm 3/2$ states, the spin matrices are:

$$S_x^{\pm 3/2} = \begin{vmatrix} 0 & 0 \\ 0 & 0 \end{vmatrix}, \; S_z^{\pm 3/2} = \frac{3}{2} \cdot \begin{vmatrix} 1 & 0 \\ 0 & -1 \end{vmatrix}. \tag{4.9}$$

Modifying the Hamiltonian to:

$$\mathscr{H} = D + g_e\mu_B B \cdot \frac{3}{2}\cos(\theta) \cdot \begin{vmatrix} 1 & 0 \\ 0 & -1 \end{vmatrix}. \tag{4.10}$$

The resulting eigenfunctions are:

$$\Psi_1 = \begin{pmatrix} 1 \\ 0 \\ 0 \\ 0 \end{pmatrix}, \ \Psi_4 = \begin{pmatrix} 0 \\ 0 \\ 0 \\ 1 \end{pmatrix}. \tag{4.11}$$

Similarly for the $M_S = \pm 1/2$ states:

$$S_x^{\pm 1/2} = \begin{vmatrix} 0 & 1 \\ 1 & 0 \end{vmatrix}, \ S_z^{\pm 1/2} = \frac{1}{2} \cdot \begin{vmatrix} 1 & 0 \\ 0 & -1 \end{vmatrix}, \tag{4.12}$$

$$\mathscr{H} = -D + g_e \mu_B B \cdot \frac{1}{2} \cdot \begin{vmatrix} \cos(\theta) & 2\sin(\theta) \\ 2\sin(\theta) & -\cos(\theta) \end{vmatrix}, \tag{4.13}$$

$$\Psi_2 = \begin{pmatrix} 0 \\ \sqrt{\frac{1}{2} + \frac{\cos(\theta)}{2\sqrt{1+3\sin^2(\theta)}}} \\ \sqrt{\frac{1}{2} - \frac{\cos(\theta)}{2\sqrt{1+3\sin^2(\theta)}}} \\ 0 \end{pmatrix}, \ \Psi_3 = \begin{pmatrix} 0 \\ \sqrt{\frac{1}{2} - \frac{\cos(\theta)}{2\sqrt{1+3\sin^2(\theta)}}} \\ \sqrt{\frac{1}{2} + \frac{\cos(\theta)}{2\sqrt{1+3\sin^2(\theta)}}} \\ 0 \end{pmatrix}. \tag{4.14}$$

It is evident that while for the $M_S = \pm 3/2$ states the degeneracy is lifted by the magnetic field (Ψ_1 and Ψ_4 orthogonal), the $M_S = \pm 1/2$ states in general stay mixed also after level splitting. This leads to appearance of four possible induced transitions with $\Delta M_S = \pm 1$ for $\theta \neq 0°$, with their probabilities described by Equation 4.6 for $B_1 \perp$ c. In Figure 4.4a the dependence of the energetic states on the polar angle θ at a fixed magnetic field $B = 100\,\mu\text{T}$ is depicted, as numerically calculated from Equation 4.3.

The four allowed transitions result in four ODMR peaks at following frequencies:

$$\nu_{1,2} \cdot h = h\nu_0 \mp g_e \mu_B B \cdot f_{in}(\theta) + \zeta(\theta) B^2, \tag{4.15}$$

$$\nu_{3,4} \cdot h = h\nu_0 \mp g_e \mu_B B \cdot f_{out}(\theta) + \zeta(\theta) B^2, \tag{4.16}$$

with $h\nu_0 = 2D$, $f_{in,out}$ being linearly independent trigonometric functions:

$$f_{in,out}(\theta) = \frac{\left| 3\cos(\theta) \mp \sqrt{1 + 3\sin^2(\theta)} \right|}{2}, \tag{4.17}$$

and quadratic constant $\zeta(\theta)$, calculated in [8] and [83]:

$$\zeta(\theta) = \frac{3g_e^2\mu_B^2\sin^2(\theta)}{2h\nu_0}. \tag{4.18}$$

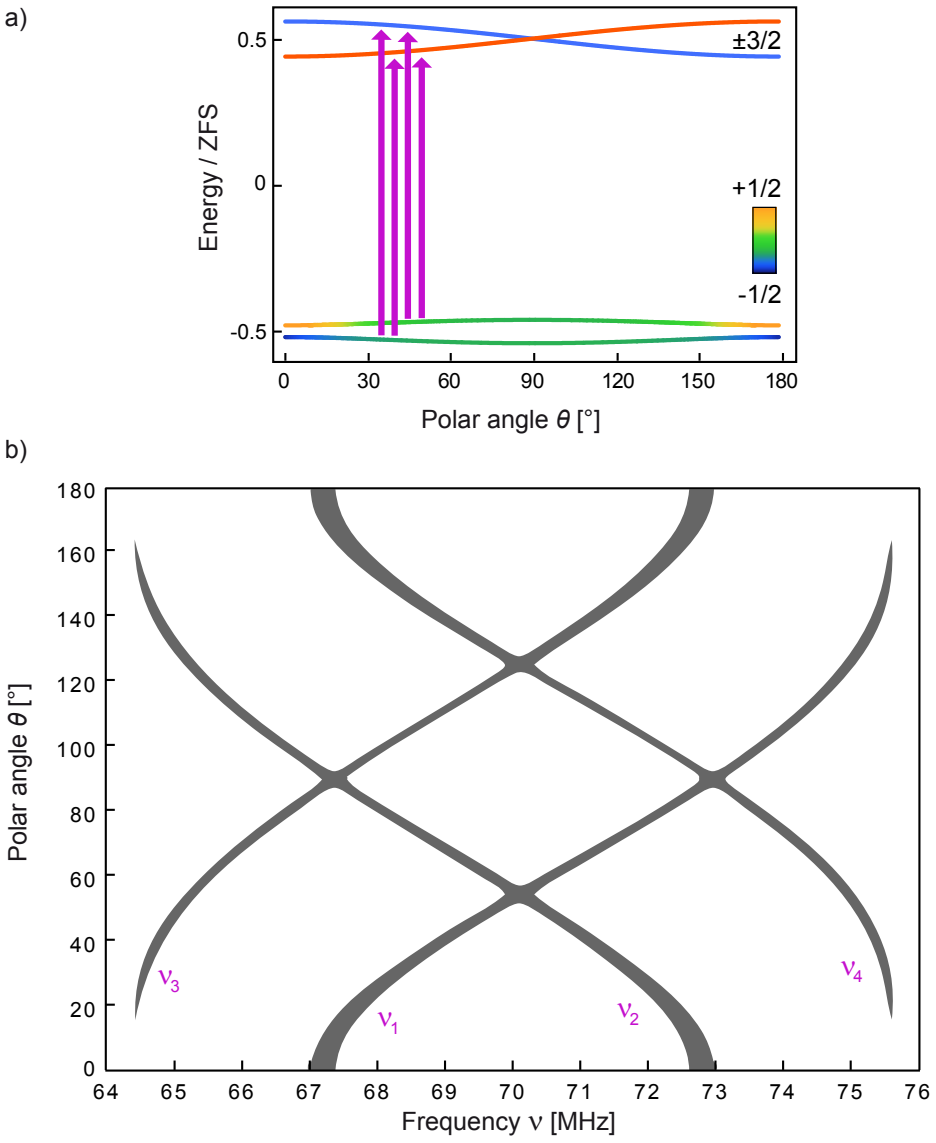

Figure 4.4.: a)Level splitting of the ground states for $B = 100\,\mu\text{T}$ in dependence on the polar angle θ. For $\theta \neq 0°$ the mixing of $\pm 1/2$ states occurs, leading to four allowed transitions. At $\theta = 0°$ and $\theta = 180°$ the eigenfunctions are orthogonal in the uniaxial model, expecting two allowed transitions with $\Delta M_S = \pm 1$. b) The resulting evolution of the ODMR peaks with θ. The line thickness denotes the expected ODMR contrast.

From these equations it is evident, that the polar angle θ can be deduced from the relative splittings of the inner and outer resonances:

$$\frac{\nu_2 - \nu_1}{\nu_4 - \nu_3} = \frac{f_{in}(\theta)}{f_{out}(\theta)} = \kappa(\theta). \tag{4.19}$$

As seen in Equation 4.17, the angle determination is done without the need to consider the magnetic field strength and subsequently the quadratic shift $\zeta(\theta)B^2$. The two functions $f_{in,out}(\theta)$ are plotted in accordance with Equation 4.17 in Figure 4.5a. The line thickness denotes the calculated probability of the respective transitions using Equation 4.6.

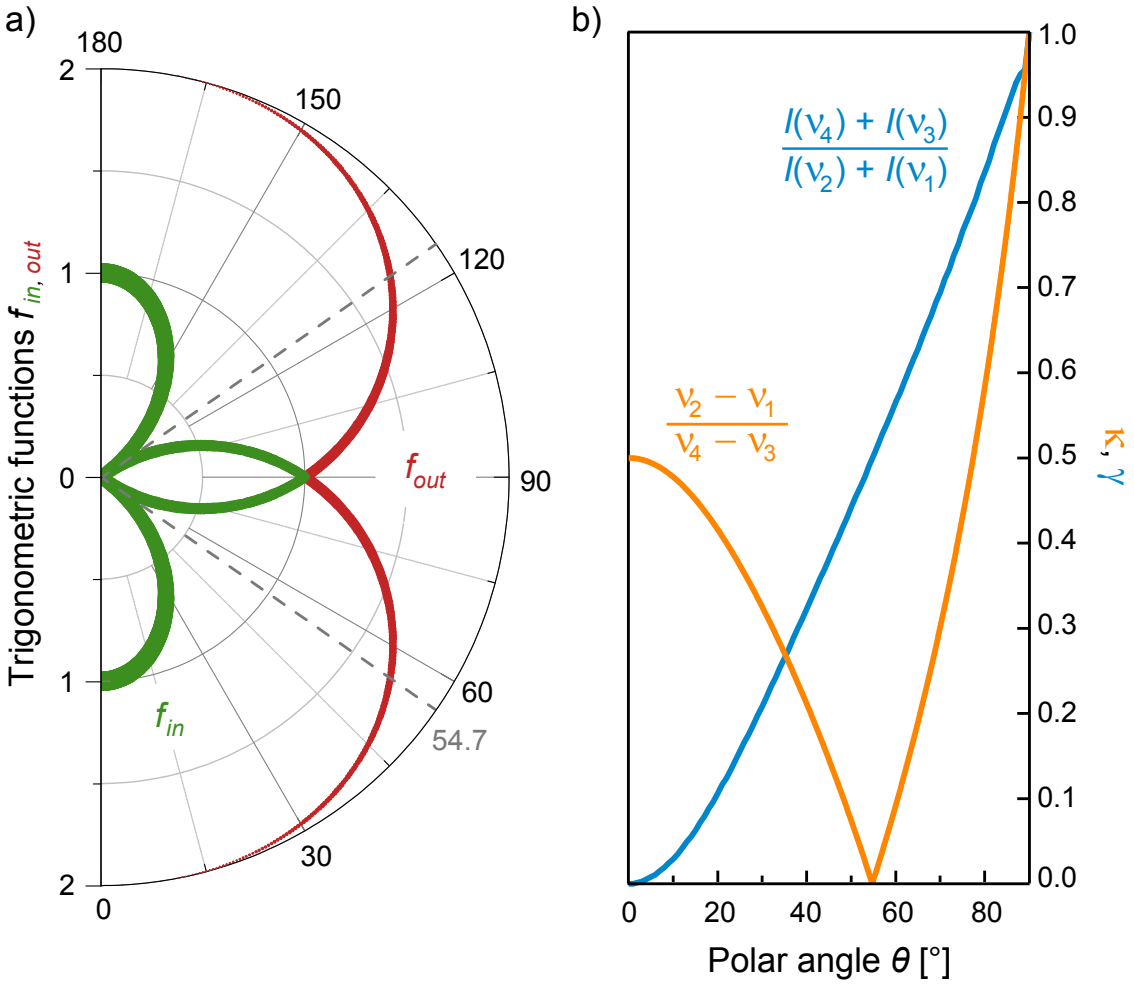

Figure 4.5.: a) Linearly independent trigonometric functions $f_{in,out}(\theta) = \left|3\cos(\theta) \mp \sqrt{1+3\sin^2(\theta)}\right|/2$. The line thicknesses of f_{in} (green) and f_{out} (red) reflect the ODMR contrast of the $\nu_{1,2}$ and the $\nu_{3,4}$ transitions, respectively. b) Relative spectral position $\kappa(\theta)$ (orange) and relative intensity $\gamma(\theta)$ (blue) in dependence on the polar angle.

In Figure 4.5b, the splitting ratio $\kappa(\theta)$ for angle determination is depicted. Here it is evident that for the most angles, two values of κ come into question. In order to assign a certain κ value to a measurement, also the relative intensity $\gamma(\theta)$ has to be considered. The latter is calculated with Equation 4.6 as the ratio of the overall intensity of inner and outer peaks:

$$\gamma(\theta) = \frac{I(\nu_3) + I(\nu_4)}{I(\nu_1) + I(\nu_2)}, \tag{4.20}$$

and is also plotted in Figure 4.5b.
A special case is predicted for three angles, as can be seen in Figure 4.4a: at 0° and 90° one expects only two peaks, due to complete lifting of the spin degeneracy in the first case and energetic crossing of the $M_S = \pm 3/2$ states in the latter. For the angle $\theta = \arccos(1/\sqrt{3}) \approx 54.7°$, which is known as the "magic angle" from the Magnetic Resonance Imaging (MRI) field [84], three peaks are expected. In this case, f_{in} is zero and the inner peaks merge into one (see Equation 4.16).
All in all, for every angle θ, there is a unique pair of the relative spectral positions κ and relative intensities γ of detected peaks, which measurement allows unambiguous determination of the polar angle and subsequent extraction of the magnetic field strength.
At this point, a brief comparison to the magnetic field sensing using the NV-centers in diamond is instructive. A detailed elaboration of the properties of the NV-centers is out of scope of this work and can be found among others in [7] and [6]. Since these centers are $S = 1$ -systems, there are only two detectable transitions ($M_S = 1 \leftrightarrow M_S = 0$ and $M_S = -1 \leftrightarrow M_S = 0$) and hence only two ODMR lines for every polar angle appear. The two peaks are propagating with the magnetic field as:

$$\nu_{1,2}^{NV} \cdot h = h\nu_0 \mp g_e \mu_B B\cos(\theta) + \zeta(\theta) B^2. \tag{4.21}$$

Hence, from the splitting of these two peaks alone, only the projection $B\cos(\theta)$ on the c-axis can be deduced. The full reconstruction of the magnetic field strength requires ensemble measurements: The NV-defect in the diamond cubic lattice is oriented along one of four $\langle 111 \rangle$ crystallographic axes [85, 86], and by fabrication of defects with a preferential alignment, also the transverse field component can be reconstructed. These implementations however require high homogeneity of the NV-center distribution. As seen from Equation 4.21, the ODMR lines also exhibit a quadratic shift. With the coefficient $\zeta(\theta)$ from Equation 4.18 depending on the magnetic field orientation, the polar angle θ can be determined.

However, the angular sensitivity vanishes rapidly in the sub-millitesla range as $\delta\theta \propto \nu_0/B^2$, making the extraction of the polar angle difficult. The here proposed technique using V_{Si} centers in SiC does not rely on the quadratic shift and enables the extraction of the magnetic field strength and the polar angle from a single measurement on both ensembles as well as on single defects. A detailed comparison of achievable resolution between the NV-center and V_{Si} based techniques will be elaborated in Chapter 4.1.3. Now, after establishing the vector magnetometry technique with V_{Si} centers in SiC theoretically, its functionality will be verified on actual experiments.

4.1.2. Experimental Verification

All the measurements presented in the following were conducted on a 4H-SiC bulk crystal at room temperature. The crystal has been grown by the standard sublimation technique, such that the [0001] crystallographic direction (c-axis) is inclined at an angle of 7° to the surface normal, i.e. the z-axis of the laboratory coordinate system (Figure 4.6). For creation of V_{Si} defects, the crystal has been irradiated with neutrons of an energy 5 MeV with a fluence of $10^{16}\,\mathrm{cm}^{-2}$.

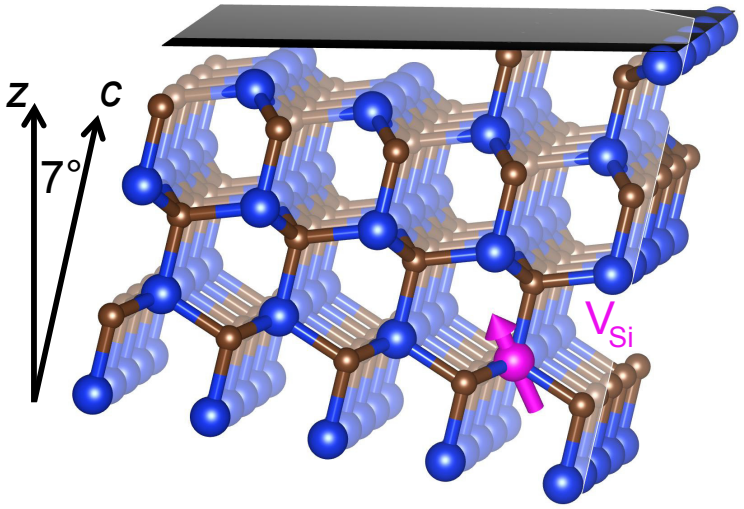

Figure 4.6.: Schematic of the used 4H-SiC bulk crystal, with the c-axis inclined by 7° from the surface normal.

To see how well the simulations describe the measurements, a case with $B \| z$, i.e. $\angle B, \mathrm{c} = 7° = \theta$ is considered first. To make the simulations more realistic, the Lorentzian line shape from Table 3.1, including the hyperfine interaction, is incorporated. The result is shown in Figure 4.7.

Due to relatively small deviation from the defect symmetry axis, the behavior is quite similar to the high-symmetry case $B \| c$ (Figure 4.3). Nevertheless, the manifestation of an anticrossing ($\nu_1^{AC} = 13\,\text{MHz}$) between the $M_S = \pm 3/2$-like and $M_S = \pm 1/2$-like states at 2.5 mT and the appearance of outer resonances ν_3 and ν_4, which evolve with twice the slope of the inner resonances, are distinct features of $\theta \neq 0°$. This behavior is closely reproduced by the simulation.
Therefore, once the angle θ is identified, the magnetic field can be unambiguously determined from the positions of the ODMR peaks.

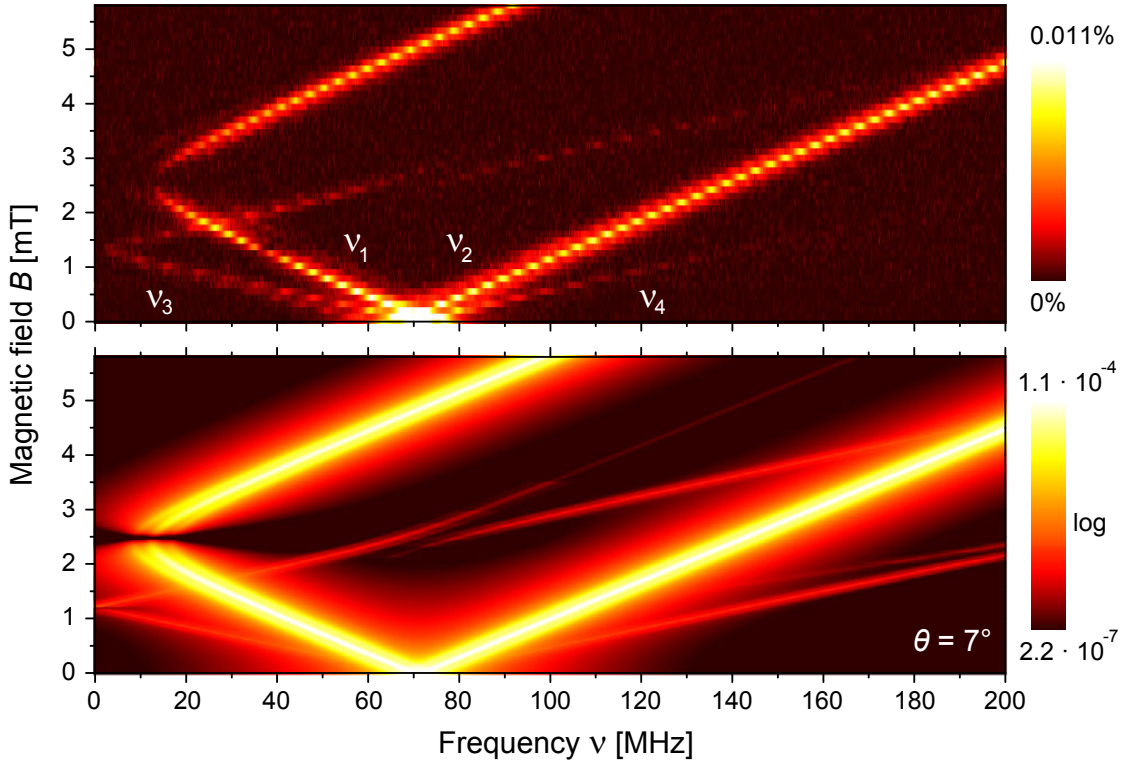

Figure 4.7.: Comparison of the ODMR measurement (top) and simulation (bottom) for magnetic fields applied at an angle $\theta = 7°$ with respect to the c-axis ($B \| z$). The ODMR contrast is color coded, while in the simulation, logarithmic scale is used to pronounce the outer resonances.

In order to illustrate the determination of the polar angle, the evolution of the ODMR spectra as a function of the magnetic field orientation at a fixed magnitude $B = 0.8\,\text{mT}$ is conducted. Therefore, the magnetic field vector is tilted from the z-axis ($\vartheta_B = 0°$) in $\Delta\vartheta_B = 5°$ steps until $\vartheta_B = 90°$. The result is shown in Figure 4.8a, along with the simulated evolution with the angle θ between B and c. Since the defect symmetry axis is not exactly parallel to the z-axis ($\vartheta_B \neq \theta$, Figure 4.6), there is a constant offset in the polar angle between the measurement and the calculated spectra.

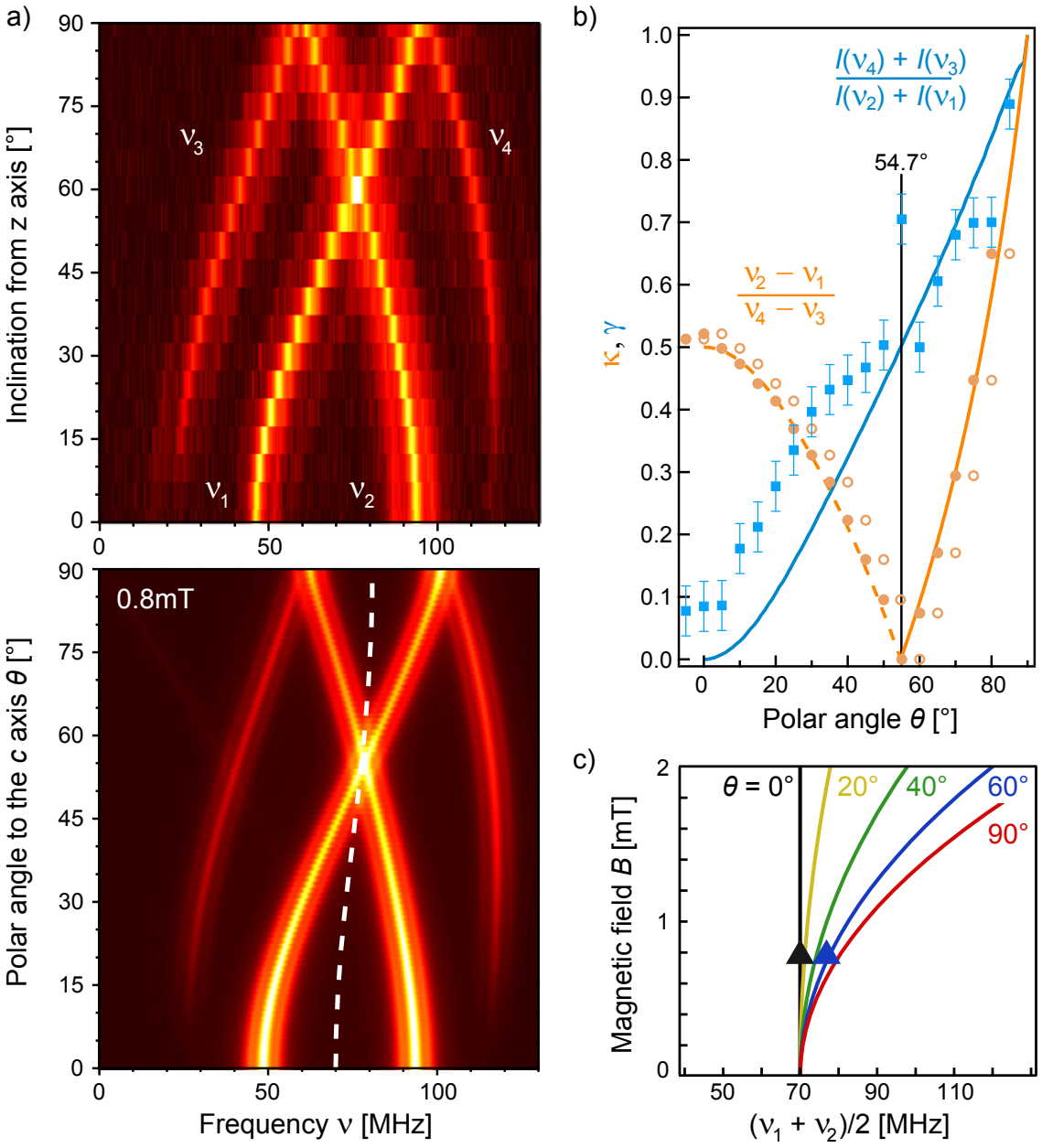

Figure 4.8.: a) Angular dependence of measured (top) and calculated (bottom) ODMR spectra at $B = 0.8\,\mathrm{mT}$. The color coding of the ODMR contrast is equal to Figure 4.7. The dashed line indicates the non linear shift $(\nu_1 + \nu_2)/2$, which is depicted in c) in dependence of the magnetic field for various polar angles, along with the measured values for 0° and 54.7°. b) Polar angle dependence on the relative splitting $\kappa(\theta) = (\nu_2 - \nu_1)/(\nu_4 - \nu_3)$ and relative amplitude $\gamma(\theta) = (I(\nu_3) + I(\nu_4))/(I(\nu_1) + I(\nu_2))$. The dashed line corresponds to angles when the outer ODMR lines are weak (see main text). Open circles are unaltered experimental $\kappa(\theta)$ values, while solid symbols are shifted by 7° to account for the inclination of the c-axis with respect to the z-axis.

Aside from that, the simulation resembles closely the experimental signal evolution. From this measurement it becomes evident that the spectral distance of the inner ($\nu_2 - \nu_1$) and the outer ($\nu_4 - \nu_3$) resonances changes distinctly with the orientation of the magnetic field.
Following Equation 4.19 and Figure 4.5, the polar angle can be deduced from the ratio of these two splittings $\kappa(\theta) = (\nu_2 - \nu_1)/(\nu_4 - \nu_3)$. This is shown in Figure 4.8b, where the evolution of the polar angle θ in regard to $\kappa(\theta)$ is depicted. The solid and dashed lines represent the theoretical calculations, while the circles are measured values. Open circles are the unaltered data obtained from the measurements.
There is a constant offset of the experimental data from the expectation. Shifting the values by 7°, one obtains an outstanding agreement between the measurement and the theory. Remarkably, this shifting angle coincides with the tilting angle of the c-axis with respect to the z-axis (Figure 4.6).
For unambiguous angle determination from a single measurement, also the relative intensities have to be considered. These are depicted in Figure 4.8b as squares, already shifted by 7°. One sees that while the general tendency is following the theory, there is a constant offset at small angles θ towards a higher ratio from expected values. This means that the outer peaks have a higher intensity than assumed by the uniaxial model. This is a strong indication that this model, as stated in the beginning of the chapter, cannot describe the full complexity of defect's energetic properties. While the true form of the fine structure will be uncovered in Chapter 4.2, the polar angle and magnetic field strength determination can nevertheless be conducted as intended, since it relies primarily on the relative spectral splitting $\kappa(\theta)$, which shows exceptional agreement between measurement and expectation.
Therefore, the algorithm to determine the orientation of the magnetic field can be established as follows. If $\theta > 54.7°$, the $M_S = \pm 1/2$ states are strongly mixed and the outer resonances are well resolved. In this case, the ratio of intensities is >50% and the measured relative distance between the ODMR lines κ is compared to the calibration curve denoted by the solid line in Figure 4.8b. In the opposite case $\theta < 54.7°$, the $M_S = \pm 1/2$ states are weakly mixed and the outer ODMR lines have a smaller magnitude, leading to an intensity ratio < 50%. The corresponding calibration curve to determine θ is shown by the dashed line.
Either way, the polar angle can be unambiguously derived from the relative positions of the ODMR lines, considering the differences in signal amplitudes.
If implementing vector magnetometry with $S = 1$ centers like NV-centers in diamond, the polar angle is deduced from the quadratic shift $\zeta(\theta)$ as composed in Equation 4.18.

According to Equation 4.15 this parameter can be experimentally determined from the mean value of the spectral positions of the inner peaks:

$$h \cdot \frac{\nu_1 + \nu_2}{2} = h\nu_0 + \zeta(\theta)B^2. \tag{4.22}$$

This is denoted by the white dotted line in Figure 4.8a. In Figure 4.8c, the calculated evolution of $\zeta(\theta)B^2$ with the magnetic field for several polar angles is depicted. Also, two exemplary measured values (triangles), for $\theta = 0°$ and $\theta = 60°$ are included, in order to demonstrate a good agreement between theoretical and experimental data.

It is evident that for small magnetic fields the $\zeta(\theta)$ values for different polar angles are indistinguishable, reducing tremendously the angular sensitivity of the magnetometer based on $S = 1$ defects in the sub-millitesla range. This drawback is not of importance for $S = 3/2$ systems, since the angle is deduced from the relative peak positions and not from the quadratic shift.

Before a comparison of the achievable resolutions with both systems will be elaborated, two further measurements at $\theta \approx 61°$ and $\theta = 90°$ should be considered, in order to reveal further advantages of the presented technique. These are depicted in Figure 4.9 along with corresponding simulations.

The case $\theta \approx 61°$, as depicted in Figure 4.9a is close to the aforementioned "magic angle"$\approx 54.7°$ when one expects the inner ODMR resonances to merge. Indeed, the experimental data shows $\nu_2 - \nu_1 << \nu_4 - \nu_3$. Furthermore, since the magnetic field is significantly inclined from the symmetry axis, the outer resonances ν_3 and ν_4 become much more pronounced. This complicated behavior is reproduced very well in the calculated ODMR spectra of Figure 4.9a.

In the special case $\theta = 90°$ shown in Figure 4.9b, one expects only two peaks, as can be deduced from the energetic level scheme in Figure 4.4. This is well covered by the experimental data, showing a distinct evolution of two peaks with almost equal amplitude. The corresponding simulation resembles the measurement in a strong way.

So far it was shown that the polar angle θ and subsequently the magnetic field strength B of an external magnetic field can be unambiguously determined from one single ODMR measurement for fields in the microtesla range.

The question left to clarify is the achievable resolution of such a vector magnetometer, especially in comparison to the already implemented ones, based on NV-centers. This will be analyzed in the following.

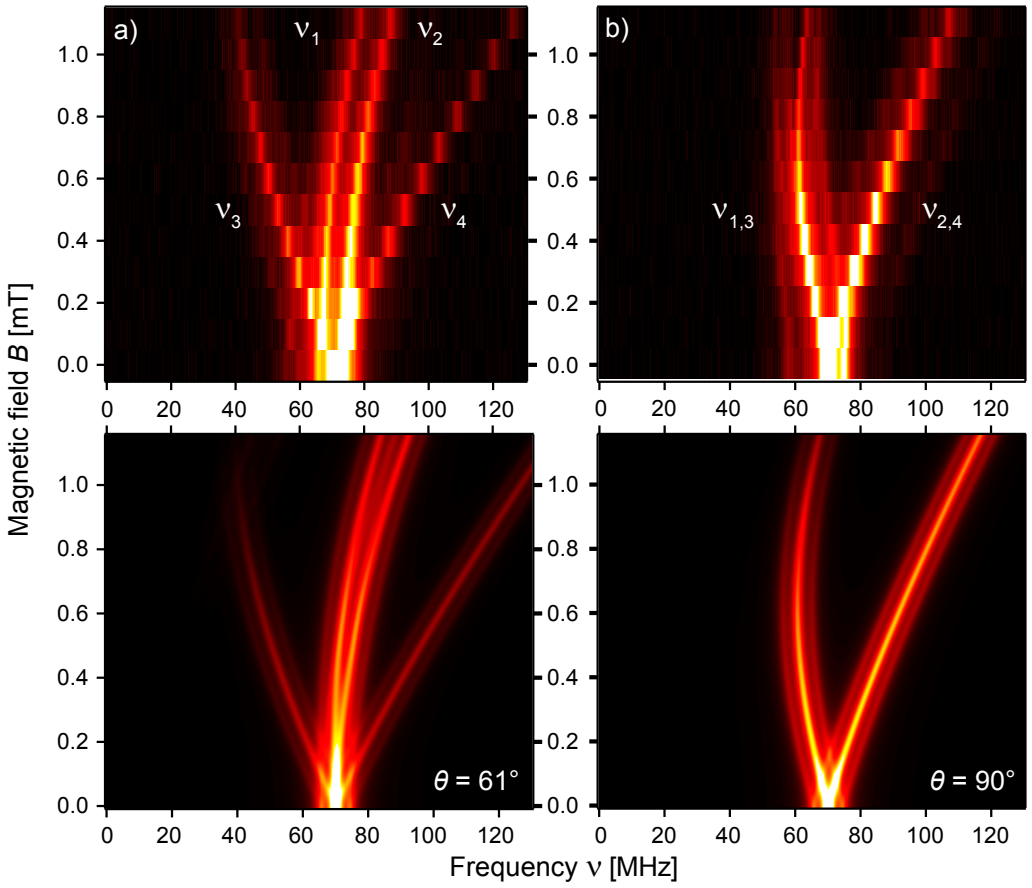

Figure 4.9.: Experimental (top) and calculated (bottom) evolution of the ODMR spectra in magnetic fields applied at an angle $\theta \approx 61°$ (a) and $\theta = 90°$ (b) with respect to the c-axis, showing strong similarity between measurements and simulations.

4.1.3. Resolution

The sensitivity in regard to magnetic field strength δB is dependent on the ability to determine the spectral positions of the peaks $\delta\nu$. These are dependent on the line shape of every peak and, according to Equation 3.6, influenced by the power of the applied radio frequencies P_{RF} and relaxation times T_1 and T_2. As described in [22], the best spectral sensitivity we achieve is $\delta\nu = 100\,\text{kHz}$ with a measurement duration of 8 s per point. Applying

$$\delta\nu = 2g_e\mu_B\delta B/h, \tag{4.23}$$

a general noise-equivalent sensitivity of $\delta B \approx 10\,\mu\text{T}/\sqrt{\text{Hz}}$ is obtained. Compared to common magnetometers from Figure 4.1, the obtained sensitivity is quite competitive to the formerly established techniques. The spatial resolution can be roughly estimated from the illuminated volume by the laser being around $300\,\mu\text{m}^3$.

As stated before, the presented technique is not limited to ensemble measurements and by down-scaling to single defects, same spatial resolution as for single NV-centers in diamond is feasible, for which, however, the magnetic field sensitivity would change. Furthermore, the main advantage of this method lies in the vector magnetometry, i.e. the simultaneous determination of the polar angle θ with respect to the c-axis.
For the NV-center, which is a $S = 1$-system, the polar angle is deduced from the angle dependent non-linear shift of the ODMR lines with the magnetic field. In the experiments, this manifests in a shift of the mean spectral positions of the two peaks (Equation 4.21):

$$h \cdot \frac{\nu_1 + \nu_2}{2} = h\widetilde{\nu} \approx h\nu_0 + \zeta(\theta)B^2. \tag{4.24}$$

Therefore, angle resolution $\delta\theta_{S=1}$ is determined by the accuracy of the quadratic frequency shift measurement $\delta\widetilde{\nu}$:

$$\delta\theta_{S=1} = \frac{1}{|d\widetilde{\nu}/d\theta|}\delta\widetilde{\nu} = \frac{2h\nu_0}{3g_e^2\mu_B^2B^2\sin(2\theta)}\delta\widetilde{\nu}, \tag{4.25}$$

by inserting the formula for $\zeta(\theta)$ from Equation 4.18.
Using $\delta\widetilde{\nu} = g_e\mu_B\delta B/h$, one obtains:

$$\delta\theta_{S=1} = \frac{2}{3\sin(2\theta)} \cdot \frac{h\nu_0}{g_e\mu_B B} \cdot \frac{\delta B}{B}. \tag{4.26}$$

As one can see, the angular sensitivity of this method depends linearly on the zero field splitting $h\nu_0$ and inversely proportional on B^2. Hence, the sensitivity drastically diminishes if $g_e\mu_B B << h\nu_0$. A self-evident improvement would be to apply defects with a smaller zero field splitting: since the ZFS of the NV-center is around 2.87GHz and of the here implemented V_{Si} defects 70 MHz, a tremendous improvement is possible. Indeed, as shown in Figure 4.8c, the angle in the measurements of Figure 4.8a can be determined from the quadratic shift.
For the V_{Si} based magnetometry with $S = 3/2$ the angle is deduced from the relative splittings of the inner and outer peaks $\kappa(\theta)$ as in Equation 4.19. Hence, the angle resolution $\delta\theta_{S=3/2}$ is determined by the accuracy to measure this ratio $\delta\kappa$:

$$\delta\theta_{S=3/2} = \frac{1}{|d\kappa(\theta)/d\theta|}\delta\kappa, \tag{4.27}$$

with $\nu_{in} = \nu_2 - \nu_1$ and $\nu_{out} = \nu_4 - \nu_3$, and subsequently $\kappa = \nu_{in}/\nu_{out}$, one obtains for $\delta\kappa$:

$$\delta\kappa = \sqrt{(\frac{\delta\nu_{in}}{\nu_{in}})^2 + (\frac{\delta\nu_{out}}{\nu_{out}})^2} \cdot \kappa. \tag{4.28}$$

Unlike for the $S = 1$ system, the spectral sensitivity $\delta\nu_{in,out}$ depends on the different amplitudes of the inner and outer peaks as follows:

$$\delta\nu_{in,out} = \frac{2g_e\mu_B\delta B}{h\sqrt{K_{in,out}}}, \tag{4.29}$$

with $K_{in,out}$ being the ODMR contrast of each peak relative to its value at $\theta = 0°$. Hence, as can be seen in Figure 4.5, $K_{in}(0°) = 1$, while $K_{out}(0°) = 0$. Inserting into Equation 4.28:

$$\delta\kappa = \frac{\delta B}{B} \cdot \kappa \cdot \sqrt{\frac{1}{f_{in}^2 K_{in}} + \frac{1}{f_{out}^2 K_{out}}}. \tag{4.30}$$

With

$$\frac{1}{K(\theta)} = \kappa\sqrt{\frac{1}{f_{in}^2 K_{in}} + \frac{1}{f_{out}^2 K_{out}}}, \tag{4.31}$$

the angular sensitivity $\delta\theta_{S=3/2}$ becomes:

$$\delta\theta_{S=3/2} = \frac{1}{K(\theta)\,|d\kappa(\theta)/d\theta|} \cdot \frac{\delta B}{B}. \tag{4.32}$$

Compared to Equation 4.26, the term $h\nu_0/g_e\mu_B B$ is absent, therefore improving the angular sensitivity significantly in weak magnetic fields.

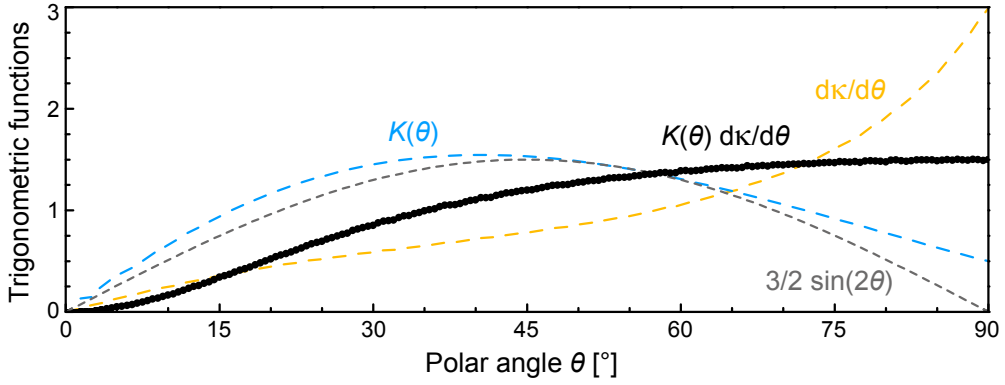

Figure 4.10.: Field-independent trigonometric functions to estimate the polar-angle resolution, according to Equations 4.26 and 4.32.

In order to estimate a value for the angular sensitivity, the trigonometric functions $K(\theta)$ and $|d\kappa(\theta)/d\theta|$ are numerically calculated and presented in Figure 4.10. The highest sensitivity is achieved for $\theta \to 90°$ with $K(\theta) = 0.5$ and $|d\kappa(\theta)/d\theta| = 3$. For the studied case of $B = 800\,\mu T$ we obtain a sensitivity $\delta\theta_{S=3/2} \approx 0.5°/\sqrt{Hz}$ for $\delta B \approx 10\,\mu T/\sqrt{Hz}$. For small angles $\theta < 20°$, the resolution strongly decreases leading to an estimated sensitivity of $\delta\theta_{S=3/2} \sim 9°/\sqrt{Hz}$.

4.2. Resolving the Fine Structure arising from the C_{3v} Symmetry

In Chapter 4.1 it was mentioned that the uniaxial model does not describe the complexity of the C_{3v} symmetry in full. This manifests itself in a deviation of the measured amplitudes of the outer peaks $\nu_{3,4}$ for small angles to the c-axis, as shown in Figure 4.8b. Even at $\theta = 0°$ these peaks are present, while they should vanish in the uniaxial model. While this does not influence the vector magnetometry described in Chapter 4.1, the true energetic structure of the defect nevertheless has to be established, in order to truly understand defects' spin dynamics and relaxation processes, which set limits for the performance of potential devices and to open further implementation areas.
In the following, the fine structure of the V_{Si} ground and excited states in external magnetic fields will be revealed, showing that the C_{3v} point group of the V_{Si} defect gives rise to additional terms in the spin Hamiltonian, which have not been considered so far. A theory of the fine structure will be developed, which precisely takes into account the real atomic arrangement of the vacancy and quantitatively describes the experimental findings.
For the conducted measurements, an isotopically purified sample with over 99.0% of Si atoms being ^{28}Si nuclei with $I = 0$ was fabricated, in order to avoid the hyperfine interaction of the defect electrons with the ^{29}Si-isotopes. This is done by synthesizing polycrystalline SiC from carbon and silicon powders, the latter enriched with ^{28}Si. From this polycrystalline substance, isotope-free 4H-SiC crystals are grown by the sublimation method in a tantalum container [87]. Using common 4H-SiC wafer as substrates, the growth is performed in vacuum at a temperature of 2000° C, with a rate of around 0.25 mm/h. After polishing out the substrate, the final sample with a thickness of about 500 µm is obtained. In order to create silicon vacancies, the sample is irradiated with neutrons in a nuclear reactor with a fluence of $10^{16}\,cm^{-2}$, resulting in a nominal V_{Si} density of $2 \cdot 10^{14}\,cm^{-3}$.

An external magnetic field B parallel to the c-axis splits the Kramers degenerate levels linearly with the magnetic field strength. An energy level diagram including the ground and excited states is presented in Figure 4.11a. In an ODMR experiment with $B = 0$, as depicted in Figure 4.11c, two peaks are detected, at 70 MHz and at around 420 MHz, originating from the zero field splitting of the GS and ES, respectively. Due to the short lifetime of around 6 ns [19], the ES line is only visible at high RF-powers (here 40 dBm).

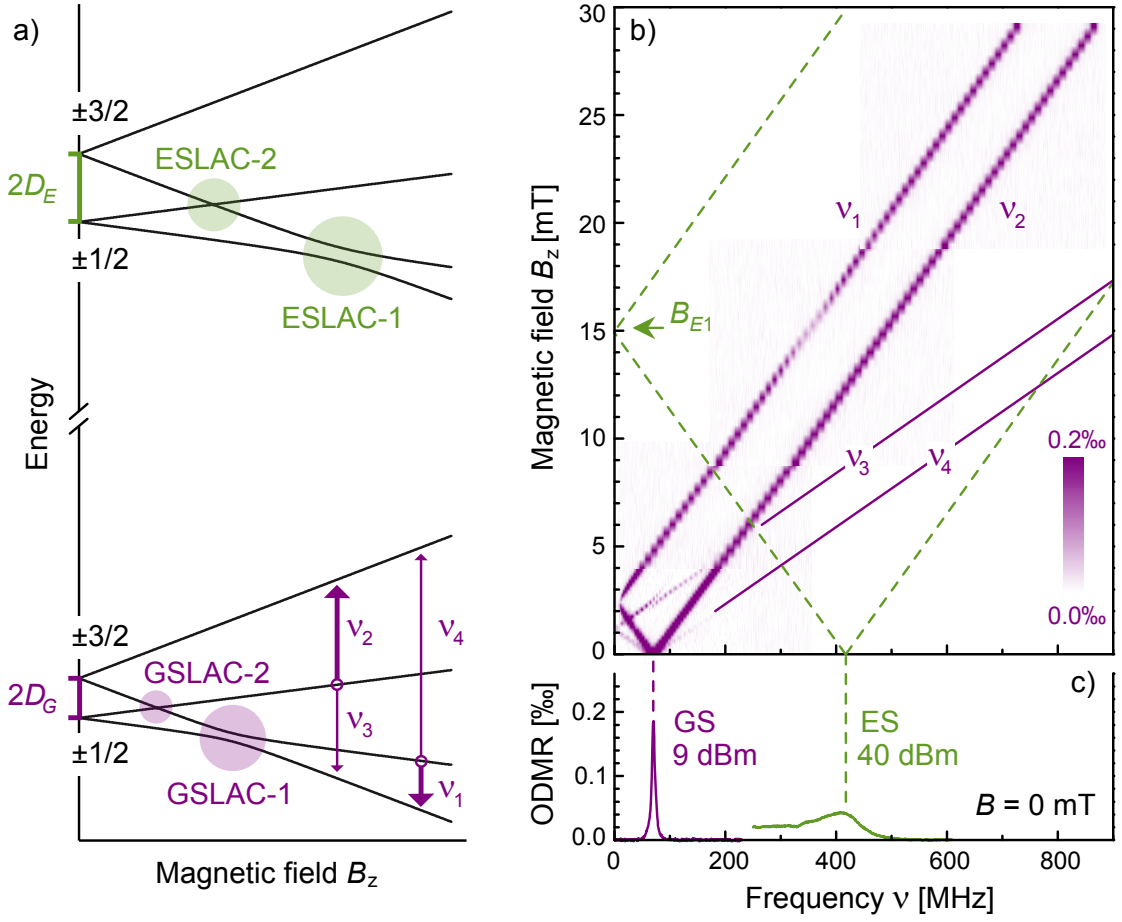

Figure 4.11.: a) Energy diagram of the GS (ZFS = 70 MHz) and ES (ZFS = 420 MHz) evolving in an external magnetic field $B \| c$, with a weak perpendicular component $B_\perp << B_z$. The arrows indicate RF-driven spin transitions, with the thickness denoting the contrast of the corresponding ODMR line in b). For simplicity, the evolution is shown schematically, i.e. B_z and energy axis are not scaled. The semi-transparent circles denote the positions of appearing level anticrossings in the ground and excited states (GSLAC and ESLAC, respectively). b) Evolution of the ODMR signal with the magnetic field along the c-axis. The additional solid and dashed lines denote calculated positions of the ODMR peaks, when the contrast is too low. B_{E1} denotes the magnetic field, at which ESLAC-1 is expected to appear (note the contrast change of the ν_1-line in this area). c) Zero field ODMR spectra of GS and ES at low (9 dBm) and high (40 dBm) RF-power, respectively.

Applying a magnetic field along the c-axis leads to a spitting of these ODMR lines as depicted in Figure 4.11b. While in the uniaxial model two detectable ODMR lines originating from the GS are expected for $B \| c$, the experiment unambiguously shows the presence of four lines, with the outer resonances evolving with twice the slope as the inner ones. The appearance of these peaks due to misalignment of the magnetic field can be excluded: The intensity ratio of ν_3 and ν_1 peaks is around 0.1, which is reached in the uniaxial model not before an angle $\theta = 10°$ (see Figure 4.5). This value is by an order of magnitude higher than the precision of the magnetic field orientation as described in Chapter 3.5.

Additionally, at a magnetic field $B_{G1} = h\nu_0 g_e \mu_B = 2.5\,\mathrm{mT}$, the ν_1 line is expected to reach zero point in the ideal case, due to the level crossing. However, due to inevitable tiny perturbations of the transverse magnetic field component and/or nuclear field, a gap is opening at the crossing point of the energy levels (Figure 4.11a), resulting in the level anticrossing GSLAC-1.

In Figure 4.11b it is also visible with the bare eye, that the intensity of the ν_1 line decreases at around 15 mT, while the ν_2 intensity seems to stay the same. From the green dashed line it is evident that at this magnetic field, the calculated low frequency ES ODMR line tends to zero due to ESLAC-1 (Figure 4.11a), assuming the effective g-factor $g_e \approx 2.0$.

From this observation, the ES fine structure can be reconstructed: The appearance of the dip in the ν_1 rather than in the ν_2 line unambiguously determines the order of the spin sub-levels in the ES, i.e. the $M_S = \pm 3/2$ state having higher energy than the $M_S = \pm 1/2$ state (positive zero field splitting $2D_E$ in ES).

By comparing the intensities $I(\nu_{1,2})$ of the ν_1 and ν_2 lines from Figure 4.11b in dependence on B_z, two further dips can be resolved. As depicted in Figure 4.12a, one is at $B = 2.5\,\mathrm{mT}$, coinciding with GSLAC-1 and the second at $B = 1.25\,\mathrm{mT}$, coinciding with GSLAC-2. The appearance of these dips is explained by the altered optical pumping cycle in the vicinity of LACs (GS and ES), which results in a change of the PL intensity of the corresponding transition, as has been reported for other systems and techniques [88, 89, 90, 91, 92, 93].

To verify this statement, a PL measurement in dependence on the magnetic field B_z without an application of RF-fields is conducted. In order to increase the sensitivity, the dc magnetic field is modulated by creating a small additional oscillating field $\Delta B \cos(2\pi f_m t)$ with the Helmholtz coils. The correspondingly oscillating PL signal is locked-in, with the measurement outcome representing the first derivative of the PL on B_z. The experimental curve, recorded at a modulation frequency $f_m = 5\,\mathrm{kHz}$ with a modulation depth $\Delta B = 83\,\mu\mathrm{T}$, is presented in Figure 4.12b.

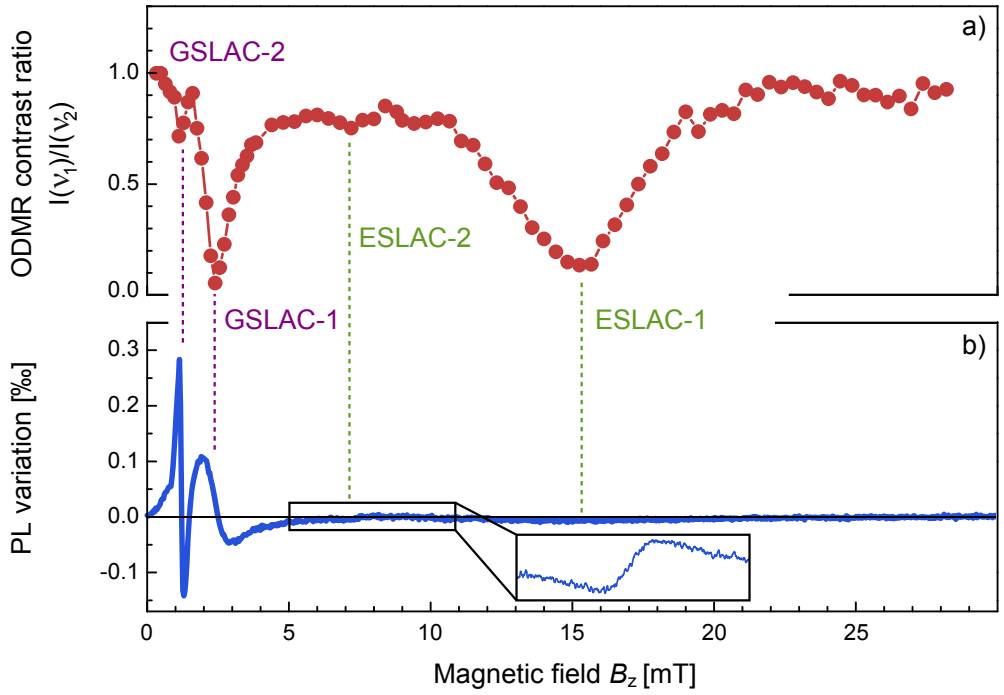

Figure 4.12.: a) ODMR contrast ratio $I(\nu_1)/I(\nu_2)$ of the ν_1 and ν_2 lines as a function of magnetic field B_z along the c-axis. The contrast exhibits dips at magnetic positions coinciding with the positions of GS and ES anticrossings. b) Lock-in detection of the change in PL (without RF) as a function of the dc magnetic field B_z due to an additional weak oscillating magnetic field $\Delta B\cos(2\pi f_m t)$. Inset: high resolution measurement of the range, where ESLAC-2 is expected.

The PL variations in the vicinity of LACs are clearly visible. Additionally to resonances coinciding with GSLAC-1 and 2, also a signal at the calculated ESLAC-2 position is resolved in the inset to Figure 4.12b. The line corresponding to ESLAC-1 cannot be resolved, since its width exceeds by far the modulation depth of the applied magnetic field.

All in all, the LACs can be detected without RF, simply by monitoring the PL intensity as a function of B_z.

So far, it was shown that in an external magnetic field, two LACs appear in the GS and also two in the ES. Regarding the GS ODMR signal, it is splitting into four resonance lines even for $B\|$c, which cannot be explained by the uniaxial model.

These results unambiguously show that in order to resolve the appearing signal attributes, the uniaxial model is not sufficient and a whole new approach to the spin structure of the V_{Si} defect is needed.

Therefore, the findings will be explained in the framework of the spin Hamiltonian, which precisely takes into account the real microscopic C_{3v} group symmetry of the defect.

The effective Hamiltonian $\mathscr{H}$ can be built up from three contributions:

$$\mathscr{H} = \mathscr{H}_0 + \mathscr{H}_{1\parallel} + \mathscr{H}_{1\perp}, \tag{4.33}$$

with $\mathscr{H}_0$ being the Hamiltonian in zero field, and, to the first order in the magnetic field, $\mathscr{H}_{1\parallel} \propto B_z$, $\mathscr{H}_{1\perp} \propto B_\perp$ are the terms induced by the magnetic field.

The Hamiltonian components are constructed applying the theory of group representations [94]. This was conducted in collaboration with colleagues from the Ioffe Institute in St. Petersburg, with the extensive calculation path described in the shared publication [95]. Since this thesis is concentrating on the experimental results, the final form of the Hamiltonian will be discussed.

This is assembled to:

$$\begin{aligned}
\mathscr{H}_0 &= D\left(S_z^2 - \frac{5}{4}\right), \\
\mathscr{H}_{1\parallel} &= \left[g_\parallel S_z + g_{2\parallel} S_z \left(S_z^2 - \frac{5}{4}\right) + g_{3\parallel} \frac{S_+^3 - S_-^3}{4i}\right] \mu_B B_z, \\
\mathscr{H}_{1\perp} &= g_\perp \mu_B \mathbf{S}_\perp \mathbf{B}_\perp + 2 g_{2\perp} \mu_B \left\{\mathbf{S}_\perp \mathbf{B}_\perp, S_z^2 - \frac{3}{4}\right\} + g_{3\perp} \mu_B \frac{\left\{S_+^2, S_z\right\} B_+ - \left\{S_-^2, S_z\right\} B_-}{2i}.
\end{aligned} \tag{4.34}$$

Here, $S_{x,y,z}$ are the spin-3/2 operators as established in Equation 4.2, $\mathbf{S}_\perp = (S_x, S_y)$ is the transverse spin component in regard to c-axis coinciding with the z-axis of the laboratory system, $S\pm = S_x \pm i S_y$, $B\pm = B_x \pm i B_y$ and $\{A, B\} = (AB + BA)/2$ is the symmetric product.

The difference $g_\parallel - g_\perp$, as well as the non-zero values of D, $g_{2\parallel}$, and $g_{2\perp}$ origin in the non-equivalence of the z-axis and the perpendicular axes. The g-factors $g_{3\parallel}$, and $g_{3\perp}$ come from the trigonal pyramidal symmetry of the defect. The six g-factors are linearly independent in a structure of the C_{3v} point group and can be determined from experimental ODMR data. For this cause, several experiments have been conducted.

To obtain the values of the parallel g-factors $g_\parallel$ and $g_{2\parallel}$ the case $B\parallel$c from Figure 4.11b is analyzed.

Application of a magnetic field along the c-axis leads to the splitting of the spin sublevels $M_S = \pm 1/2$ and $M_S = \pm 3/2$ as:

$$\begin{aligned}
E_{\pm 1/2} &= -D \pm \frac{1}{2} g_{\parallel,1/2} \mu_B B_z, \\
E_{\pm 3/2} &= D \pm \frac{3}{2} g_{\parallel,3/2} \mu_B B_z,
\end{aligned} \tag{4.35}$$

with effective g-factors:

$$\begin{aligned} g_{\parallel,1/2} &= g_{\parallel} - g_{2\parallel}, \\ g_{\parallel,3/2} &= \sqrt{(g_{\parallel} + g_{2\parallel})^2 + g_{3\parallel}^2}. \end{aligned} \tag{4.36}$$

In the ideal case of non-transverse magnetic field, the sub-level $M_S = -3/2$ crosses $M_S = +1/2$ at a magnetic field B_{G2} and the $M_S = -1/2$ sub-level at B_{G1}:

$$\begin{aligned} B_{G1} &= \frac{4D}{(3g_{\parallel,3/2} - g_{\parallel,1/2})\mu_B}, \\ B_{G2} &= \frac{4D}{(3g_{\parallel,3/2} + g_{\parallel,1/2})\mu_B}. \end{aligned} \tag{4.37}$$

From Figure 4.12, the magnetic fields B_{G1} and B_{G2}, corresponding to the GSLAC-1 and GSLAC-2, respectively, are deduced. The determined ratio $B_{G2}/B_{G1} = 0.503 \pm 0.005$, independent of the magnetic field calibration, allows to extract the value of $g_{2\parallel}/g_{\parallel}$:

$$\frac{B_{G2}}{B_{G1}} \approx \frac{1}{2} + \frac{3g_{2\parallel}}{4g_{\parallel}} + \frac{3g_{3\parallel}^2}{16g_{\parallel}^2}. \tag{4.38}$$

Neglecting for the first iteration the term $\propto g_{3\parallel}^2$, one obtains $g_{2\parallel} = 0.0 \pm 0.1$.
From the energetic splitting of the sub-levels in Equation 4.35, the evolution of the four appearing ODMR lines with the magnetic field is given by:

$$\begin{aligned} h\nu_{1,2} &= h\nu_0 \pm \left(\frac{3}{2}g_{\parallel,3/2} - \frac{1}{2}g_{\parallel,1/2}\right)\mu_B B_z \approx h\nu_0 \pm \left(g_{\parallel} + 2g_{2\parallel} + \frac{3g_{3\parallel}^2}{4g_{\parallel}}\right)\mu_B B_z, \\ h\nu_{3,4} &= h\nu_0 \pm \left(\frac{3}{2}g_{\parallel,3/2} + \frac{1}{2}g_{\parallel,1/2}\right)\mu_B B_z \approx h\nu_0 \pm \left(2g_{\parallel} + g_{2\parallel} + \frac{3g_{3\parallel}^2}{4g_{\parallel}}\right)\mu_B B_z. \end{aligned} \tag{4.39}$$

With the obtained value $g_{2\parallel} = 0.0 \pm 0.1$, the value of $g_{\parallel}$ is extracted from the slope of the ODMR lines in Figure 4.11b, confirming $g_{\parallel} \approx 2.0$ to the second digit accuracy, in agreement with earlier studies [37].
In order to obtain the transverse g-factors $g_{\perp}$ and $g_{2\perp}$, a measurement with the magnetic field perpendicular to the c-axis is analyzed. In this case, the energy values are given by:

$$\begin{aligned} E_{\pm 1/2} &= \pm\frac{1}{2}(g_{\perp} - g_{2\perp})\mu_B B_{\perp} - \frac{1}{2}\sqrt{[2D \mp (g_{\perp} - g_{2\perp})\mu_B B_{\perp}]^2 + 3[(g_{\perp} + g_{2\perp})^2 + g_{3\perp}^2]\mu_B^2 B_{\perp}^2}, \\ E_{\pm 3/2} &= \pm\frac{1}{2}(g_{\perp} - g_{2\perp})\mu_B B_{\perp} + \frac{1}{2}\sqrt{[2D \mp (g_{\perp} - g_{2\perp})\mu_B B_{\perp}]^2 + 3[(g_{\perp} + g_{2\perp})^2 + g_{3\perp}^2]\mu_B^2 B_{\perp}^2}. \end{aligned} \tag{4.40}$$

As shown in Figure 4.9 of Chapter 4.1.2, for $B \perp c$, two ODMR peaks are expected. From the energetic level evolution of Equation 4.40 these are calculated up to quadratic terms of $B_\perp$ as:

$$h\nu_{1,2} = h\nu_0 \mp (g_\perp - g_{2\perp})\mu_B B_\perp + \frac{3[(g_\perp + g_{2\perp})^2 + g_{3\perp}^2]}{2h\nu_0}\mu_B^2 B_\perp^2. \tag{4.41}$$

An actual measurement is presented in Figure 4.13a. As elaborated in Chapter 4.1.1, the quadratic shift of the lines can be deduced from the mean value $(\nu_1 + \nu_2)/2$. It can be represented in dependence on the Zeeman splitting of the two lines $\nu_2 - \nu_1 = 2(g_\perp - g_{2\perp})\mu_B B_\perp / h$, as follows from Equation 4.41:

$$\frac{\nu_1 + \nu_2}{2} - \nu_0 = \frac{3[(g_\perp + g_{2\perp})^2 + g_{3\perp}^2]}{8(g_\perp - g_{2\perp})^2} \cdot \frac{(\nu_2 - \nu_1)^2}{\nu_0} \approx \left(1 + \frac{4g_{2\perp}}{g_\perp} + \frac{g_{3\perp}^2}{g_\perp^2}\right) \cdot \frac{3(\nu_2 - \nu_1)^2}{8\nu_0}. \tag{4.42}$$

The experimental values of $(\nu_1 + \nu_2)/2$, plotted against $3(\nu_2 - \nu_1)^2/8\nu_0$, along with a linear fit, are presented in Figure 4.13b. By again neglecting in the first iteration terms $\propto g_{3\perp}^2$, the value for $g_{2\perp}$ is obtained from the linear fit with a slope of 0.995 ± 0.010 to $g_{2\perp} = 0.0 \pm 0.1$. Subsequently, analogous to the determination of $g_\parallel$, from the evolution of the peaks in Figure 4.13, the value for $g_\perp \approx 2.0$ is confirmed.

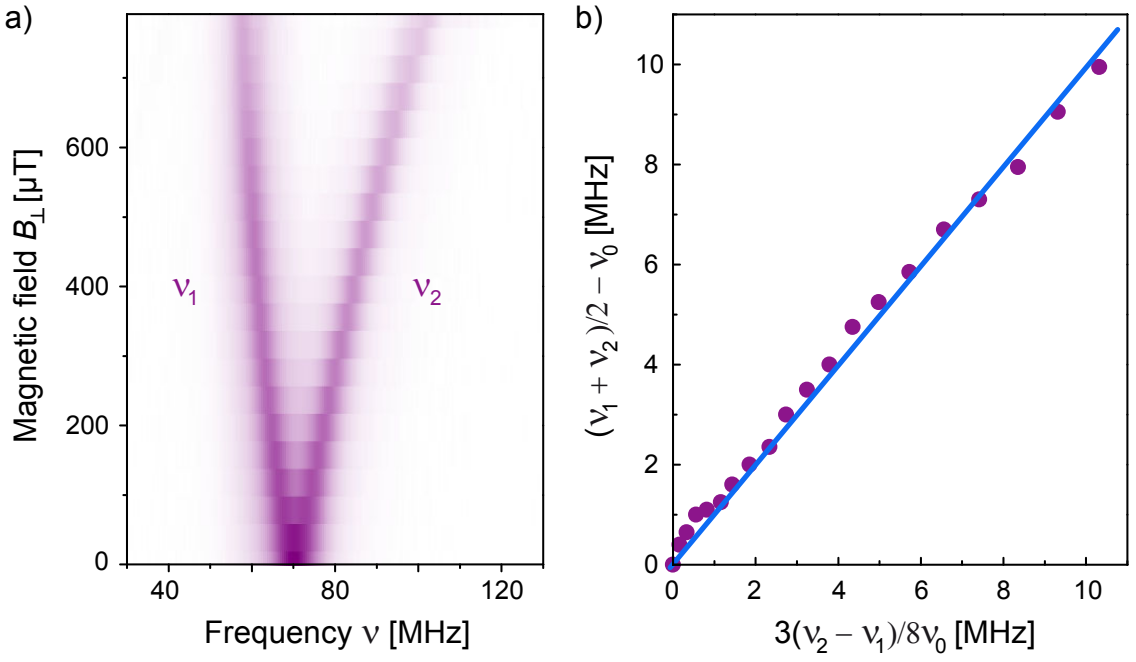

Figure 4.13.: a) Evolution of the ODMR signal as a function of a magnetic field $B \perp c$. b) Quadratic shift measurement (points) $(\nu_1 + \nu_2)/2$ in dependence on the Zeeman splitting represented as $3(\nu_2 - \nu_1)^2/8\nu_0$. Solid line is a linear fit according to Equation 4.42.

Last but not least, the values $g_{3\parallel}$ and $g_{3\perp}$ are determined from the spectral positions of the GSLACs in dependence on a weak perpendicular field.
As described by the Hamiltonian in Equation 4.34, due to the perpendicular component $B_\perp$, anticrossings of energy levels appear, manifesting themselves as spectral gaps, i.e. turning points of ν_1 and ν_3 lines not reaching 0 MHz. For $\mu_B B_\perp << D$, the corresponding splittings Λ_1 and Λ_2 scale linearly with the perpendicular field.
Up to linear terms in $g_{2\parallel}$, $g_{2\perp}$ and quadratic terms in $g_{3\parallel}$ and $g_{3\perp}$, this splittings are given by:

$$\begin{aligned}\Lambda_1 &\approx \sqrt{3}\left(1+\frac{g_{2\perp}}{g_\perp}-\frac{g_{3\parallel}g_{3\perp}}{g_\parallel g_\perp}-\frac{g_{3\parallel}^2}{8g_\parallel^2}\right)g_\perp\mu_B B_\perp,\\ \Lambda_2 &\approx \sqrt{3}\left(\frac{g_{3\perp}}{g_\perp}+\frac{g_{3\parallel}}{2g_\parallel}\right)g_\perp\mu_B B_\perp.\end{aligned} \tag{4.43}$$

Hence, by monitoring the spectral position of the turning points of the ν_1 and ν_3 lines, the g-factors $g_{3\perp}+g_{3\parallel}/2$ and $g_{3\perp}-g_{3\parallel}/2$ can be extracted.
For this reason, the evolution of the ODMR spectra with the longitudinal magnetic field component $B_z\parallel$c in vicinity of the GSLACs is analyzed at different transverse components $B_\perp$. The result is presented in Figure 4.14. In the case of $B_\perp = 0$, as seen in Figure 4.14a, the ν_1 and ν_3 lines can be clearly resolved, as well as their turning points ν_1^{AC} and ν_3^{AC}, corresponding to GSLAC-1 and GSLAC-2, respectively. The alignment uncertainty of the magnetic field is $\delta\theta \approx 1°$ resulting in a potential transverse magnetic field of $\delta B_\perp = B_z \sin(\delta\theta)$. Therefore, in the vicinity of GSLAC-2 the transverse component is at most $\delta B_\perp \approx 22\,\mu$T. Such a small uncertainty cannot explain the appearance and the relative intensity of the ν_3 line in the uniaxial model. Also, the possibility of a hyperfine interaction with nearby nuclei, causing the appearance of the ν_3 line can be neglected, since the intensity of the ν_3 line is the same in the experiments presented here and in the previous Chapter 4.1, while the abundance of the spin carrying ^{29}Si nuclei differs by a factor of five between the used samples.
The point of interest now is the behavior of the turning points ν_1^{AC} and ν_3^{AC} at increasing $B_\perp$, which are direct measures of the level splittings. The corresponding measurements are presented in Figure 4.14b. It is evident, that with increasing transverse component $B_\perp$, the ν_1^{AC} and ν_3^{AC} values are shifting towards higher frequencies, but with different slopes. This becomes even more clear in Figure 4.14c, where the extracted values are depicted as a function of $B_\perp$.

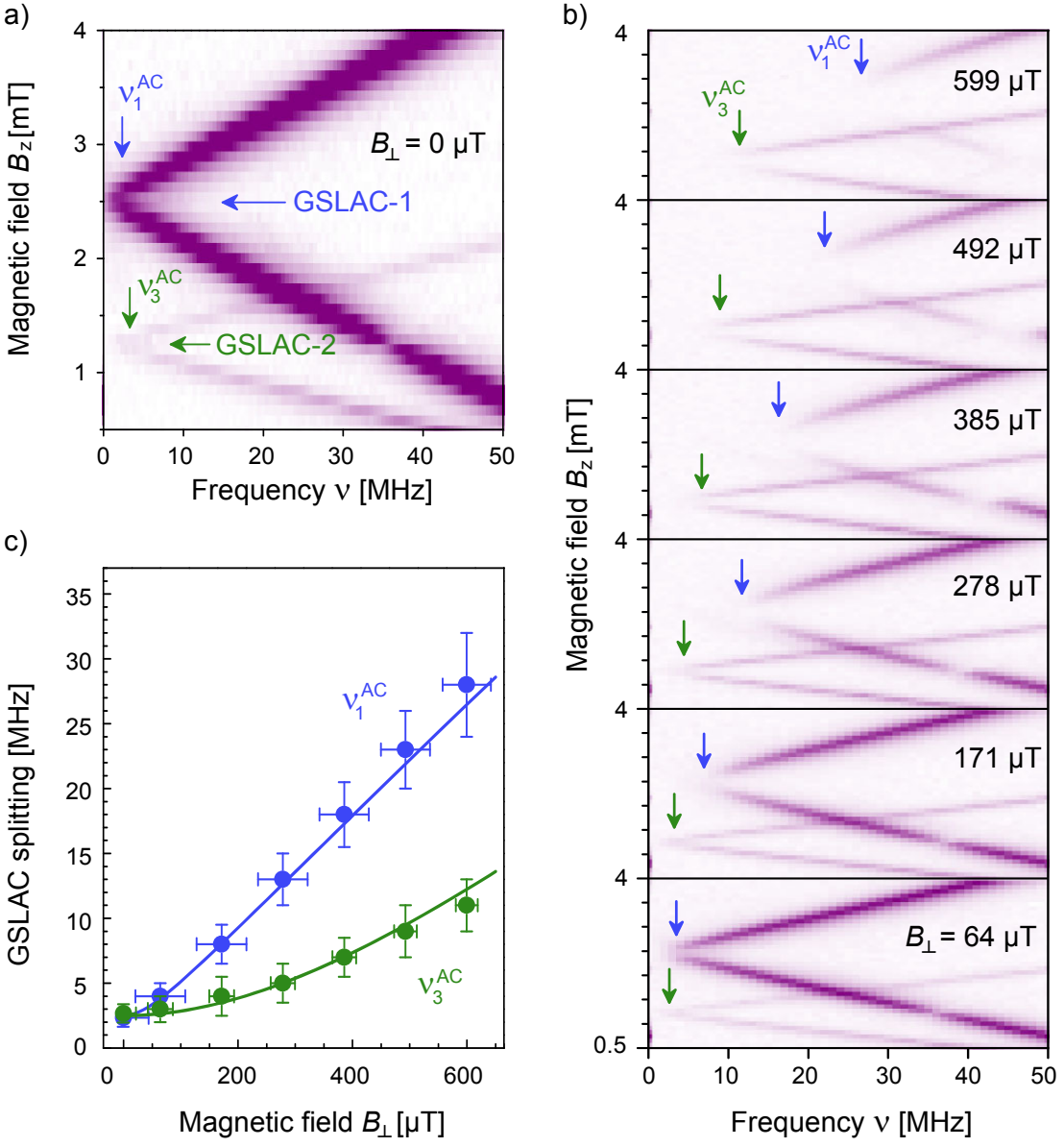

Figure 4.14.: Evolution of the ν_1 and ν_3 ODMR lines in the vicinity of GSLACs in dependence on the magnetic field B_z with no perpendicular magnetic field component $B_\perp$ (a) and with $B_\perp$ up to 600 µT (b). The arrows indicate the turning points ν_1^{AC} and ν_3^{AC}, which are direct measures of the level splittings at GSLAC-1 and GSLAC-2, respectively. c) The GSLAC splittings ν_1^{AC} and ν_3^{AC} as a function of $B_\perp$. Solid lines represent calculations described in the main text.

In order to extract the remaining g-factors, the data is fitted according to Equation 4.43 as $h\nu_{1,3}^{AC} = (\Lambda_{1,2}^2 + \Lambda_0^2)^{1/2}$, with $\Lambda_0/h = 2.5$MHz accounting for the finite ODMR linewidth and inhomogeneity. From the fits, the values $g_{3\perp} + g_{3\parallel}/2 = 0.5 \pm 0.2$ and $g_{3\perp} - g_{3\parallel}/2 = -0.1 \pm 0.4$ are extracted.

Finally, all the determined g-factors are summarized in Table 4.1.

$g_{2\parallel}$	$g_{2\perp}$	$g_{3\perp}+g_{3\parallel}/2$	$g_{3\perp}-g_{3\parallel}/2$
0.0 ± 0.1	0.0 ± 0.1	0.5 ± 0.2	-0.1 ± 0.4

Table 4.1.: The experimentally determined g-factors in Hamiltonian 4.34, which, together with the zero-field splitting $2D = 70\,\text{MHz}$ and $g_\parallel = g_\perp \approx 2.0$, describe the GS fine structure of the V_{Si} defect in an external magnetic field.

With all the work done so far, the appearance of the ν_3 and the ν_4 line in the ODMR spectra also for $B_\perp = 0$ can be understood. From the Hamiltonian in Equation 4.34, the allowed magnetic dipole transitions are calculated to:

$$\begin{aligned} M_{\mp 1/2,\mp 3/2} &= \frac{\sqrt{3}}{2}\left(1+\frac{g_{2\perp}}{g_\perp}\right) g_\perp \mu_B B_{1,\sigma^\mp}, \\ M_{\pm 1/2,\pm 3/2} &= -i\frac{\sqrt{3}}{2}\left(\frac{g_{3\perp}}{g_\perp}+\frac{g_{3\parallel}}{2g_\parallel}\right) g_\perp \mu_B B_{1,\sigma^\pm}. \end{aligned} \tag{4.44}$$

$M_{\mp 1/2,\mp 3/2}$ denote the matrix elements of the transitions $(-1/2 \rightarrow -3/2)$ and $(1/2 \rightarrow 3/2)$, while $M_{\pm 1/2,\mp 3/2}$ represent the $(1/2 \rightarrow -3/2)$ and $(-1/2 \rightarrow 3/2)$ transitions, responsible for the ν_3 and ν_4 lines, respectively. B_1 is the RF magnetic field and $B_{1,\sigma^\mp} = B_{1,x} \mp i B_{1,y}$. Hence, the transitions $(1/2 \rightarrow -3/2)$ and $(-1/2 \rightarrow 3/2)$ occur due to the trigonal pyramidal symmetry of the spin-3/2 defect and are induced by the σ^+ and σ^- circularly polarized RF-radiation. Two microscopic contributions are responsible for these transitions:

- The appearance of the g-factor $g_{3\parallel}$ establishes the coupling of the $M_S = 3/2$ and $M_S = -3/2$ states by the longitudinal static field B_z, as has been shown for related systems [96, 97], allowing the RF-driven transitions with $\Delta M_S = \pm 1$.
- Due to g-factor $g_{3\perp}$, there is also a direct coupling of the $M_S = 3/2$ and $M_S = -1/2$, as well as of the $M_S = -3/2$ and $M_S = 1/2$ states by the transverse RF magnetic field.

From Equation 4.44, the relative intensities of the ν_3 and ν_1 lines for a linearly polarized RF-field are:

$$\frac{\left|M_{1/2,-3/2}\right|^2}{\left|M_{-1/2,-3/2}\right|^2} \approx \frac{(g_{3\perp}+g_{3\parallel}/2)^2}{4}. \tag{4.45}$$

With the experimentally obtained value $g_{3\perp} + g_{3\parallel}/2 = 0.5 \pm 0.2$ from Table 4.1, the relative signal intensity in Equation 4.45 is expected to be 0.063 ± 0.025. The measured value of $I(\nu_3)/I(\nu_1) = 0.09 \pm 0.02$ coincides very well with the theoretical value, justifying the calculated Hamiltonian in Equation 4.34 and experimental verification.
All in all, using the theory of group representations, a Hamiltonian, describing the phenomena appearing in the ODMR spectra of the V_{Si} defect in 4H-SiC, was reconstructed. Especially the appearance of four GS ODMR transitions and the opening of spectral gaps can now be explained. With the experimentally determined values of the g-factors summarized in Table 4.1, the new established Hamiltonian can be written in the matrix form as follows:

$$\mathscr{H} = \begin{vmatrix} D + \frac{3}{2} g_{\parallel} \mu_B B_z & \frac{\sqrt{3}}{2} g_{\perp} \mu_B B_- & -i\frac{\sqrt{3}}{2} g_{3\perp} \mu_B B_+ & -i\frac{3}{2} g_{3\parallel} \mu_B B_z \\ \frac{\sqrt{3}}{2} g_{\perp} \mu_B B_+ & -D + \frac{1}{2} g_{\parallel} \mu_B B_z & g_{\perp} \mu_B B_- & i\frac{\sqrt{3}}{2} g_{3\perp} \mu_B B_+ \\ i\frac{\sqrt{3}}{2} g_{3\perp} \mu_B B_- & g_{\perp} \mu_B B_+ & -D - \frac{1}{2} g_{\parallel} \mu_B B_z & \frac{\sqrt{3}}{2} g_{\perp} \mu_B B_- \\ i\frac{3}{2} g_{3\parallel} \mu_B B_z & -i\frac{\sqrt{3}}{2} g_{3\perp} \mu_B B_- & \frac{\sqrt{3}}{2} g_{\perp} \mu_B B_+ & D - \frac{3}{2} g_{\parallel} \mu_B B_z \end{vmatrix}. \tag{4.46}$$

These new findings, especially the appearance of GSLAC-2, are opening the path for a novel technique to measure magnetic field strengths in the range of nanotesla, without a need for RF excitation. This technique will be elaborated in the following.

4.3. All-optical Nanotesla Magnetometry

The technique described here utilizes the appearance of GSLAC-2, depicted in Figure 4.14, even for diminishing small deviations of the magnetic field from the c-axis. As presented in Figure 4.12b, this anticrossing can be detected without any application of RF-fields, since the monitored photoluminescence abruptly changes in the vicinity of the GSLACs. In Figure 4.12b it is clearly seen that the biggest change in lock-in detected photoluminescence occurs around the magnetic field of GSLAC-2, B_{G2}.
Therefore, following sensing procedure is proposed. At first, a bias magnetic field with the strength B_{G2} from Equation 4.37, coinciding with the position of the GSLAC-2, is applied, establishing a reference photoluminescence for the lock-in detection. Then, the PL intensity is monitored through the lock-in in-phase photovoltage U_X, which is proportional to the deviation of the magnetic field to be measured from the bias field B_{G2}, provided this deviation is small. Hence, by the analysis of the photoluminescence change from its value at B_{G2}, the magnetic field of interest can be measured.

The photovoltage U_X is calibrated by applying well-defined sub-µT magnetic fields B_z along the c-axis. The result is presented in Figure 4.15a, with the oscillating field $\Delta B = 200\,\mu T$ and modulation frequency $f_m = 511\,Hz$ (see caption of Figure 4.12). The obtained calibration term is $U_X/(B_z - B_{G2}) = 39\,\mu V/\mu T$. In this measurement, three different magnetic fields $B_z = 45\,nT, 67\,nT$ and $112\,nT$ are applied, leading to the steps denoted by the black line in Figure 4.15a. Each magnetic field strength was measured for 125 s (step width), with 4 s per point. In the measurement, presented by the green line, all the steps are clearly resolvable, confirming a sensitivity of under 100 nT.

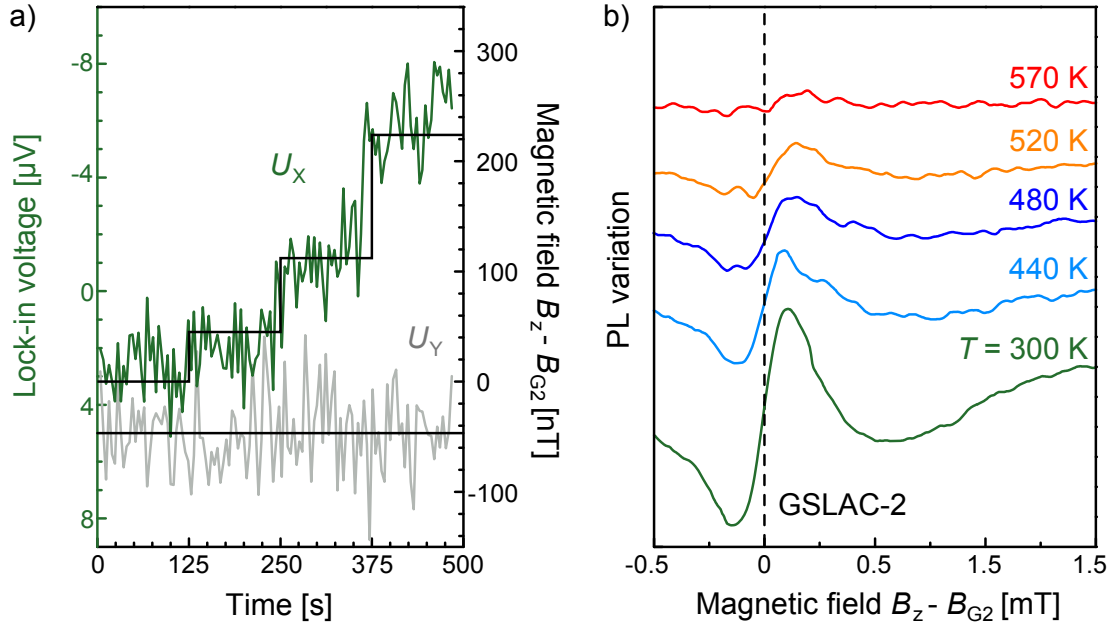

Figure 4.15.: a) Evolution of the in-phase U_X and quadrature U_Y components of the lock-in photovoltage (left axis) with stepwise increase of the magnetic field (right axis), every 125 s, at room temperature. The black lines denote the mean values for each step of U_X and U_Y. b) PL variation in the vicinity of GSLAC-2 ($B_{G2} = 1.25\,mT$) due to a small oscillating field, recorded at different temperatures.

From the quadrature component U_Y of the lock-in signal (gray line), which is independent of the magnetic field, the noise level is estimated. Considering the measurement parameters, a noise-equivalent sensitivity of $\delta B_z = 87\,nT/\sqrt{Hz}$ is achieved.
In order to test the robustness of this method towards ambient conditions, measurements of the PL around GSLAC-2 at various temperatures are performed. This is depicted in Figure 4.15b: While the slope and hence the sensitivity of the magnetic field detection decreases with temperature, a change in PL in vicinity of GSLAC-2 can be detected up to over 520 K.

In the experiments presented so far, an isotopically purified crystal was used, in order to exclude possible contributions from the hyperfine interaction with ^{29}Si nuclei to the Hamiltonian in Equation 4.33. Nevertheless, the proposed all-optical magnetometry can also be performed using commercially available SiC wafers with natural isotope abundance, as presented in Figure 4.16a. By aligning the bias magnetic field along the symmetry axis, it is possible to clearly separate the spin-carrying isotope contributions.

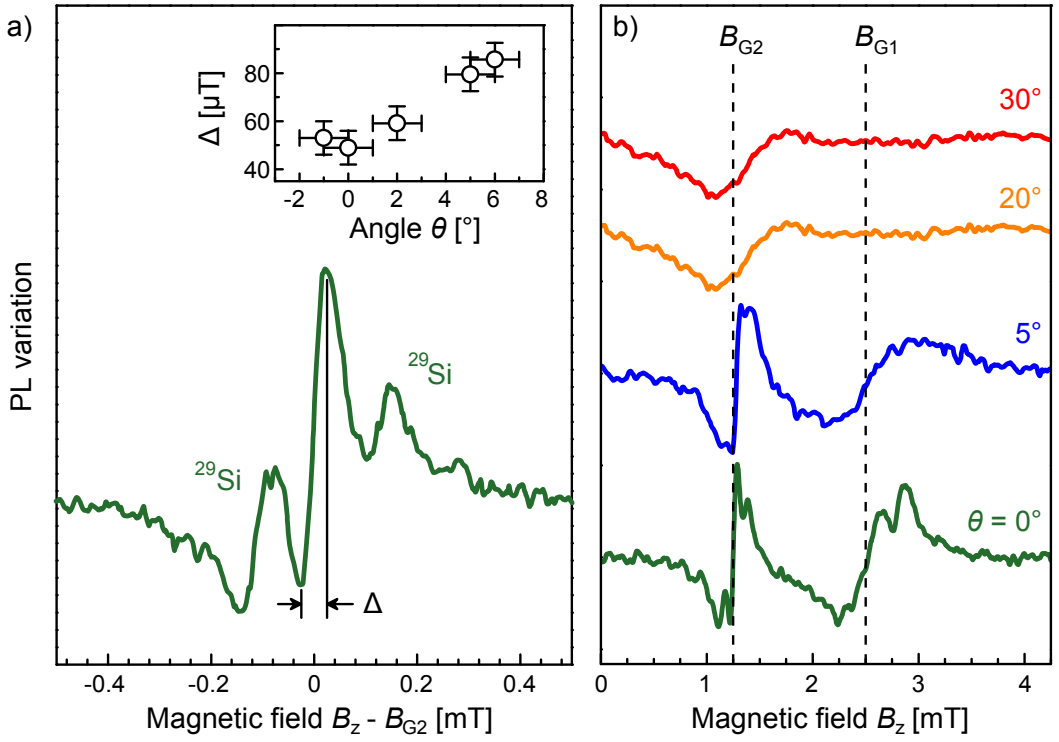

Figure 4.16.: a) PL variation in the vicinity of GSLAC-2, analogous to Figure 4.15b, but performed on a sample with natural isotope abundance. Due to the hyperfine interaction with ^{29}Si nuclei, satellite resonances appear. Inset: The peak-to-peak width Δ change with the angle θ of the magnetic field to the c-axis. b) PL variation at GSLAC-1 (B_{G1}) and GSLAC-2 (B_{G2}) for various angles θ. The non-zero peak-to-peak width for $\theta = 0°$ is ascribed to ambient magnetic fluctuations (nuclear spins and paramagnetic impurities), as well as to the magnetic field alignment uncertainty of 1°.

Since the appearance of GSLAC-2 is a unique property of spin-3/2 and higher spin systems, the achieved sensitivity cannot be reached with spin-1 defects like NV-center in diamond, where the GSLAC-1 would be utilized. From Figure 4.14c, as well as from Equation 4.43 it is visible that GSLAC-2 is generally narrower than GSLAC-1 ($\Lambda_2 < \Lambda_1$), making the spin-3/2 defect more sensitive to magnetic fields and more robust against misalignment than spin-1 systems. To underline this point, measurements in magnetic fields tilted by various angles from the c-axis are performed.

The measurements, conducted again in a sample with natural isotope abundance, are presented in Figure 4.16b. It can be clearly seen that while the photoluminescence change at GSLAC-2 is persistent up to an angle of 30°, the GSLAC-1 signal vanishes already under 20°.
An important aspect for industrial devices is the dynamic range of the magnetometer. Here, it is limited to several tens of μT, defined by the peak-to-peak width Δ of the resonance. As depicted in the inset to Figure 4.16a, it can be extended by applying a small transverse magnetic field, however, lowering the sensitivity. The loss in sensitivity with the increasing transverse field component $B_\perp$ can be found from the inset to Figure 4.16a, where the linewidth Δ is plotted against small inclinations θ of the magnetic field. From $\theta = \arcsin(B_\perp / B_{G2})$, it is empirically obtained:

$$\delta B_z(\theta) = \delta B_z(0) \cdot (1 + 7.2 \frac{B_\perp}{B_{G2}}), \tag{4.47}$$

with $\delta B_z(0)$ denoting the sensitivity when B_z is perfectly aligned along the c-axis. From the angle uncertainty in our experiments of 1°, a transverse field of $B_\perp \approx 22\,\mu\text{T}$ is possible, resulting in a sensitivity change of 13%. To align the magnetometer, several measurements around B_{G2} in differently oriented bias fields have to be conducted, until the maximal slope is obtained.
The proposed method relies only on the completely RF-free PL detection and therefore can be also used with the ESLACs or, in general, on systems with short spin lifetimes. For instance, ESLAC-2 is not observable in the ODMR measurements (Figure 4.11b), however can be clearly resolved by the here introduced technique (inset to Figure 4.12b).
In order to further improve the field sensitivity, several approaches are compilable. One of them is the improvement of the signal to noise ratio, which can be significantly increased by a modification of the irradiation fluence, to create more defects in the same volume. This way, the V_{Si} density can be increased by more than 2 orders of magnitude [19], and the projected sensitivity in this case is a few $\text{nT}/\sqrt{\text{Hz}}$ within the same volume of $\sim 300\,\mu\text{m}^3$.
By utilizing light-trapping waveguides in bigger samples [98], the collection efficiency can be improved by several orders of magnitude: For a waveguide of 3 mm x 3 mm x 300 μm and a V_{Si} density of $4 \cdot 10^{16}\,\text{cm}^{-3}$, the projected noise limit is estimated to be below $100\,\text{fT}/\sqrt{\text{Hz}}$. To actually obtain such a high sensitivity, drift-compensation schemes [99, 98] and magnetic noise screening, similar to optical magnetometry with vapor cells [100], will be necessary.

Last but not least, by using completely spin-free substrates of high crystalline quality, containing only ^{28}Si and ^{12}C isotopes, further improvement due to absence of magnetic fluctuations caused by nuclear spins is expected.
In summary, an all-optical dc magnetometry method, utilizing unique properties of the spin-3/2 V_{Si} defect is introduced, allowing to measure weak magnetic variations in a certain direction with exceptional sensitivity.
The distinct properties of the fine structure of the V_{Si} defect, allow not only for a magnetic field sensing but also a simultaneous thermometry. This will be elaborated in the next chapter.

4.4. All-optical Millikelvin Thermometry

A variety of contact-less techniques, utilizing temperature dependent features in Raman spectra of micro-fabricated chips [101, 102] or temperature dependent change in PL of quantum dots [103], nanocrystals [104] or fluorescent proteins [105], are widely used for temperature sensing with high spatial resolution. With a typical temperature resolution of several hundreds of mK and lower, these sensors are crucial for various applications in biology and physics, like mapping of biochemical processes inside living cells or examining heat dissipation in electronic circuits [106, 107].
A temperature sensor based on the quantum-mechanical properties of the NV-center in diamond, utilizing the moderate thermal shift $d\nu_0/dT = -74\,\mathrm{kHz/K}$ of the GS zero-field ODMR line ($\nu_0 = 2.87\,\mathrm{GHz}$ at room temperature), allows for exceptional spatial resolution and achieves a temperature sensitivity of $\delta T = 10\,\mathrm{mK}/\sqrt{\mathrm{Hz}}$ [108, 109, 110]. However, this method relies on the application of high-power RF-fields, which, strongly impacts the temperature of the sample during the measurement.
Here, analogous to the all-optical magnetometry previously presented, an all-optical temperature sensing method is constructed, utilizing the temperature dependence of the zero field splitting $2D_E$ in the excited states of the V_{Si} defect in 4H-SiC.
In Chapter 4.2 it was elaborated, that due to the short lifetime of 6 ns in the ES [19], the direct observation of the associated zero field ODMR line is only possible by application of high-power RF-fields (Figure 4.11c). However, the zero field splitting $2D_E$ in the ES can be measured indirectly: in Figure 4.11b, it can be seen that the ν_1 contrast is diminished in the vicinity of the magnetic field B_{E1}, where ESLAC-1 is expected to appear.
This is confirmed in Figure 4.17b, where the evolution of the ν_1 and ν_2 lines with a magnetic field B_z along the c-axis in vicinity of the expected position of ESLAC-1 ($2D_E = 420\,\mathrm{MHz}$ at room temperature) is plotted.

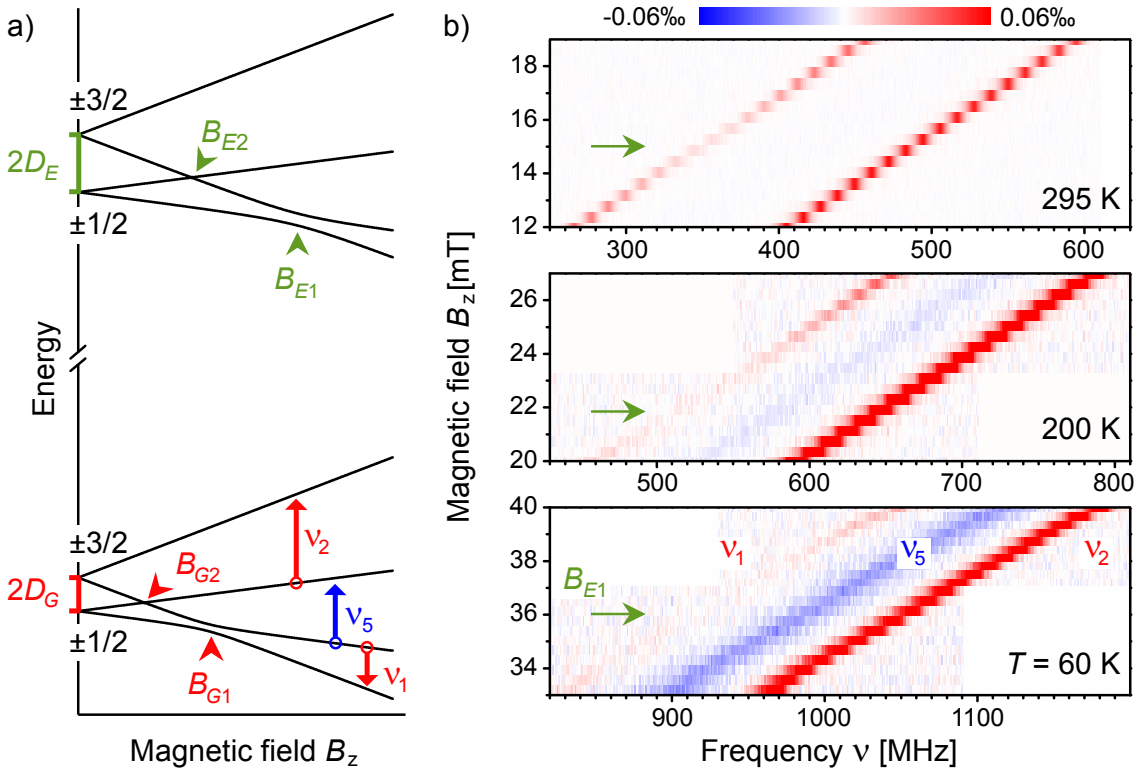

Figure 4.17.: a) Evolution of the GS and ES levels in an external magnetic field $B \| c$, with a weak perpendicular component $B_\perp << B_z$. The arrows indicate RF-driven spin transitions, which are detected in b). b) Magnetic field dependence of the ν_1, ν_2 and ν_5 lines in the vicinity of the ESLAC-1, performed at different temperatures. The arrows indicate the magnetic field B_{E1}, described by the diminishing ODMR contrast of the ν_1 transition.

As expected, the both lines shift linearly in a magnetic field along the c-axis, with a contrast change appearing in the ν_1 line around $B_{E1} = 15.2\,\mathrm{mT}$. The position of the zero field ES ODMR line can be determined from $h\nu_0^{ES} = 2D_E = g_\parallel \mu_B B_{E1}$, while simultaneously, the GS ZFS is directly measured as $2D_G = (\nu_2 - \nu_1)/2$.

From similar measurements at lower temperatures, also presented in Figure 4.17b, a shift of the magnetic field, at which the PL change in the ν_1 line occurs, is observed, implying a thermal shift of ESLAC-1 and hence of the zero-field ES splitting. For $T = 200\,\mathrm{K}$ the ESLAC-1 occurs at $B_{E1} = 21.8\,\mathrm{mT}$, hence shifted by around 6.6 mT from its position at room temperature. This trend continues further for lower temperatures, with $B_{E2} = 36.0\,\mathrm{mT}$ at 60 K. Meanwhile, the splitting between the ν_1 and ν_2 lines does not change with temperature, suggesting that D_G is nearly temperature independent.

For lower temperatures, a further line with a negative contrast is observable, denoted as ν_5. From its spectral position and slope, its origin is ascribed to the $(-1/2 \leftrightarrow 1/2)$ transition, which is normally not resolved in an ODMR experiment.

Its appearance at low temperatures may occur either due to temperature-dependent interaction with phonons or some magnetic field misalignment, which in turn leads to the modification of the inter-system crossing as well as of the optical pumping cycle. Since this line is not of importance to the here presented thermometry method, a further analysis is refrained for future work.
From the ODMR measurements at different temperatures, the thermal shift of the ES zero-field splitting $2D_E$ can be determined. In Figure 4.18 the extracted D_E and D_G values are plotted as filled circles against the ambient temperature.

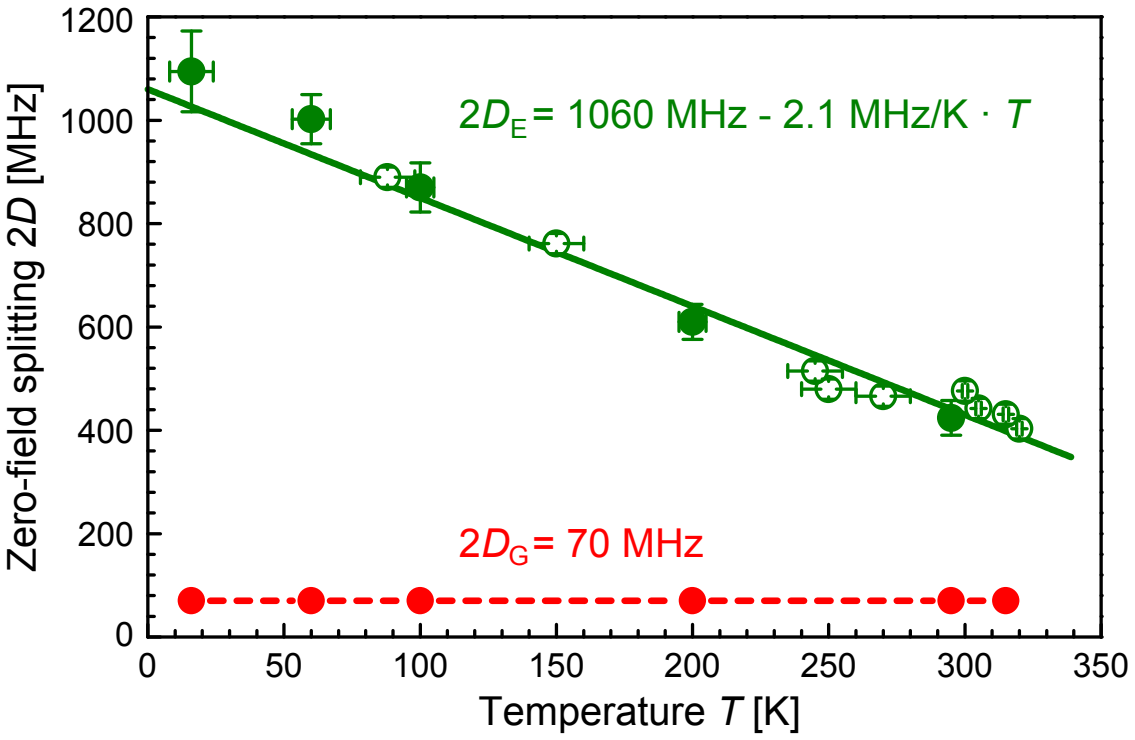

Figure 4.18.: The determined GS ($2D_G$) and ES ($2D_E$) zero field splitting as a function of temperature. Solid symbols denote the values extracted from the ODMR experiments of Figure 4.17, while open symbols are values from the LAC experiments presented in Figure 4.19. The solid green line is a fit of combined $2D_E$ values by Equation 4.48. The dashed red line is to guide the eye.

The evolution of $D_E(T)$ is well fitted to:

$$2D_E(T) = 2D_E(0) + \beta T, \tag{4.48}$$

with $2D_E(0) = (1.06 \pm 0.02)$ GHz denoting the ZFS in the limit $T \to 0$ and $\beta = (-2.1 \pm 0.1)$ MHz/K being the thermal shift. The latter defines the temperature sensitivity, and is by more than an order of magnitude larger than for the NV-defect in diamond [111].

While the observations made so far already constitute to a functioning thermometer, an RF-free technique is desired. Analogous to the all-optical magnetometry, the idea is to exploit the variation of the PL in the vicinity of ESLACs, which, as presented in Figure 4.12b, occurs even without RF-fields. A similar measurement is presented in Figure 4.19 for different temperatures. As in Chapter 4.3, lock-in detection of the PL change, as a function of a dc magnetic field B_z is conducted. Again, a weak oscillating field $\Delta B\cos(2\pi f_m t)$, with $\Delta B = 100\,\mathrm{mT}$ and $f_m = 0.33\,\mathrm{kHz}$ is applied, and the first derivative of the PL change is evaluated. As in Figure 4.12, peaks originating from GSLAC-1, GSLAC-2 and ESLAC-2 are resolved at positions B_{G1}, B_{G2} and B_{E2}, respectively. It is clearly seen that while the GSLAC positions are temperature independent, B_{E2} is shifting towards higher fields with decreasing temperature.

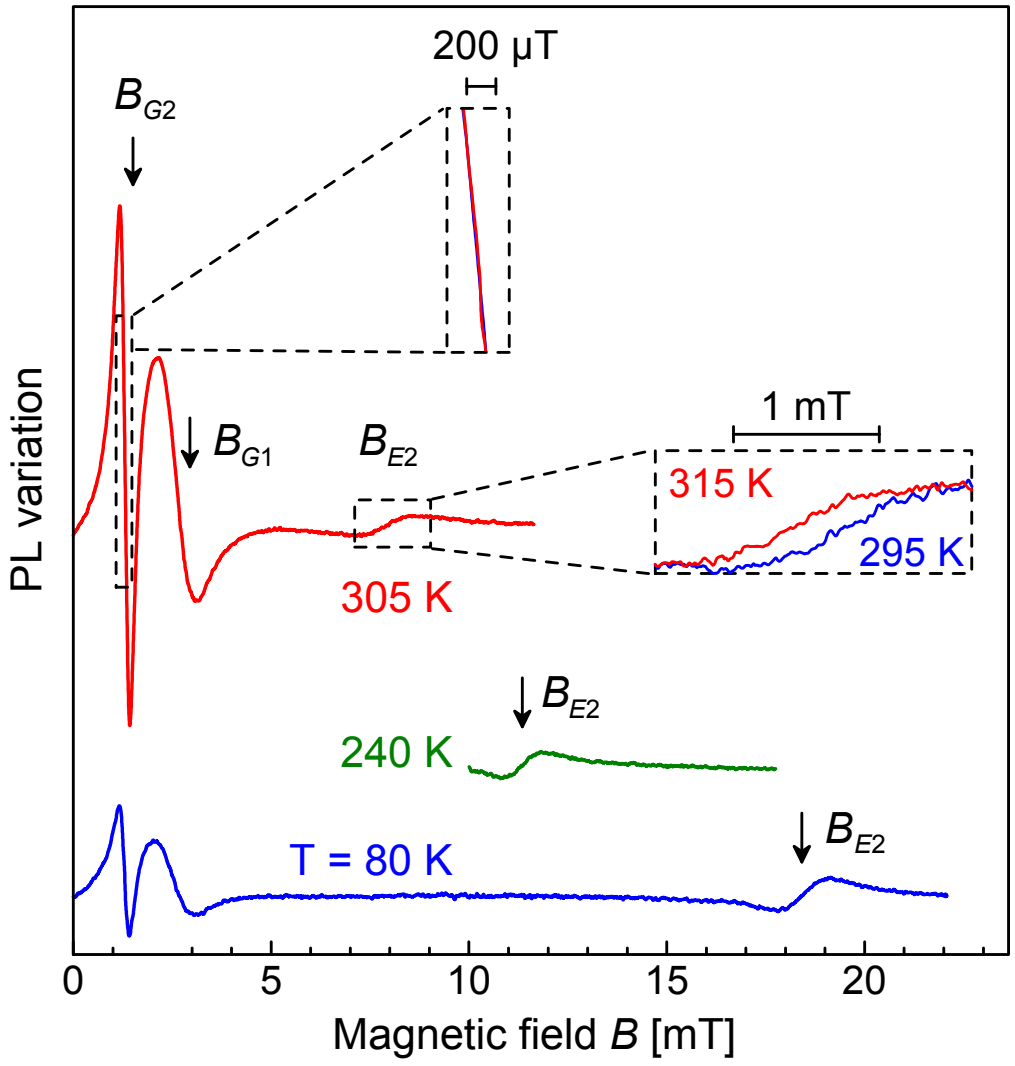

Figure 4.19.: Lock-in detection of the PL variation in dependence on the magnetic field B_z, at different temperatures, caused by a small oscillating field. The arrows indicate magnetic field positions of the LACs.

From the extracted B_{E2} values, $2D_E(T) = 2g_{\parallel}\mu_B B_{E2}$ values are calculated and plotted as open circles in Figure 4.18. Here it is evident that this complimentary data points are well described by Equation 4.48 and are in good agreement with the previously conducted ODMR experiments of Figure 4.17b. Therefore, the observation of the thermal shift of the zero field ES splitting without any RF-fields opens the path for an all-optical thermometry. Due to the aforementioned ES lifetime of 6 ns, an RF-field of about 2 mT would be necessary in order to observe an ODMR signal associated with a similar spin state. To establish such a strong alternating magnetic field without strongly influencing the temperature of the object under measurement would be quite a challenging task.
As has been shown, the GS zero field splitting $2D_G$ and subsequently the position of GSLAC-2, which is used for the all-optical magnetometry, are temperature independent, allowing a simultaneous detection of the magnetic field and the temperature.
The same lock-in detection scheme as in Chapter 4.3 is implemented, with the in-phase lock-in voltage U_X, described at the bias field B_{G2} by (left inset to Figure 4.19):

$$U_X^{G2} = L_{11}\Delta B + L_{12}\Delta T, \tag{4.49}$$

with $L_{11} = -39\,\mathrm{mV/mT}$ determined in Chapter 4.3 and, since B_{G2} is temperature independent $L_{12} \approx 0\,\mathrm{mV/K}$ can be approximated.
At B_{E2}, U_X is written as:

$$U_X^{E2} = L_{21}\Delta B + L_{22}\Delta T, \tag{4.50}$$

with experimentally determined values $L_{21} = 1.8\,\mathrm{mV/mT}$ and $L_{22} = 23\,\mathrm{mV/K}$. The factors L_{ij}, clearly show the ability to measure the magnetic field and temperature separately using GSLAC-2 and ESLAC-2 of the same defect.
While the magnetometry scheme was established in Chapter 4.3, the temperature sensing scheme can be constructed as follows. First, by measuring U_X^{G2} at the bias field B_{G2}, the ambient magnetic field is determined, accounting for ΔB in Equation 4.50. Subsequently, by applying B_{E2} and monitoring U_X^{E2}, the uncertainty due to magnetic noise can be excluded from the thermometry signal and the temperature is calculated with:

$$\Delta T = \frac{1}{L_{22}}\left(U_X^{E2} - \frac{L_{21}}{L_{11}}U_X^{G2}\right). \tag{4.51}$$

As can be deduced from the right inset to Figure 4.19, the dynamic range of such thermometry is $|\Delta T| < 10\,\mathrm{K}$. If the temperature to measure does not lie within this boundary, broad range thermometry is also possible, however with a lower sensitivity.

By scanning the magnetic field from 5 mT to 20 mT and determining B_{E2}, the zero field splitting $D_E = g_{\parallel}\mu_B B_{E2}$ can be calculated and subsequently, the temperature can be determined using the Equation 4.48.
The last question to address is the achievable temperature sensitivity δT. For this, the in-phase and quadrature lock-in signals are measured as a function of time to determine the upper limit for the noise level δU. Using the calibrated L_{ij} values, the temperature sensitivity $\delta T = \delta U / L_{22}$ is calculated. Hence, a sensitivity of $\delta T \approx 100\,\mathrm{mK}/\sqrt{\mathrm{Hz}}$ within a detection volume of approximately $300\,\mu\mathrm{m}^3$ is estimated. By applying the improvements already proposed for the all-optical magnetometry, a temperature sensitivity better than $\delta T \approx 1\,\mathrm{mK}/\sqrt{\mathrm{Hz}}$ is feasible.
In summary, a thermometry method is proposed, utilizing the thermal shift of the ESLAC-2, which can be detected completely RF-free and, by monitoring GSLAC-2, with simultaneous all-optical magnetometry with the same defect.
The achievable sensitivities of quantum metrology are dictated by the coherence times of the spin system. Therefore, in the next chapter the spin-lattice relaxation time T_1, and the spin-spin relaxation time T_2 will be analyzed.

5. Exploring the Coherence Properties

Long quantum coherence in solid-state systems is the ultimate prerequisite for new technologies based on purely quantum phenomena [112, 113]. Particularly, the sensitivity of quantum sensors, as the ones introduced in Chapter 4, scales with the electron spin coherence time [7, 2]. Also, one of the crucial requirements for quantum computing is a proof of the possibility to coherently control the qubits over a long time. Therefore, in order to confirm the V_{Si} defects in SiC as a suitable candidate for various kinds of quantum applications, a thorough analysis of the coherence properties is necessary. This chapter is dedicated to this task.

The coherence properties, particularly the spin-lattice relaxation time T_1 and the spin-spin relaxation time T_2, are determined by techniques widely known from the field of Nuclear Magnetic Resonance (NMR), adapted to the ODMR measurement protocol. The implemented NMR terminology and basic physical principles are well described by de Graaf in [68].

As briefly introduced in Chapter 3.4, by using the pulsed ODMR (pODMR) technique, the spins can be coherently controlled and their state read-out. Unlike the cwODMR technique utilized in the previous chapters, here, the frequency of the radio waves remains fixed at the resonance condition with one of the allowed transitions. For the measurements described below, this is either the $|-1/2\rangle \rightarrow |-3/2\rangle$ or the $|+1/2\rangle \rightarrow |+3/2\rangle$ transition, denoted by ν_1 and ν_2 frequency, respectively, in Chapter 4 (see Figure 4.3) and also in the following. The variable in the measurements to extract coherence times of the defect is either the length of the applied resonant RF-pulses or "the dark" time in between. This is best illustrated by the so-called Rabi measurements, where the resonant RF-pulse length is varied, hence changing the final state of the chosen spin transition. The scheme for an pODMR Rabi measurement is as follows. First a laser pulse of a sufficient length to polarize the spins into the $|\pm 1/2\rangle$ states, is applied. The RF is set to resonance with one particular spin transition, e.g. to 490 MHz for the $|+1/2\rangle \rightarrow |+3/2\rangle$ (ν_2) transition in an external magnetic field along the c-axis of 15 mT. This frequency is also known as the Larmor frequency in NMR. Then, a resonant RF-pulse of a certain length is applied, rotating the electron spin by a certain angle from its initial direction. Subsequently, the photoluminescence is detected.

As described in Chapter 2.3.1 the photoluminescence is spin state dependent. Hence, by repeating this procedure for iteratively increasing RF-pulse lengths, an oscillation in the detected photoluminescence is observed, representing the oscillation of the spin between the two energetic states, driven by the resonant radio frequency.
In Figure 5.1a, the pulse sequence for one iteration is presented, along with the respective spin directions on the Bloch-sphere. It consists of two laser pulses of constant length (10 µs) and two RF-pulses, with one of them being varied in time length every cycle. The laser pulses have two purposes: on the one hand they pump the defect electrons into the $|\pm 1/2\rangle$ state, just like in cwODMR, on the other hand they stimulate the photoluminescence, from which the spin alteration caused by the RF-pulses can be extracted. This read-out is made by averaging the PL values in the first 500ns of the laser pulses, denoted as PL_1 and PL_2. By extending the read-out range, the signal-to-noise ratio can be improved, however, diminishing the contrast due to spin relaxation to equilibrium. Note that this sequence is repeated for every iteration, meaning that the second laser pulse polarizes the electrons before the first RF-pulse.
Since the length of the second RF-pulse is fixed to a constant length, the PL extracted from the second laser pulse is constant and hence serves as the reference value for the PL change caused by the first RF-pulse. In principal, also the PL extracted at the end of the first laser pulse might serve as reference. However, due to heating effects by the laser and the high power RF-pulses, a symmetrical sequence for signal and reference is preferred. Finally, the spin polarization $\mathcal{S} = (PL_1 - PL_2)/(PL_1 + PL_2)$ is plotted against the iterated length of the first RF-pulse τ.
A real measurement is presented in Figure 5.1b for different RF-powers.
As expected, the PL is oscillating with the RF-pulse length τ and is well fitted to:

$$\mathcal{S}(\tau) = -\frac{\Delta PL}{2} e^{-\tau/T_R} \cos(\Omega_R \tau) + C. \tag{5.1}$$

ΔPL is the ODMR contrast, T_R is the decay time, C the offset and Ω_R the Rabi frequency. The latter can be regarded as the Larmor precession of the electron spin around the magnetic component of the resonant RFs B_1 [69]:

$$\Omega_R = \gamma B_1 \sim \sqrt{P(B_1)}, \tag{5.2}$$

with γ being the electron gyromagnetic ratio, and $P(B_1)$ the corresponding RF-power. To verify that the observed oscillations are actually spin transitions, the extracted Ω_R values are plotted against $\sqrt{P(B_1)}$ in Figure 5.1c, showing the expected linear dependence.

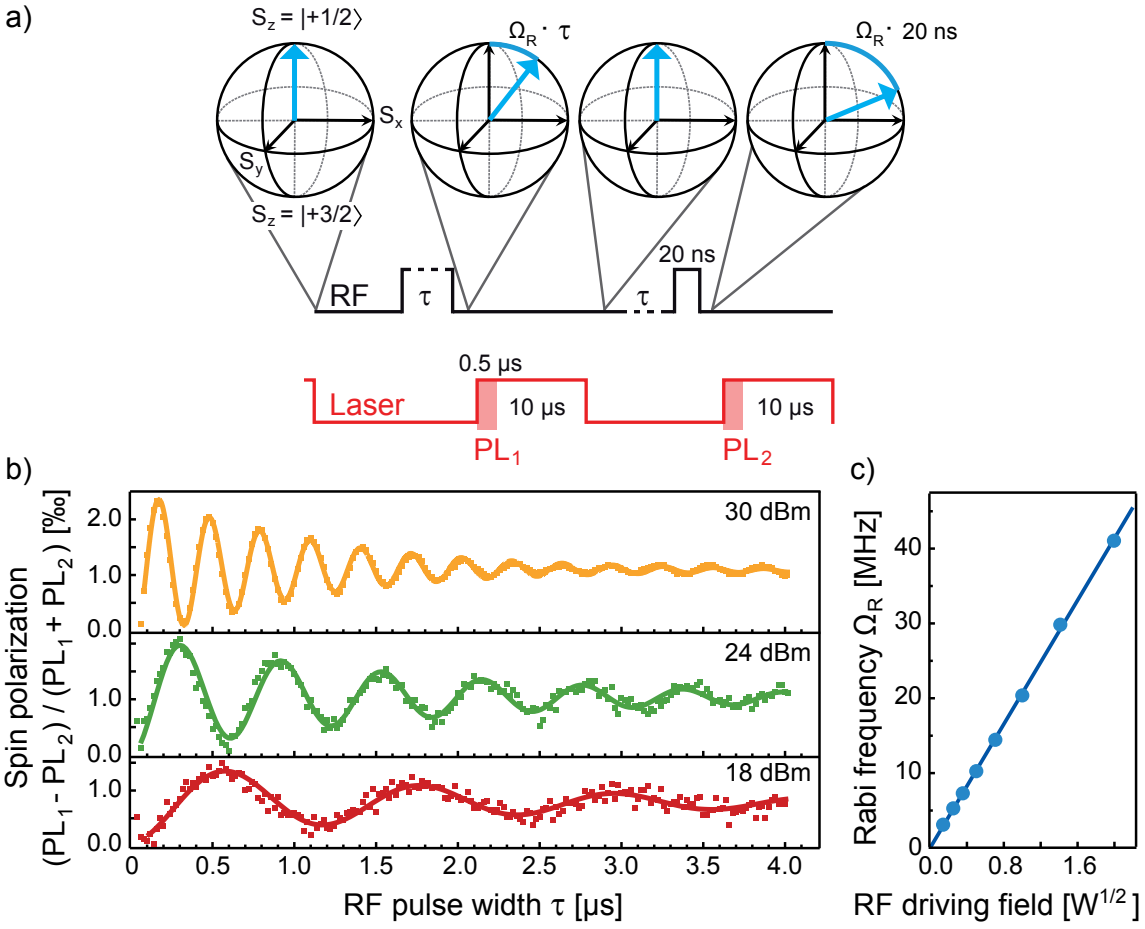

Figure 5.1.: a) Pulse sequence in order to measure Rabi oscillations and the corresponding spin states for the ν_2 transition on a Bloch-sphere. The length τ of the first RF-pulse is iterated, while the second one is constant at 20ns. b) Read-out of the spin polarization as $(PL_1 - PL_2)/(PL_1 + PL_2)$ for different RF-powers. The solid lines are fits to Equation 5.1. c) Extracted Rabi frequencies versus the applied RF-field strength. The solid line is a linear fit according to Equation 5.2.

Next, the setup must be calibrated in order to perform measurements of the T_1 and T_2 times. Particularly, the length of the π pulse, i.e. the pulse which flips the spin exactly around 180°, which is equivalent to a spin transition between the two spin levels, is necessary. Ideally, this pulse should be as short as possible to avoid any relaxations during the spin manipulation. As seen in Figure 5.1b, its length is dependent on the applied RF-power, which is 44 dBm at max with the available frequency generator and amplifier. Hence, a π pulse length of 40ns is chosen, at an RF-power of roughly 38dBm. Note that this value is not fixed, since the actual RF-power at the illumination spot is highly dependent on the strip line behavior and the ambient conditions. Therefore, for every measurement, a Rabi curve calibrating the π pulse to be 40 ns in length has to be conducted. This can be done by extracting the Ω_R value from the fit, which, however, requires post processing of the experimental data and is hence time consuming.

A quicker way to calibrate the RF-power on the fly is by observing the offset C from Equation 5.2. Initially, the second RF-pulse from Figure 5.1a is fixed to 20 ns, i.e. the desired length of the $\pi/2$ pulse. Since the measured PL change is oscillating around the PL value corresponding to the pulse length of $\pi/2$, this offset parameter C must become zero, if the reference PL is fixed to the $\pi/2$ signal. Hence, the RF-power is adjusted until the measured signal is oscillating around and decaying to zero PL.

For measurements in magnetic fields, a further calibration step is needed. While in zero field the resonance frequency is assumed to be constant at $\nu_0 = 70$ MHz for all temperatures (see Chapter 4.4), to precisely find the resonance frequencies $\nu_{1,2}$ in a certain field, preliminary cwODMR measurements are necessary.

Now, the setup is ready to perform further pulsed measurements in order to extract the desired T_1 and T_2 relaxation times of the defect. This will be thoroughly done in the next two chapters. In the first one, the dependence on the ambient conditions, i.e. temperature and magnetic field, is elaborated. In the second, the dependence of the relaxation times on the defect creation is analyzed by comparing electron and neutron irradiated samples with different irradiation fluences. Last but not least, using a dynamic decoupling sequence, a substantial prolongation of the coherence time is shown.

5.1. Dependence on the Magnetic Field and Temperature

In this chapter, the coherence properties of the V_{Si} defects in 4H-SiC will be analyzed in regard to their dependence on the ambient conditions, namely the temperature and the magnetic field strength B_z along the c-axis. For this cause, T_1 and T_2 times were measured in the temperature range from 17 K to 300 K, and in magnetic fields B_z from 0 mT to 31 mT.

The measurements were conducted on the sample #3 in Table 5.2, of the electron irradiated series described in the next Chapter 5.2. It contains natural abundance of ^{29}Si (4.7%) and ^{13}C (1.1%) nuclear spins and an initial V_{Si} concentration of $2 \cdot 10^{13}$ cm^{-3}. In order to increase the signal intensity by higher defect concentration, the sample is irradiated with 2 MeV electrons with a fluence of 10^{17} cm^{-2}. Further sample properties are described in the next Chapter 5.2.

At first, the measurements related to the spin-lattice relaxation time T_1 are presented. This relaxation is due to intrinsic, irreversible processes in the crystal and hence determines the absolute limit for spin coherence [68].

The measurement and post processing follow the technique described in the supplementary of [17]. The pulse sequence is depicted in Figure 5.2a. It contains only one RF-pulse with a length equivalent to a rotation by π, flipping the spin over 180°, hence, exactly from one state to another. The time τ between the RF-pulse and the read-out laser pulse is iterated.

Hence, PL_1 evolution with τ is starting at the value when the electrons are polarized in the $|3/2\rangle$ level, decaying with T_1 towards equilibrium with increasing delay between the RF-pulse and the read-out laser pulse. In the reference, there are no RF-pulses and PL_2 is decaying towards equilibrium from its value at $|1/2\rangle$.

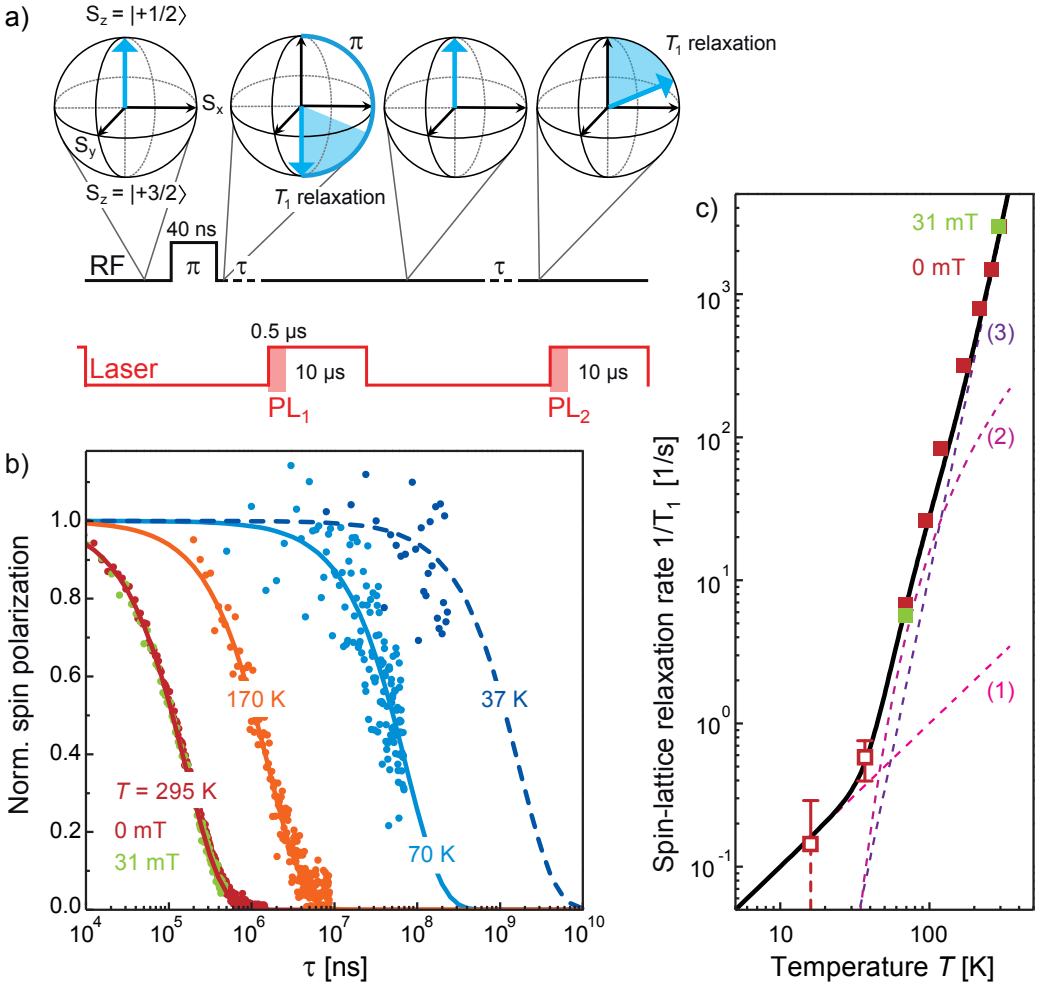

Figure 5.2.: a) Pulse sequence in order to measure the spin-lattice relaxation time T_1. The time τ between the first RF-pulse and the subsequent read-out laser pulse is iterated. In the reference part without RF-pulses, the dark time is iterated. b) Exemplary curves of resulting spin polarization in dependence on τ for different temperatures and magnetic fields. The solid lines are fits to Equation 5.3. The curves are normalized to the maximum of each fit. c) Extracted T_1 values for all measured temperatures and magnetic fields. The solid line is a fit according to Equation 5.4 and the dashed lines (1) - (3) are its most pronounced contributions in the corresponding temperature range, as described in the main text.

A theoretical dependency of the spin polarization $\mathcal{S}$ on the pulse gap τ using this sequence is described as:

$$\mathcal{S} = A \cdot \mathrm{Exp}\left(-\frac{2(\tau - \tau_0)}{T_1}\right) + C, \tag{5.3}$$

with τ_0 accounting for the finite pulse gap of the first iteration and C being the offset due to environmental temperature and magnetic field fluctuations during the measurement.

In Figure 5.2b, exemplary measurements at different temperatures and magnetic fields are shown, with the curves for $B_z \neq 0$ measured in resonance with the ν_2 transition. Here it is evident that the T_1 time continuously increases with lower temperatures, while no difference between the measurements in zero field and at 31 mT is detectable. An additional measurement in $B_z = 20$ mT shows the same evolution. The curves are fitted to Equation 5.3, from which the T_1 values are extracted. The curve for 37 K (and for 17 K, not shown) preserves over 90% of its initial spin polarization in a time span of 1 s, making the acquisition time of the whole exponential decay curve too long. Therefore, here, the linear part of the exponential decay is fitted and a T_1 time estimated with a bigger error margin. At room temperature, the spin-lattice relaxation time is obtained to $T_1 = (340 \pm 30)$ µs and is in accordance with earlier studies within the error margins [17]. From the fits of all measured curves at different temperatures and magnetic fields, the T_1 dependence on these factors is established. This is presented in Figure 5.2c, to account for different additive mechanisms, as spin-lattice relaxation rate $1/T_1$ versus the temperature. Indeed, also at 70 K, no difference between zero field and 31 mT is detected, as also has been reported for the NV center in diamond [114]. On the other hand, a temperature dependence, with the spin-lattice relaxation rate becoming smaller (T_1 longer) with lower temperature is clearly present. The values for the two lowest temperatures 37 K and 17 K are denoted as open squares to underline the extraction of the T_1 value from the linear part of the exponential decay. Therefore, these values must be considered as lower limits for the T_1 time, rather than as a quantitative estimation.

The experimentally obtained values are well described by a power law:

$$\frac{1}{T_1(T)} = A_0 + A_1 T + A_2 T^5 + \frac{A_3}{e^{\Delta/k_B T} - 1}, \tag{5.4}$$

relating to various phonon-assisted, temperature dependent, spin relaxation mechanisms, assumed to be similar to that previously reported for donors in silicon [65] and the NV-center in diamond [114]. Hence, the obtained T_1 values are influenced in different temperature ranges by different phonon interaction mechanisms.

For high temperatures $T > 120$K, thermally excited high-energy phonons result in spin-lattice relaxation via a two-phonon Raman process with $1/T_1 \approx A_2 T^5$ [115]. The respective fit is denoted by the dashed line (3). At intermediate temperatures, an Orbach-like process via a vibrational state may impact the spin relaxation, with the dependency $1/T_1 \propto 1/(e^{\Delta/k_B T} - 1)$ (dashed line (2)) [115].
Here, $\Delta \approx 25$ meV denotes the energy of the local phonon mode at the defect position, which is roughly estimated from the spectral distance of the zero-phonon line and the phonon sideband maximum in the PL spectrum [19].
For the lowest measured temperatures $T < 30$ K, the relaxation through single phonon scattering should be taken into account $1/T_1 \approx A_1 T$ (dashed line (1)) [115]. Also a temperature independent relaxation mechanism, namely the cross relaxation with residual impurity spins $1/T_1 \propto A_0$ might become important at cryogenic temperatures. From the experimental data, the lower limit of the spin-lattice relaxation time is estimated to be at least $T_1(0) = 1/A_0 > 10$ s. All the obtained fitting parameters are listed in Table 5.1.

A_0 [s^{-1}]	A_1 [$K^{-1}s^{-1}$]	A_2 [$K^{-5}s^{-1}$]	A_3 [s^{-1}]
< 0.1	$1.0 \pm 0.2 \cdot 10^{-2}$	$1.1 \pm 0.2 \cdot 10^{-9}$	300 ± 150

Table 5.1.: Relaxation parameters, accounting for different spin-phonon and defect interactions, extracted from the fit to Equation 5.3 of the T_1 values in Figure 5.2c.

To sum up, the spin-lattice relaxation time T_1 was measured at a variety of temperatures and magnetic fields, showing no dependence on B_z at least up to 31 mT. With decreasing temperature, the T_1 time is prolonged from around 340 µs at room temperature to an estimated minimum of at least 10s at cryogenic temperatures. While the measurements in magnetic fields presented here were conducted at the ν_2 resonance, test measurements at the ν_1 lead to the same results.
Next, the dependence of the spin-spin relaxation time T_2 on the temperature T and magnetic field B_z will be elaborated. This time defines the actual coherence time, i.e. the time span in which the spin can be manipulated.
The utilized pulse sequence is depicted in Figure 5.3a and is in accord with common Spin-Echo experiments in NMR. Three RF-pulses with the delay time $\tau/2$ are applied before the read-out laser pulse. The first $\pi/2$ pulse transfers the spin from the $|\pm 1/2\rangle$ state into the transverse plain, a state superposition $(|\pm 1/2\rangle + |\pm 3/2\rangle)/\sqrt{2}$. Due to slight differences in experienced magnetic field and intrinsic differences in environmental conditions, the spins have slightly different Larmor precession frequencies, wherefore the aligned single spin vectors start to dephase.

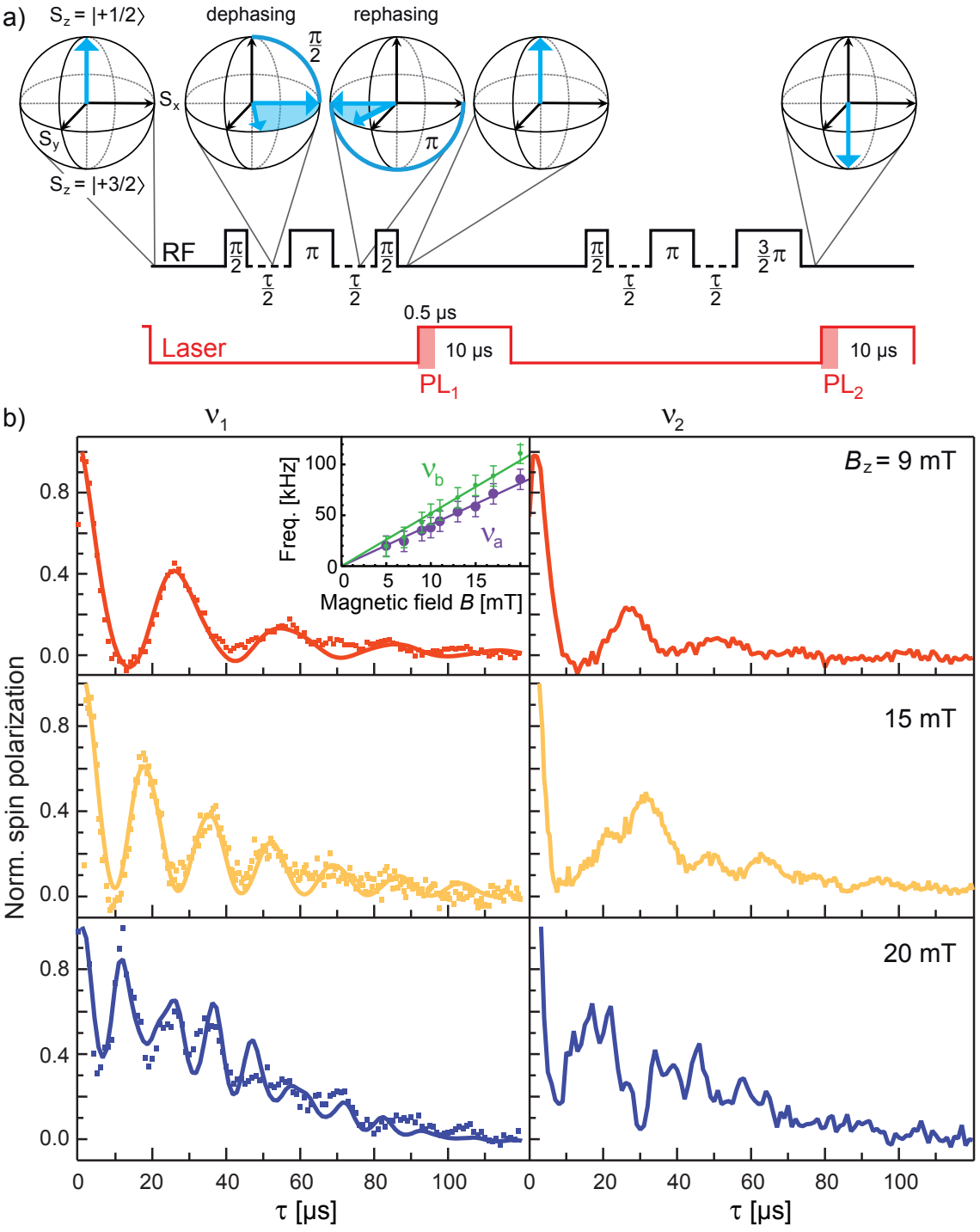

Figure 5.3.: a) Pulse sequence in order to measure the spin-lattice relaxation time T_2. The time gap $\tau/2$ between the RF-pulses is iterated. b) Exemplary curves of resulting spin polarization in dependence on τ for different magnetic fields at room temperature. On the left are the measurements conducted at the ν_1 resonance and the corresponding fits to Equation 5.5. The curves are normalized to the respective maximum of the fit. On the right, the ν_2 measurements are depicted as solid lines. Inset: extracted ESEEM frequencies $\nu_{a,b}$ with a linear fit.

After the iterated time interval $\tau/2$, a π pulse is applied, rotating the spins with their momentary direction by 180° again into the transverse plain. By this pulse, the dephasing tendency is reversed, resulting in a rephasing of the spins, ultimately reaching the initial alignment after time $\tau/2$. In the NMR measurements, which are sensitive to the transverse spin component, the signal of this initial alignment after the time $\tau/2$ is detected.
Since the here presented technique is most sensitive to the longitudinal component, a further pulse is needed to project the spins back into one of the eigenstates $|\pm 1/2\rangle$ and $|\pm 3/2\rangle$. This is done by a $\pi/2$ pulse in the first part of the sequence and, to achieve maximal contrast, a $3\pi/2$ pulse in the reference part. By this Spin-Echo method, the intrinsic spin-spin relaxation time T_2 of the defects is extracted, with the impact by the properties of the measurement setup opted out. Note that since the gaps $\tau/2$ between the pulses are much shorter than the spin-lattice relaxation time, the decoherence process is dominated by the spin-spin relaxation.
This sequence is first applied for $T = 295\,\mathrm{K}$ at different magnetic fields, with the RF being resonant either to ν_1 or ν_2 transition. The measured evolution of the spin polarization with τ is presented in Figure 5.3b. Two striking attributes are resulting from this experiment. First, at $B_z \neq 0$, oscillations are appearing, with their frequencies changing with the magnetic field strength. Furthermore, the curves obtained at the ν_1 and ν_2 lines for the same field strength B_z are not equal, showing slightly diverging oscillation behavior. The appearance of this so-called electron spin echo envelope modulation (ESEEM) is ascribed in this case to the interaction of the electron spins with the $I = 1/2$ nuclear spins of the naturally abundant ^{29}Si and ^{13}C isotopes, as observed in various similar experiments [15, 16, 17, 116].
The experimental data at the ν_1 resonance is fitted by:

$$\mathcal{S} = A \cdot \mathrm{Exp}\left(-\frac{(\tau-\tau_0)}{T_2}\right) \cdot \prod_{j=a,b}\left[1 - B_j \sin^2(\pi \nu_j \tau)\right] + C, \tag{5.5}$$

assuming two frequencies ν_a and ν_b contributing to the ESEEM shape.
The extracted frequencies at different magnetic fields are depicted in the inset to Figure 5.3b. Here it is evident that $\nu_{a,b}$ are evolving linearly with the magnetic field strength B_z and from the linear fit one obtains the slopes as $\nu'_a = 4.1 \pm 0.9\,\mathrm{kHz/mT}$ and $\nu'_b = 5.2 \pm 0.9\,\mathrm{kHz/mT}$. Similar values have been observed in [15] for the divacancy ESEEM in SiC and have been associated with the Larmor precession of the ^{29}Si and ^{13}C nuclear spins.

As seen in Figure 5.3b, the ESEEM for the ν_2 transition shows more complex behavior, which agrees with the earlier reported observations [116]. The origin of the asymmetry in oscillations for the ν_1 and ν_2 transitions has not been completely clarified yet and is a task for future works, while the present thesis mainly focuses on the extraction of coherence times, which are the same at both resonances. Since the applied magnetic fields B_z lie in the vicinity of the excited-state level anticrossing (see Chapter 4.3), the observed asymmetry may indicate dynamic nuclear spin polarization, as described in [117].

From the fits to Equation 5.5, applied to all measured spectra at room temperature for magnetic fields in the range from 0 mT to 31 mT, the T_2 dependence on the magnetic field is obtained. This is depicted in Figure 5.4b.

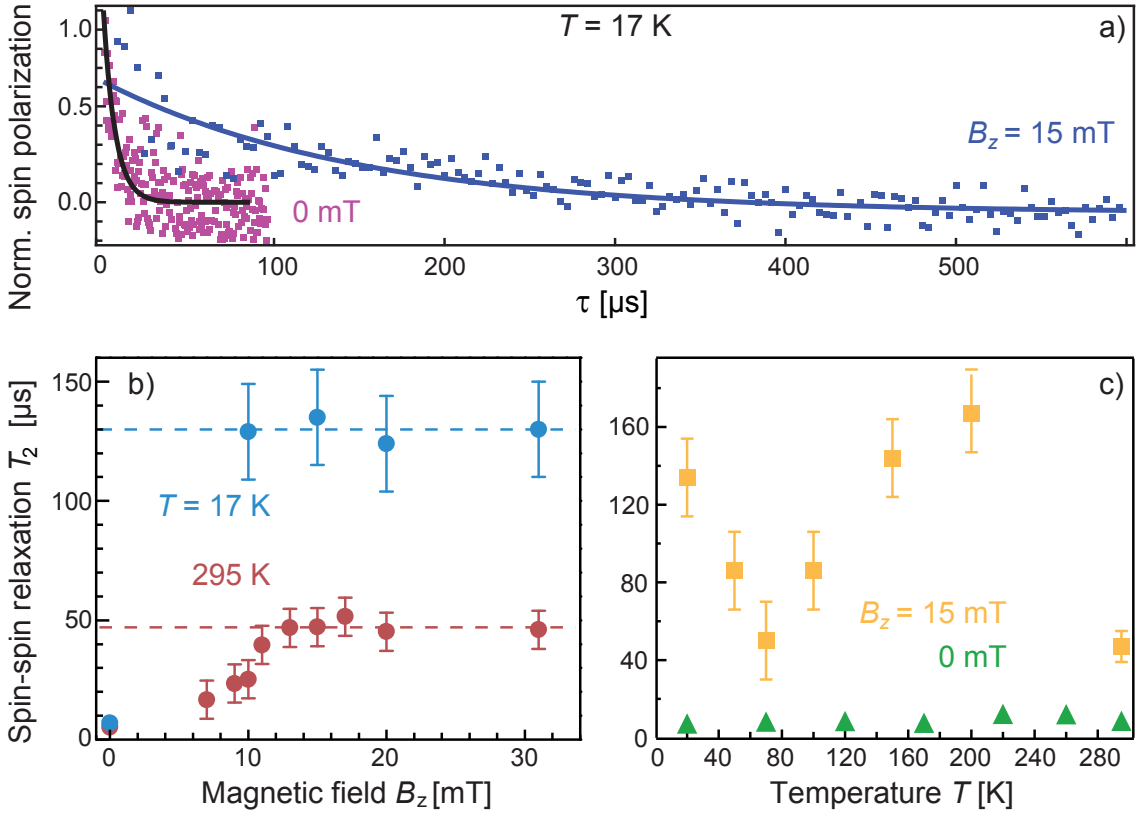

Figure 5.4.: a) Spin polarization in dependence on τ from a Spin-Echo measurement in zero field and $B_z = 15\,\text{mT}$ at $T = 17\,\text{K}$. The solid lines are exponential fits. b) Extracted T_2 values as a function of the magnetic field at room temperature and $T = 17\,\text{K}$. c) Evolution of the T_2 time with temperature in zero field and $B_z = 15\,\text{mT}$.

While in zero field, a T_2 time of $(8 \pm 2)\,\mu\text{s}$ is extracted, the spin-spin relaxation time increases with higher magnetic field and is prolonged to $(47 \pm 8)\,\mu\text{s}$ for $B_z > 11\,\text{mT}$. The maximal value is slightly shorter than the spin coherence time of single V_{Si} centers reported in [17].

The increase in coherence time with magnetic field is theoretically explained in [118] by the suppression of heteronuclear spin interaction of the ^{29}Si and ^{13}C isotopes. In small fields, the Larmor frequencies of the environmental nuclei are very close to each other, whereby reciprocal flip flops can be induced and cause a temporal change in the precession frequency of the V_{Si} electron-spin. This so-called nuclear-induced spectral diffusion is diminished in higher magnetic fields, since the isotope spin-baths are energetically separated [119]. Also, the observed saturation of T_2 is in accord with this theoretical considerations, although the saturation is expected to take place at higher magnetic fields > 30 mT.

The T_2 dependence on the magnetic field is also analyzed at $T = 17$ K. Exemplary curves, obtained at the ν_2 resonance, in zero field and at $B_z = 15$ mT are presented in Figure 5.4a. Due to considerably increased noise, the ESEEM oscillations are not resolved anymore and the data are fitted by a simple exponential decay. The extracted T_2 values are added to Figure 5.4b. The evolution with increasing magnetic field is similar to the one at room temperature, with the same value in zero field of about 8 µs, but a higher saturation value of $T_2 = (134 \pm 20)$ µs. Widmann et al. [17] estimate the T_2 coherence time of a single V_{Si} defect at room temperature and $B_z = 28$ mT to around 160 µs. While the low temperature T_2 value obtained here is in good agreement with this estimation, the room temperature coherence time of $T_2(295\,\text{K}) = (47 \pm 8)$ µs is slightly shorter.

To further investigate this discrepancy, T_2 is measured as a function of temperature, in zero field and $B_z = 15$ mT. The result is depicted in Figure 5.4c. While the T_2 time in zero field stays nearly constant in the applied temperature range, the coherence time at 15 mT is evolving inconsistently. The shorter coherence time at room temperature might be caused by the temperature enhanced nuclear-induced spectral diffusion due to flip-flop interaction of the ^{29}Si and ^{13}C isotopes with $I = 1/2$ [118]. Since the distribution of these isotopes around each V_{Si} defect in the crystal lattice is not homogeneous, the resulting different hyperfine interaction with the V_{Si} electrons might lead to a shortening of the effective coherence time [119], which is not the case for single defects. The second pronounced attribute of the T_2 dependency on the temperature at $B_z = 15$ mT, is a "dip" at around 80 K. Its origin is not completely clarified yet. As has been elaborated in Chapter 4.4, the spectral position of the level anticrossings in the excited state are linearly dependent on temperature. Hence, the temperature at which the ESLACs are occurring at the 15 mT used in the temperature dependent measurements can be calculated with Equation 4.48. While ESLAC-1, as depicted in Figure 4.17, is expected to occur at $B_{E1} = 15$ mT for room temperature, the ESLAC-2 reaches $B_{E2} = 15$ mT at a temperature $T \approx 104$ K.

Therefore, the occurrence of this "dip" might be caused by the vicinity of the ESLAC-2, which is altering the pumping process and the dynamics of the regarded ν_2 transition. For quantitative conclusions, a more thorough analysis of the T_2 temperature dependence, with more measurement points at different temperatures, as well as at different magnetic fields, is necessary and is a task for future work.
In summary, the coherence properties, namely the spin-lattice and spin-spin relaxation times T_1 and T_2 have been analyzed in dependence on the external magnetic field and temperature. While the T_1 time shows no dependence on the magnetic field up to 31 mT, T_2 increases from (8 ± 2) µs in zero field to a saturation level of (47 ± 8) µs for $B_z > 11$ mT at room temperature. T_1 is strongly temperature dependent, with the room temperature value of (340 ± 30) µs increasing to at least 10 s for cryogenic temperatures. The T_2 time shows a non-monotonic temperature dependence, while the saturation level is increased to (134 ± 20) µs at 17 K.
In regard to sensing devices, an optimum of the signal-to-noise ratio, dictated by the amount of excited defects and the coherence times, which define the achievable resolution, must be found. For this reason, the next chapter will address the dependence of T_1 and T_2 on the irradiation process, which creates V_{Si} centers, as well as on the resulting defect density.

5.2. Influence of the Irradiation Type

When irradiating a SiC crystal with neutrons or electrons, the crucial aspect in creating defect ensembles for sensing applications, such as the ones described in Chapter 4, is to find the perfect match between the signal-to-noise ratio and the coherence time, dictating the resolution of a sensing device. In this chapter, the relaxation times of defect ensembles created by electron or neutron irradiation with different fluences will be compared, allowing a subsequent proposal for an optimal defect creation scheme.
For the electron irradiated sample series, a semi-insulating 4H-SiC wafer (2 inch), is purchased from Norstel. Grown by high temperature chemical vapor deposition with no further isotope purification, it contains natural abundance of ^{29}Si (4.7%) and ^{13}C (1.1%) nuclear spins. In this wafer an as-grown V_{Si} concentration of $2\cdot10^{13}$ cm^{-3} is already present. In order to introduce further defects, the wafer is diced into 7 mm x 4 mm samples and irradiated with electron fluences in the range from $1\cdot10^{17}$ cm^{-2} to $5\cdot10^{18}$ cm^{-2}. While for all fluences an electron energy of 2 MeV is used, an additional sample is irradiated with 1 MeV electrons at $1\cdot10^{17}$ cm^{-2}. During the irradiation, the samples are placed on a water cooled copper plate to avoid heating by the electron beam.

Also, two neutron irradiated samples were available with the pristine samples purchased from CREE. A 110 µm thick high purity layer was epitaxially grown on a 2-inch n-type 4H-SiC wafer. On top, a 5 µm n-type and a 2 µm p-type 4H-SiC layers are grown. Diced in 4 mm x 2 mm pieces, the samples are then irradiated in a TRIGA Mark-II nuclear reactor, with neutron energies in the range of 0.18 MeV to 2.5 MeV. The different fluences were achieved by varying the irradiation time and fission power of the reactor. Further information on the reactor is available at [120].
The defect density can be estimated by comparing the PL values with calibrated measurements from the previous work [19], where the defect densities are known. The quantitative dependence of the amount of created vacancies on the fluence has been extensively elaborated in [19] and [70] and is out of scope for the present thesis. However, it must be noted, that this calibration does not reflect the full amount of created defects, but only the luminescent fraction.
The list with all the measured samples is presented in Table 5.2.

sample #	irradiation particle	fluence [10^{17} cm^{-2}]	defect density n_V [10^{14} cm^{-3}]
1	pristine	-	0.2
2	electrons, 1 MeV	1	1.5
3	electrons, 2 MeV	1	3.9
4	"	2.5	8.0
5	"	5	16.3
6	"	7.5	38.8
7	"	10	64.6
8	"	50	90.4
9	neutrons, < 2.5 MeV	0.1	2.5
10	"	1	5.9

Table 5.2.: Attributes of the investigated samples. With the calibrated PL from [19], the created V_{Si} densities are calculated.

All the measurements in this chapter were conducted at room temperature, either in zero magnetic field or at $B_z = 15\,\mathrm{mT}$ along the c-axis. As was elaborated in the previous Chapter 5.1, at this magnetic field, the maximal values of T_2 are reached.
First, the measurements of the spin-lattice relaxation time T_1 will be discussed. The pulse sequence, as depicted in Figure 5.2a, and also all the post-processing follow the method established in Chapter 5.1.
Conducting these measurements on all samples, a dependency of the T_1 time on the defect density and subsequently on irradiation fluence is acquired. Two exemplary curves, one of the neutron and one of the electron irradiated samples, are presented in Figure 5.5b. From the fits to Equation 5.3, T_1 relaxation times are extracted for all examined samples and presented in Figure 5.5c in dependence on the calculated V_{Si} density.

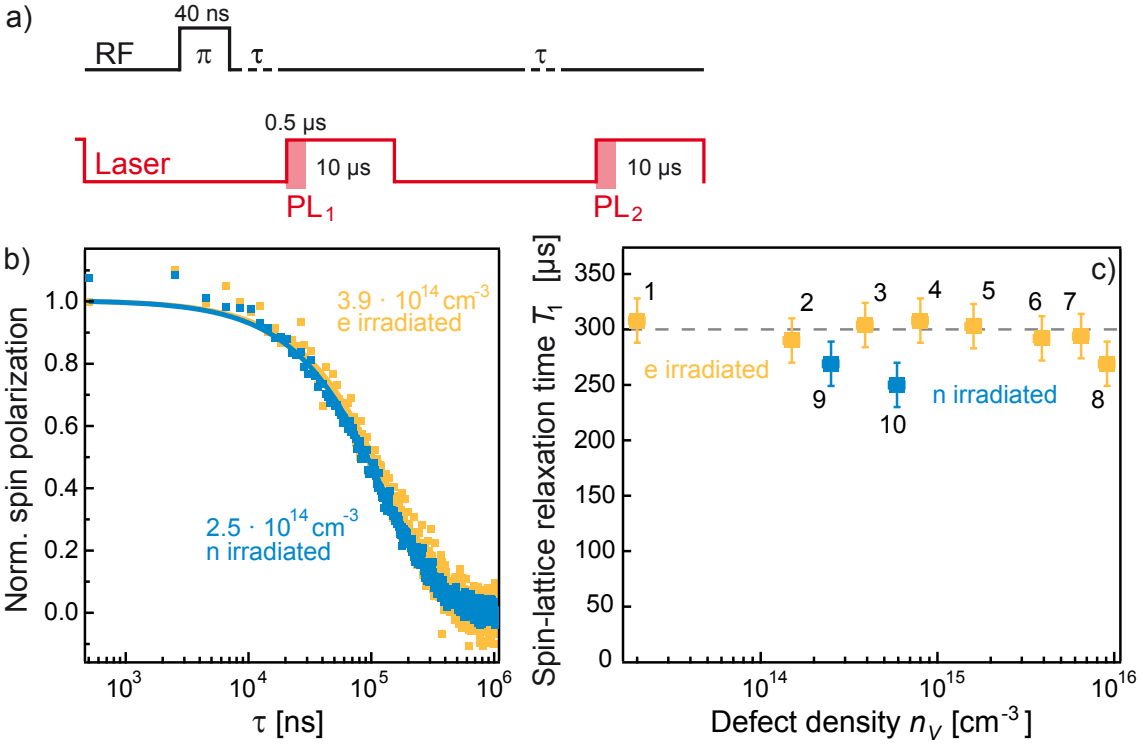

Figure 5.5.: a) Pulse sequence applied to measure the spin-lattice relaxation time T_1. The time gap τ between the first RF-pulse and the subsequent read-out laser pulse is varied. In the reference part without RF-pulses, the dark time is varied. b) Exemplary curves of resulting spin polarization in dependence on τ. The solid lines are fits to Equation 5.3. The curves are normalized to the maximum of each fit. c) Extracted T_1 values for all samples, denoted according to Table 5.2. The gray dashed line at 300 µs is a guide to the eye.

The extracted T_1 times are around 300 µs for most of the samples irradiated with electrons. Only for the sample with the highest irradiation fluence of $5 \cdot 10^{18}\,\mathrm{cm}^{-3}$ (sample #8) the relaxation time is shorter, indicating increased crystal damage.

For both neutron irradiated samples (#9, 10) the T_1 times are distinctly shorter, although the calculated defect concentration is in the range of moderately irradiated electron samples. This is a strong hint that neutrons produce significantly more non-luminescent paramagnetic defects as well as cause stronger crystal damage. Last but not least, from comparison of the 1 MeV and 2 MeV electron irradiated samples (#2, 3), no apparent change of the T_1 time with the electron energy is observed.

Next, the dependence of the spin-spin relaxation time T_2 on the irradiation method is evaluated. The measurements are conducted at room temperature, one time with $B_z = 0\,\mathrm{mT}$ and at 15 mT on the ν_2 resonance.

Again, following the Spin-Echo technique introduced in Chapter 5.1, the pulse sequence in Figure 5.6a is applied to all the samples. In Figure 5.6b three exemplary curves are presented. From the fits to Equation 5.5, the T_2 values are extracted and presented as a function of the defect density in Figure 5.6c.

While the spin-lattice relaxation times T_1 of the electron irradiated series generally showed no dependence on the defect density, the spin-spin coherence time T_2 for $B_z = 15\,\mathrm{mT}$ continuously decreases in samples with densities $n_V > 3.9\cdot10^{14}\,\mathrm{cm}^{-3}$ (sample #3). Theoretically, an approximately linear decrease in spin coherence with the concentration of paramagnetic centers is expected [121], leading to the fitting function:

$$T_2(n_V) = \frac{T_2^0}{1 + n_V/n_0}, \tag{5.6}$$

with T_2^0 and n_0 being free parameters.

The best fit is denoted by the solid line in Figure 5.6c. For low irradiation fluences, leading to vacancy densities $n_V << n_0 = 2.6\cdot10^{15}\,\mathrm{cm}^{-3}$, the effect of irradiation-induced defects on decoherence is negligible and the spin coherence time stays as in the pristine sample at $T_2^0 = 48\,\mu\mathrm{s}$ (samples #1, 2, 3). Contrary, for high irradiation fluences and subsequently $n_V > n_0$, the decoherence is dominated by all types of irradiation-induced defects. The highest irradiated sample (#8) deviates from the dependence of Equation 5.6, indicating, as with the T_1 time in Figure 5.5c, a strong crystal damage induced by high-energy electrons. Similarly to the T_1 values, no change in T_2 due to different electron energies is observed, comparing the 1 MeV and 2 MeV irradiated samples (#2 and 3).

In zero magnetic field, a qualitatively same evolution is observed, while the short relaxation time makes a quantitative analysis impossible.

In comparison, the two neutron irradiated samples (# 9 and 10) show substantially shorter coherence times as the electron irradiated ones with similar defect densities.

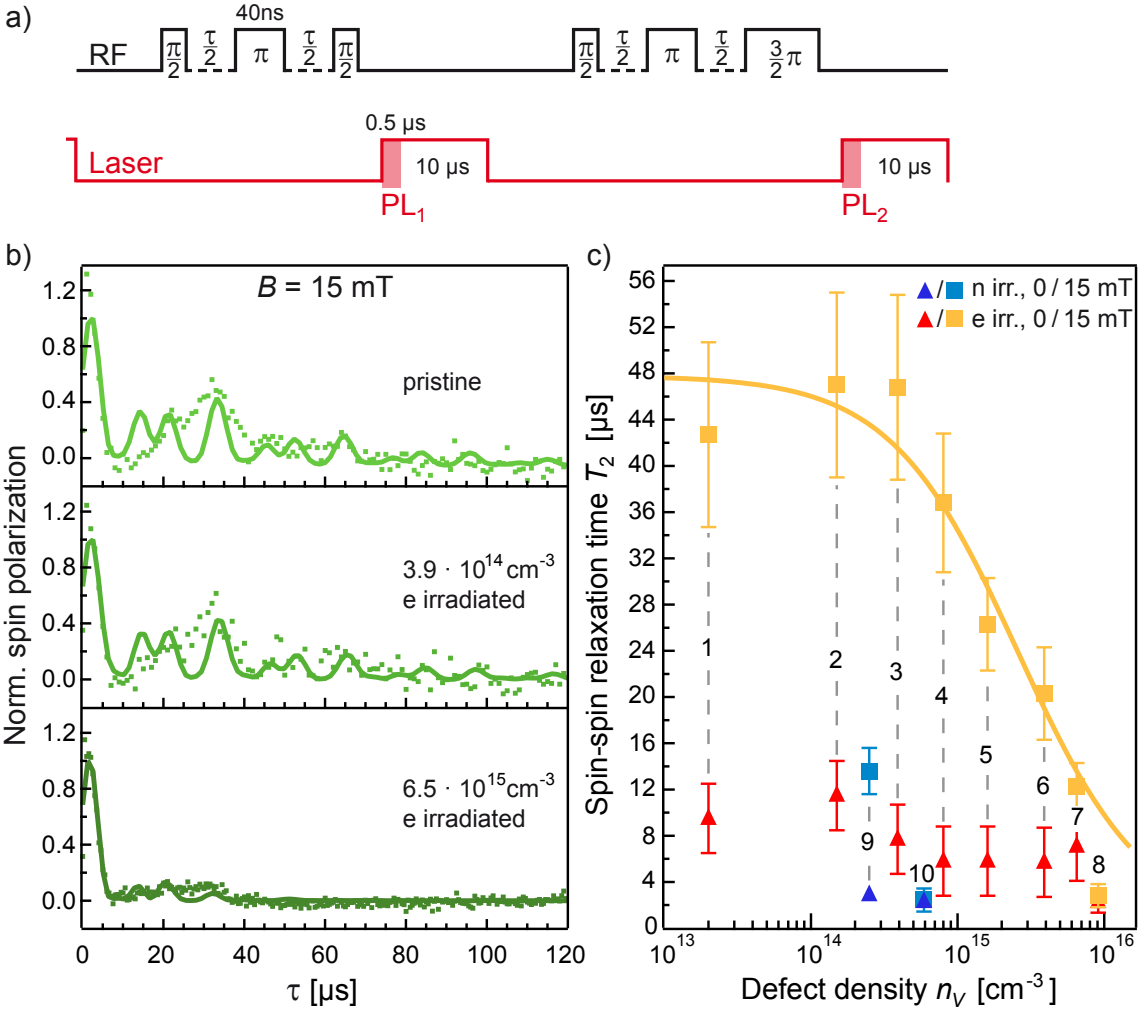

Figure 5.6.: a) Pulse sequence to measure the spin-spin relaxation time T_2. The time gap $\tau/2$ between the RF-pulses is altered. b) Spin polarization in dependence on delay time τ in electron irradiated samples. The solid lines are fits to Equation 5.5. The curves are normalized. c) Extracted T_2 values for all samples, enumerated according to Table 5.2. The values for electron irradiated samples are fitted according to Equation 5.6 (solid line).

This indicates that neutrons create a wide range of non-luminescent impurities, other than silicon vacancies, inducing stronger dipolar coupling and subsequently diminishing the T_2 time of the nearby V_{Si} defects.

All in all, the analysis of the dependence of both the T_1 and T_2 relaxation times on the irradiation fluence and the kind of ionizing radiation revealed following.

For electron irradiated samples, T_1 time is almost constant around 300 µs, while the T_2 time linearly decreases for defect concentrations higher than $\sim 4 \cdot 10^{14}\,\mathrm{cm}^{-3}$.

The highest irradiated sample shows a deviation to lower values for both T_1 and T_2, indicating an increased crystal damage. No influence of the electron energy is observed.

The neutron irradiated samples show a significantly shorter T_1 and T_2 values as the electron irradiated samples with a similar defect density, indicating that the bigger in cross-section neutrons produce more damage to the crystal and introduce far more non-luminescent paramagnetic defects along with the V_{Si} centers in the irradiation area.
In regard to sensing implementations, to obtain the best signal-to-noise ratio by maximizing the ensemble of excited defects, without loss in coherence time, and subsequently in sensitivity, sample #3 seems to be most suitable. Generally speaking, electron irradiation seems to be superior to the neutron irradiation, and a defect density below $n_0 = 2.6 \cdot 10^{15}\,\mathrm{cm}^{-3}$ gives the optimal ratio of coherence time and signal intensity. All other experiments on coherence properties in previous and next chapters are conducted on sample #3, meaning that the dipolar coupling between irradiation-induced vacancies can be neglected and all the here obtained results on ensembles can be projected into single V_{Si} spins.
After discussing the impact of the magnetic field, temperature and defect density on the coherence properties of the V_{Si} defect, a technique allowing substantial prolongation of the spin-spin coherence time by using dynamic decoupling sequences will be introduced in the next chapter.

5.3. Extending the Coherence Time With Dynamic Decoupling Pulse Sequences

The prolongation of the T_2 coherence time is a major topic in the quantum sensing community. As elaborated in Chapter 5.1, one of the main limiting factors of the T_2 time is the interaction with the nuclear spins of the naturally abundant ^{29}Si and ^{13}C and other impurities. In order to diminish this interaction, so-called dynamical decoupling (DD) sequences are utilized. The most known one is Carr-Purcell-Meiboom-Gill (CPMG) [122], which utilizes spin rotation along both x- and y-axis and has shown considerable coherence prolongation for the NV-centers in diamond [4, 123].
Although being widely used in NMR [124], MRI [125] and also on various quantum systems [126, 127], the origin of the anomalous prolongation of the coherence time via CPMG protocol is under ongoing debate. One interpretation is that it may arise from the spin storage along the quantization axis (S_z) during RF-pulses, meaning that the decay is captured by spin-lattice relaxation rather than quantum-state decoherence [128]. Another alternative is that a finite rephasing pulse length may result in a long tail in the CPMG curve for short delays between RF-pulses due to dipolar coupling [129]. Nevertheless, theoretical considerations show that the application of the CPMG pulse sequence is equivalent to spin-locking [130, 131], i.e. the preservation of the spin state perpendicular to the magnetic field axis. Furthermore, pulse errors may quickly destroy some spin states, but maintain other states with high fidelity over longer times [132].
The CPMG pulse sequence is depicted in Figure 5.7a. At the first sight, this sequence is very similar to the Spin-Echo experiment but with two major differences.
On the one hand, the rephasing π pulse is applied with 90° phase difference in regard to the $\pi/2$ pulses. Hence, after the dephasing time $\tau/2$, the π_{90} pulse is not rotating the main spin vector, but only the so far dephased parts back into rephasing, which makes this scheme robust against pulse uncertainties [133]. Furthermore, the $\tau/2 - \pi_{90} - \tau/2$ part is repeated several times N, making the spins rephase over and over again and preserve in the ideal case the spin polarization over a long time. If the time intervals $\tau/2$ are chosen short enough, i.e. much shorter than the Larmor precession of the nuclear spins, their field can be regarded as static and, for short τ and many repetitions N, ESEEM is completely suppressed [134].
This sequence is applied on the same sample that was already characterized in Chapter 5.1 and is denoted as #3 in Table 5.2.

The measurements resonant to the ν_2 transition at room temperature and in a magnetic field along the c-axis $B_z = 15\,\mathrm{mT}$ are depicted in Figure 5.7b, as spin polarization $\mathcal{S}$ versus the free precession time $N\tau$. From the left part of Figure 5.7b it is evident that with increasing number N of π_{90} pulses, the ESEEM modulation depth decreases and the non-oscillating contribution in spin polarization is dominating. In the right part it is visible, that for $N > 15$, the ESEEM pattern is completely absent, indicating a complete decoupling from the ^{29}Si and ^{13}C nuclear spin baths. Intuitively, for $N = 0$ (one π_{90} pulse) the sequence becomes equal to the Spin-Echo technique and hence the same coherence time, as well as the same ESEEM pattern as in the Spin-Echo experiments can be expected.

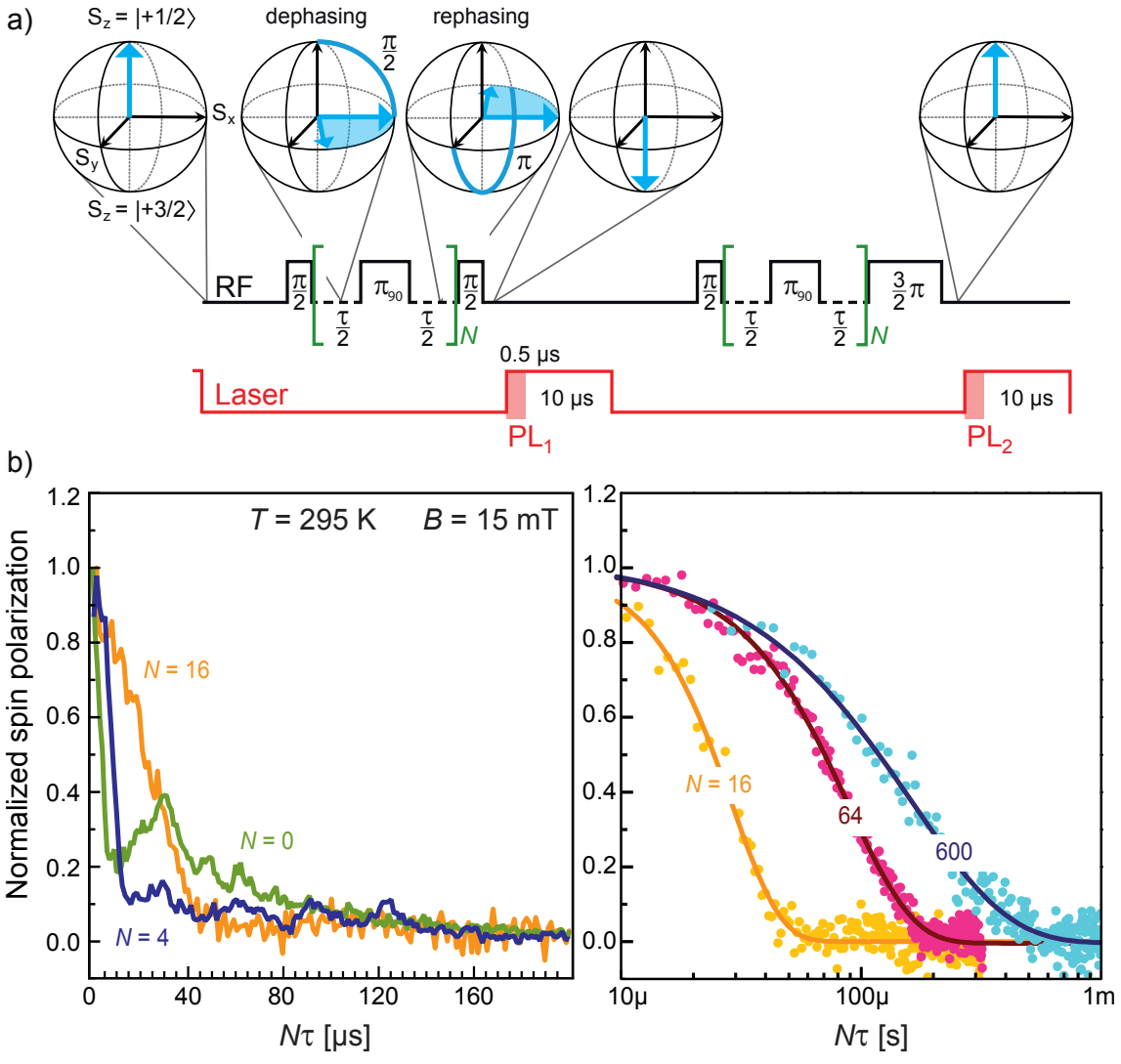

Figure 5.7.: a)Pulse sequence in order to measure the CPMG T_2 time. b) Normalized spin polarization as a function of free evolution time $N\tau$, measured at room temperature and $B_z = 15\,\mathrm{mT}$ for different numbers of rephasing π_{90} pulses N. The data on the left is fitted according to the Equation 5.7

Indeed, the comparison of the $N = 0$ data in Figure 5.7 and the Spin-Echo measurement under the same conditions in Figure 5.3b for the ν_2 line, clearly shows coinciding evolutions with the same decay time.
To extract the coherence time T_2, the spin polarization is fitted with a stretched exponent of the form [135]:

$$\mathcal{S} = (2\mathcal{F}_\mathcal{S} - 1)\mathrm{Exp}\left[\left(-\frac{N\tau}{T_2}\right)^n\right], \tag{5.7}$$

with $\mathcal{F}_\mathcal{S}$ denoting the state preservation fidelity and n fixed in the range between 1 and 3 [135]. While the role of these free parameters will be discussed later on, the determined T_2 values are presented in Figure 5.8b as a function of the number of pulses N.
Hence, the T_2 time is steadily increasing, ultimately exceeding the T_2 time obtained from the Spin-Echo measurements, denoted by the brown dashed line, and saturates at around 200 µs for $N > 100$. One might expect the CPMG coherence time values to start at the T_2 time extracted from the Spin-Echo measurements. However, the here obtained data is fitted to Equation 5.7, which is only taking into account the non-oscillating contributions to the curve shape and ignores the still pronounced ESEEM pattern for $N < 15$. Consequently, as long as the ESEEM is prevailing, this leads to a shorter extracted coherence times compared to Spin-Echo experiments.
The T_2 values are fitted to a power law of the form (solid brown line in Figure 5.8c) [135]:

$$\frac{1}{T_2(N)} = \frac{1}{T_2(0)N^\kappa} + \frac{1}{\eta T_1}. \tag{5.8}$$

The scaling factor $\kappa = 0.83 \pm 0.05$ slightly deviates from the expected general scaling $\kappa = 2/3$ [123] for a Lorentzian noise spectrum of an electronic spin-bath and depends on other possible decoherence mechanisms arising from the spin-bath dynamics [135].
From the fit, the longest spin locking time of $T_2(N >> 100) = (230 \pm 30)$ µs is obtained. As described by [134], the T_2 time is ultimately limited by the spin-lattice relaxation time T_1, as $1 < \eta = T_2/T_1 < 2$. In the ideal two level system, $\eta = 2$ is expected, while our measurements deliver $\eta = 0.67$, which is ascribed to phonon-induced decoherence by [4], who also obtains a similar η value for the NV-center in diamond.
As analyzed in Chapter 5.1, the T_1 time is considerably prolonged at $T = 17$ K to over 10 s, suggesting also a possible further extension of the T_2 time using the CPMG sequence. The low temperature measurements are depicted in Figure 5.8a.

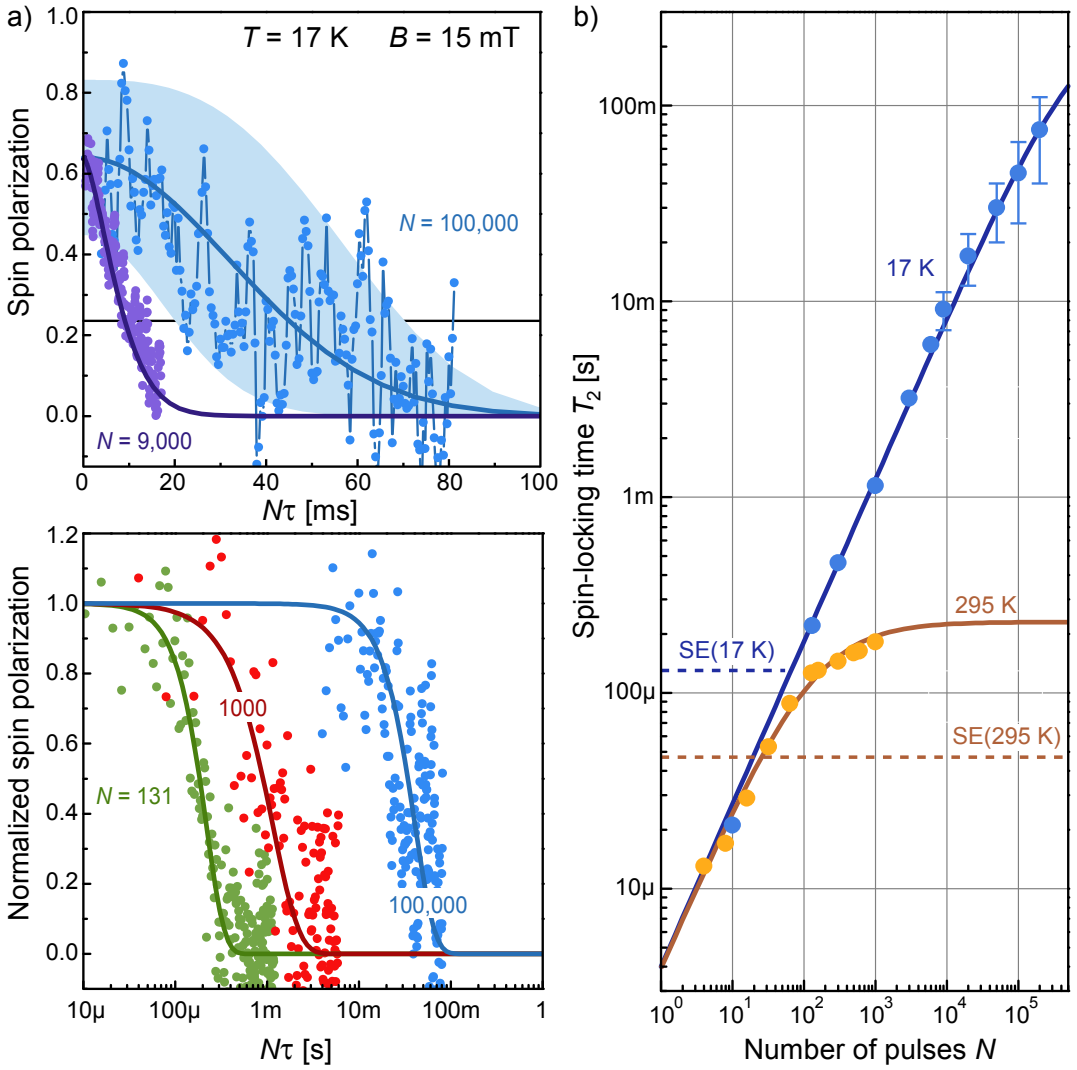

Figure 5.8.: a) Spin polarization as a function of free evolution time $N\tau$, measured at T = 17 K and B_z = 15 mT for different numbers of rephasing π_{90} pulses N. The data is fitted according to Equation 5.7. The light-blue area represents a range of the best fits within the standard deviation. b) Extracted T_2 values at room temperature and T = 17 K (B_z = 15 mT) in dependence on the number of rephasing pulses N. The solid lines are fits to Equation 5.8. Dashed lines represent the T_2 values obtained by the Spin-Echo technique in Chapter 5.1.

Indeed, even for N exceeding 100,000 π_{90} pulses, no saturation in coherence time is observed. The data is again fitted according to Equation 5.7 and the extracted T_2 values added to Figure 5.8b. For the highest measured pulse number $N = 200,000$ a coherence time $T_2 = (75 \pm 35)$ ms is obtained, exceeding the Spin-Echo $T_2 = (134 \pm 20)$ µs (blue dashed line) by almost three orders of magnitude. Furthermore, this coherence time establishes a 75-fold improvement in comparison to the earlier reported results on the single defects in high-purity 4H-SiC [16], while the here presented results are obtained from an industrially available SiC wafer without further purification treatment or annealing.

The relatively large errors for large N arise from a consequently necessary increase in integration time with increasing T_2, e.g. the $N = 100,000$ measurement was running for over five days straight.
In our experiments, the spectral position of laser excitation is at the maximum of the phononic sideband. By resonant optical excitation as described in [20], substantially higher ODMR contrast can be achieved [14], and the observation of spin locking for $N > 200,000$ rephasing pulses should be feasible.
From the fit of the low temperature T_2 values to Equation 5.8 with the same $T_2(0)$ and κ as at room temperature, a saturation level of $T_2 \rightarrow 0.3\,\mathrm{s}$ for $N > 10^7$ can be estimated.
Now, the fitting parameters from Equation 5.7, namely the exponent n and the state preservation fidelity $\mathcal{F}_S$, shall be analyzed. The latter is calculated as the ratio between the signal maximum of each CPMG measurement and the Rabi amplitude. The resulting n and $\mathcal{F}_S$ are depicted as a function of the number of pulses N in Figure 5.9.

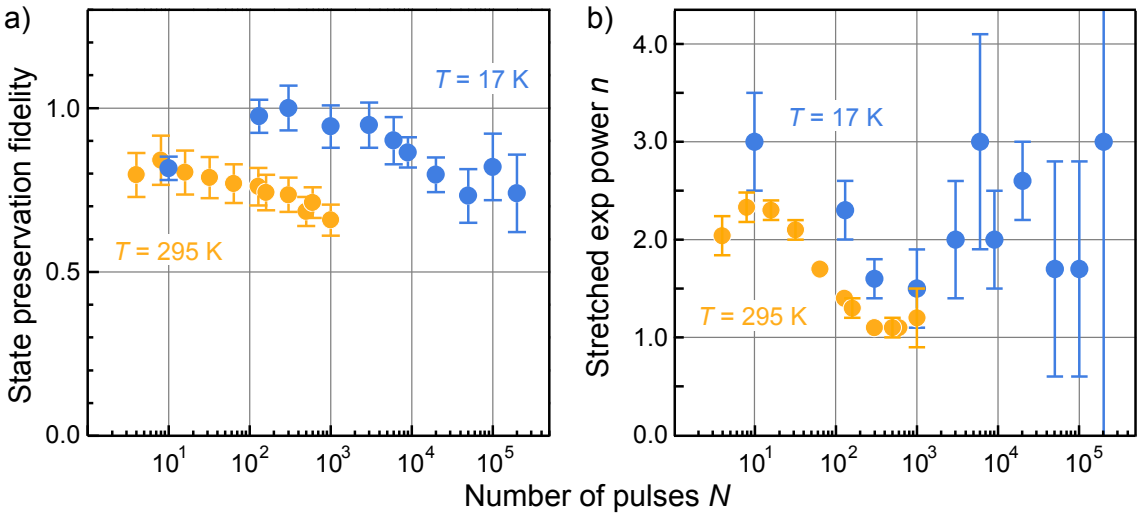

Figure 5.9.: State preservation fidelity $\mathcal{F}_S$ (a) and exponent n (b) as a function of the number of pulses N.

The preserved state fidelity, normalized to the maximum amplitude of the signal for $N = 0$, reflects how the polarization amplitude is influenced by the increasing number of repeating RF-pulses. From Figure 5.9, it is evident that for all conducted measurements, the fidelity stays over 0.6, indicating the spin-locking along the S_x-axis of the Bloch-Sphere in Figure 5.7a.
The power parameter n is influenced by the dynamics of the spin environment and inhomogeneous broadening due to ensemble averaging [135]. For a Lorentzian bath, n is expected to be in the range $1 \leq n \leq 3$, with $n = 3$ in the short time limit $N\tau < T_2$ and $n = 1$ in the long time limit $N\tau > T_2$.

While for the room temperature measurements, the n values show the expected evolution with N, no quantitative statement for the $T = 17\,\mathrm{K}$ measurements can be done due to significantly increased error bars. Nevertheless, also for $T = 17\,\mathrm{K}$, the extracted n stay within the expected boundaries.

It must be noted that the CPMG pulse sequence establishes dynamic decoupling only along one axis, i.e. only the spin component $S_x = (|+1/2\rangle + |+3/2\rangle)/\sqrt{2}$ is preserved, while test measurements on the perpendicular component $S_y = (|+1/2\rangle + i\,|+3/2\rangle)/\sqrt{2}$ show a much faster decay. Nevertheless, the here obtained CPMG locking time of S_x serves as an near-ideal limit for T_2 of all spin components, as elaborated in [4, 133, 134]. In order to achieve quantum information processing, arbitrary initial and final spin states must be preserved. For this task, two-axis sequences like the XY-family, which preserve all spin components equally [123, 133], are utilized. However, these sequences are very sensitive to angle errors due to imperfect pulse lengths [133, 136], which is a limitation of our measurement setup at the moment. Alternatively, composite pulse sequences [137], like the Knill dynamic decoupling (KDD) protocol, which preserve arbitrary quantum states, while keeping robustness against pulse errors can be applied. Measurements utilizing these sequences is a task for the future work.

While the so far discussed results favor the theoretical prediction of spin-locking, in order to verify this statement, quantum state tomography (QST) is conducted. By QST, the resulting density matrix, i.e. after modification by CPMG, is established, which describes the partial polarization of the system along the possible spin states. Therefore, if the CPMG sequence is actually locking the spin state along the S_x direction a spin polarization must occur in the respective components of the density matrix [138, 139].

At first, a closer look on the CPMG pulse sequence in Figure 5.7a must be taken, particularly considering the ν_2 transition. By the laser pulse, the spins are aligned in the $|+1/2\rangle$ state, which is defined as the $S = [S_x, S_y, S_z] = [0,0,1]$ spin state in the Bloch-Sphere of Figure 5.7a. The following RF-pulse ($\pi/2$) initializes the spin either into the $(|+1/2\rangle + |+3/2\rangle)/\sqrt{2}$ ($S = [1,0,0]$) or the $(|+1/2\rangle + i\,|+3/2\rangle)/\sqrt{2}$ ($S = [0,1,0]$), depending on the relative phase to the following pulse. This part will be referred to as RF_{ini}. Next, the $[\tau/2 - \pi_{90} - \tau/2]^N$ section manipulates the spin in a yet unknown way, which is to be revealed in the following and is referred to as RF_{man}. Finally the third RF-pulse ($\pi/2$ or $3\pi/2$) projects the spin vector into the eigenstates $|+1/2\rangle$ or $|+3/2\rangle$ and is denoted as $RF_{proj,1}$. By the subsequent laser pulse, PL_1 is measured. In the reference half, the RF_{ini} and RF_{man} parts are identical to the previous ones, while the projection pulse $RF_{proj,2}$ is always shifted by a length of a π pulse in comparison to $RF_{proj,1}$, to ensure maximal contrast. Subsequently, PL_2 is detected and the spin polarization $P = [P_x, P_y, P_z]$ is determined from $PL_1 - PL_2$.

Now, in order to obtain the individual polarization components P_x, P_y, P_z and the resulting density matrix after a manipulation by RF_{man}, measurements with different $RF_{proj,1}$ and $RF_{proj,2}$ must be conducted, in order to project the desired polarization component onto one of the eigenstates. Hence, to read out the $|+1/2\rangle$ (P_z) polarization, no RF-pulse ($RF_{proj,2} = \pi_0$) is applied. To obtain $(|+1/2\rangle + |+3/2\rangle)/\sqrt{2}$ (P_x) and $(|+1/2\rangle + i\,|+3/2\rangle)/\sqrt{2}$ (P_y) components a $RF_{proj,1} = \pi_0/2$ ($RF_{proj,2} = 3\pi_0/2$) and $RF_{proj,1} = \pi_{90}/2$ ($RF_{proj,2} = 3\pi_{90}/2$) pulses are applied, respectively.
Finally, the resulting density matrix ρ_{out} is determined as [138]:

$$\rho_{out} = \frac{\sigma_0 + P_x\sigma_x + P_y\sigma_y + P_z\sigma_z}{2}, \tag{5.9}$$

with σ denoting the Pauli matrices:

$$\sigma_0 = \begin{vmatrix} 1 & 0 \\ 0 & 1 \end{vmatrix},\ \sigma_x = \begin{vmatrix} 0 & 1 \\ 1 & 0 \end{vmatrix},\ \sigma_y = \begin{vmatrix} 0 & -i \\ i & 0 \end{vmatrix},\ \sigma_z = \begin{vmatrix} 1 & 0 \\ 0 & -1 \end{vmatrix}. \tag{5.10}$$

The described measurements are conducted at $T = 17\,\mathrm{K}$ and $B_z = 15\,\mathrm{mT}$ for $N = 20{,}000$ and $\tau/2 = 20\,\mathrm{ns}$, i.e. a free evolution time $N\tau = 0.8\,\mathrm{ms}$, on the ν_2 resonance.
The resulting density matrix, separated by the real and imaginary part, is depicted in Figure 5.10. From the diagonal components $|+1/2,+1/2\rangle$ and $|+3/2,+3/2\rangle$ being 0.5, it is evident that there is no polarization along the S_z-direction. Also, since the imaginary part $Im(\rho)$ is nearly zero, the polarization is determined to be along the S_x-axis. From the already discussed initial amplitude of the CPMG curves in Figure 5.9a, a state preservation fidelity $\mathcal{F}_S$ higher than 0.6 for all the pulse numbers N is obtained. Therefore, by performing QST, a locking of the spin polarization along the S_x component in our experiments is unambiguously shown.

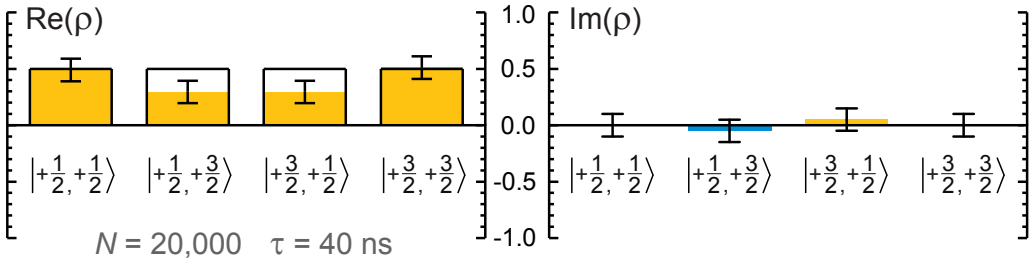

Figure 5.10.: Real and imaginary part of the resulting density matrix ρ_{out} from the quantum state tomography at $T = 17\,\mathrm{K}$ and $B_z = 15\,\mathrm{mT}$, for $N = 20{,}000$ and $\tau = 40\,\mathrm{ns}$, calculated by Equation 5.9. Colored squares denote the measured values and the empty bars the theoretical expectation for an ideal polarization along S_x.

As mentioned above, for quantum information processing, arbitrary initial and final spin states must be preserved. Nevertheless, the here shown extensively prolonged spin-locking coherence is of a key role to improve the sensitivity of quantum magnetometry and thermometry, as introduced in Chapter 4. Also, the V_{Si} defects can now be implemented in quantum sensors based on multipulse spin-locking protocols with extraordinarily sensitivity [123, 134, 140, 141], like the quantum lock-in detection [142] with extremely narrow bandwidth, as required for nuclear magnetic resonance spectroscopy at the nanoscale [143, 144].
Compared to the benchmark value of the spin-locking time in the NV-center in diamond of around 600 ms [4], the obtained value of 75 ms in this thesis is not far away, especially considering that the NV-center coherence time is obtained from a ^{12}C enriched crystal, while our measurements are conducted on a standard industrially available SiC wafer without any isotope purification processes. This once again demonstrates the high potential of the V_{Si} defect in SiC for various quantum applications.

6. Summary

In the present work, the energetic structure and coherence properties of the silicon vacancy point defect in the technologically important material silicon carbide are extensively studied by the optically detected magnetic resonance (ODMR) technique in order to verify its high potential for various quantum applications. In the V_{Si} defect, unique attributes are arising from the C_{3v} symmetry and the spin-3/2 state, which are not fully described by the standard Hamiltonian of the uniaxial model. Therefore, an advanced Hamiltonian, describing well the appearing phenomena is established and the relevant parameters are experimentally determined. Utilizing this new accomplishments, several quantum metrology techniques are proposed.

First, a vector magnetometry scheme, utilizing the appearance of four ODMR lines, allows for simultaneous detection of the magnetic field strength and the tilting angle of the magnetic field from the symmetry axis (c-axis) of the crystal. By measurements in differently aligned magnetic fields, sensitivities of $10\,\mu T/\sqrt{Hz}$ and up to $0.5°/\sqrt{Hz}$, are experimentally obtained. By down-scaling to single defects, this vector magnetometry technique may also provide substantial spatial resolution, as was shown on the NV-centers in diamond [43].

The second magnetometry protocol utilizes the appearance of energetic level anti-crossings (LAC) in the ground state (GS) energy levels. By monitoring the change in photoluminescence in the vicinity of this GSLACs, sensitivities for the magnetic field strength of $87\,nT/\sqrt{Hz}$, with an estimated sensitivity of $100\,fT\sqrt{Hz}$ with further improvement in sample treatment and read-out protocols, are obtained. This all-optical method does not require any radio waves and hence provides a much easier operation with less error sources as for the common magnetometry schemes utilizing quantum points. Also, the analyzed GSLAC appears only for systems with a spin state of 3/2 or higher, and, as revealed in the theoretical calculations for the C_{3v} symmetry, is narrower as the GSLAC of the spin 1-systems. This makes the proposed all-optical magnetometry with the V_{Si} defect in SiC potentially more sensitive to the magnetic field strength and more robust against field misalignment than the spin-1-systems.

A similar all-optical method is applied for temperature sensing, utilizing the thermal shift of the zero field splitting (ZFS) and consequently the anticrossing in the excited state (ES).

Again, by monitoring the change in photoluminescence with temperature, a sensitivity of 100 mK/$\sqrt{\text{Hz}}$, with an estimated limit of 1 mK/$\sqrt{\text{Hz}}$ by further improvements is achieved. The quantitative temperature dependence of the ESLACs is additionally determined from ODMR measurements, where the spectral position of the ESLACs can be read out from the contrast change of the low frequency ODMR transition.
Since the GSLACs show no dependence on temperature, the all-optical magnetometry and thermometry (utilizing the ESLACs) can be conducted subsequently on the same defect.
In order to quantify the achievable sensitivity of quantum metrology, as well as to prove the potential of the V_{Si} defect in SiC for quantum processing, the coherence properties are investigated by the pulsed ODMR technique. First, by conducting Rabi experiments, a coherent control of the defect spins is verified. Subsequently, the spin-lattice relaxation time T_1 and the spin-spin relaxation time T_2 are thoroughly analyzed for their dependence on the external magnetic field along the c-axis and temperature.
Regarding magnetic field dependence, T_1 time stays constant at (340 ± 30) µs for fields up to 31 mT, while T_2 increases from (8 ± 2) µs at zero field to a saturation level of (47 ± 8) µs for $B_z > 11$ mT at room temperature. On the other hand, T_1 continuously increases for decreasing temperature, with the room temperature value of (340 ± 30) µs increasing to at least 10 s for cryogenic temperatures. The T_2 time shows a non-monotonic temperature dependence, while the saturation level is increased to (134 ± 20) µs at 17 K.
For actual sensing implementations it is crucial to obtain the best signal-to-noise ratio without loss in coherence time. Therefore, the irradiation process, by which the defects are created in the crystal, plays a decisive role in the device performance. In the present work, samples irradiated with electrons or neutrons with different fluences and energies, producing different defect densities, are analyzed in regard to their T_1 and T_2 times at room temperature and at a magnetic field of 15 mT along the c-axis.
For the electron irradiated samples, T_1 time slightly varies around 300 µs, while the T_2 time linearly decreases for defect concentrations higher than $\sim 4 \cdot 10^{14}$ cm^{-3}. The highest irradiated sample shows lower values for both T_1 and T_2, indicating possible crystal damage. No direct influence of the electron energy was observed, apart from the expected different defect densities.
For the neutron irradiated samples, a significantly shorter T_1 and T_2 values as in the electron irradiated samples with a similar defect density are obtained. This indicates that the bigger in cross-section neutrons produce more damage to the crystal and introduce far more non-luminescent paramagnetic defects along with the V_{Si} centers in the irradiation area.

Generally speaking, an electron irradiation seems to be superior to the neutron irradiation, and a defect density below $2.6 \cdot 10^{15}\,\mathrm{cm}^{-3}$ gives the optimal ratio of coherence time and signal intensity.
Last but not least, a scheme to substantially prolong the T_2 coherence time by locking the spin polarization with the dynamic decoupling Carr-Purcell-Meiboom-Gill (CPMG) pulse sequence is applied. This sequence diminishes the influence of the surrounding ^{29}Si and ^{13}C nuclear spins and other impurities on the V_{Si} electron spins. While the CPMG sequence preserves only one spin component, the obtained coherence time serves as a near-ideal limit for preservation of arbitrary quantum states [133]. This way, the T_2 coherence time for one spin component is prolonged up to $(230 \pm 30)\,\mu$s at room temperature and a magnetic field of 15 mT. At 17 K, the sequence delivers an experimentally obtained spin-locking time of (75 ± 35) ms, with an estimated achievable coherence of ~ 300 ms.
While coming close to the benchmark values obtained for the NV-center in high-purity, ^{12}C enriched diamond crystal, all the experiments and obtained results in this thesis are performed on industrially available SiC wafers without any isotope purification or annealing.
All in all, by introducing several quantum metrology techniques, revealing the true energetic structure owing to the C_{3v} symmetry, determining the coherence properties in dependence on the ambient conditions as well as on the irradiation process and finally by expanding the coherence time to at least 75 milliseconds, the high potential of the V_{Si} defect in SiC in the field of various quantum applications is unambiguously justified.

Zusammenfassung

In der vorliegenden Arbeit werden die energetische Struktur und die Kohärenzeigenschaften der Silizium Fehlstelle V_{Si} in dem technologisch relevanten Material Siliciumcarbid mit Hilfe der optisch detektierten Magnetresonanz (ODMR) Technik extensiv analysiert, um ihr außerordentliches Potential für verschiedene quanten-mechanische Anwendungen zu untermauern. Aus der C_{3v} Symmetrie und dem 3/2 Spinsystem des V_{Si} Defekts entstehen einzigartige Attribute, die nur teilweise durch den Standard Hamiltonoperator des Modells einer einachsigen Symmetrie wahrheitsgemäß beschrieben werden. Aus diesem Grund wird ein weiterentwickelter Hamiltonoperator aufgestellt, welcher die auftretenden Eigenschaften genau wiedergibt. Aus experimentellen Messungen werden anschließend seine Parameter bestimmt. Das nun vorliegende genaue Verständnis der auftretenden Phänomene wird dazu genutzt, diverse Methoden zur Quantensensorik auszuarbeiten.
Zuerst wird ein Schema für Vektormagnetometrie aufgestellt, welches sich das Auftreten von vier ODMR Linien zunutze macht. Die Methode ermöglicht simultane Detektion, sowohl von der Magnetfeldstärke, als auch von dem Winkel zwischen der Magnetfeldrichtung und der Symmetrieachse (c-Achse) des Kristalls. Aus den Messungen in verschieden ausgerichteten Magnetfeldern werden Sensitivitäten von $10\,\mu T/\sqrt{Hz}$ und bis zu $0.5°/\sqrt{Hz}$ erreicht. Durch down-scaling zu einzelnen Defekten, könnte die vorgestellte Methode auch beachtliche räumliche Auflösung bieten, wie schon für die NV-Zentren in Diamant gezeigt wurde [43].
Das zweite Magnetometrieprotokoll nutzt das Auftreten von energetischen anticrossings (level anticrossing, LAC) im Grundzustand (ground state, GS). Durch das Verfolgen der Änderung der Photolumineszenz in der Nähe dieser GSLACs, ist eine Auflösung der Magnetfeldstärke von $87\,nT/\sqrt{Hz}$ erreicht, mit einer abgeschätzten möglichen Auflösung von $100\,fT\sqrt{Hz}$ für weitere Verbesserung der Probenherstellung und der read-out Protokolle. Diese rein optische Technik braucht keine Radiowellen und ist dementsprechend viel leichter umzusetzen und bietet weniger Fehlerquellen als die üblichen Magnetometriemethoden an Quantenpunkten. Darüber hinaus tritt der analysierte GSLAC-2 nur in Systemen mit Spin 3/2 oder höher auf und ist schmaler als das GSLAC des Spin-1-Systems, wie in den theoretischen Berechnungen für die C_{3v} Symmetrie aufgezeigt wird.

Somit ist die vorgestellte rein optische Magnetometrie mit den V_{Si} Defekten in SiC potenziell sensitiver gegenüber der Magnetfeldstärke und robuster gegenüber fehlerhafter Feldausrichtung, als mit Spin-1-Systemen.
Eine ähnliche, rein optische Methode wird auch für Temperaturmessungen vorgestellt, welche auf der thermisch induzierten Verschiebung der Nullfeldaufspaltung (zero field splitting, ZFS) und somit auch der anticrossings im angeregten Zustand (excited state, ES) basiert. Wie zuvor, durch die Betrachtung der Photolumineszenzänderung mit der Temperatur, kann eine Sensitivität von $100\,\mathrm{mK}/\sqrt{\mathrm{Hz}}$, mit einem abgeschätzten Limit von $1\,\mathrm{mK}/\sqrt{\mathrm{Hz}}$ durch weitere Optimierungen erreicht werden. Die quantitative Temperaturabhängigkeit der ESLAC Position wird zusätzlich durch ODMR Messungen bestimmt, in denen die spektrale Position der ESLACs aus der Änderung des Kontrastes extrahiert werden kann. Da die GSLACS keine Temperaturabhängigkeit zeigen, können die rein optischen Methoden zur Magnetfeld- und Temperaturmessung nacheinander am selben Defekt erfolgen.
Um die erreichbare Sensitivität der Quantenmetrologie zu quantifizieren und auch um das Potential der V_{Si} Defekte für Quantencomputing zu demonstrieren, werden die Kohärenzeigenschaften mit Hilfe der gepulsten ODMR Technik analysiert. Zuerst wird durch die Rabi Experimente eine fortlaufende Kontrolle der Defektspins gezeigt. Danach werden die Spin-Gitter Relaxationszeit T_1 und die Spin-Spin Relaxationszeit T_2 eingehend analysiert und deren Abhängigkeit von einem externen Magnetfeld entlang der c-Achse und der Temperatur aufgestellt.
Bei Raumtemperaturmessungen in Magnetfeldern mit einer Stärke von bis zu 31 mT bleibt T_1 konstant bei $(340 \pm 30)\,\mu\mathrm{s}$, während T_2 von $(8 \pm 2)\,\mu\mathrm{s}$ in Nullfeld auf ein Saturierungsniveau von $(47 \pm 8)\,\mu\mathrm{s}$ für $B_z > 11\,\mathrm{mT}$ ansteigt.
Bei Erniedrigung der Temperatur ist eine kontinuierliche Erhöhung der T_1 Zeit zu beobachten, von $(340 \pm 30)\,\mu\mathrm{s}$ bei Raumtemperatur auf mindestens 10 s für kryogenische Temperaturen. Die T_2 Zeit zeigt kein eindeutiges Temperaturverhalten, wobei das Saturierungslevel sich auf $(134 \pm 20)\,\mu\mathrm{s}$ bei 17 K erhöht.
Für tatsächliche Implemetierung in einem Sensor, ist es entscheidend ein Optimum zwischen dem Signal-Rausch-Verhältnis und der Kohärenzlänge zu etablieren. Deswegen spielt die Kristallbestrahlung, durch die V_{Si} Defekte erzeugt werden, eine wichtige Rolle für die Leistungsfähigkeit des Endgerätes. In der vorliegenden Arbeit werden unterschiedlich bestrahlte Proben, nämlich einmal mit Elektronen und einmal mit Neutronen unterschiedlicher Energie und mit unterschieldichen Bestrahlungsdosen, analysiert. Aus den Messungen bei Raumtemperatur und in einem Magnetfeld von 15 mT entlang der c-Achse werden die T_1 und T_2 Relaxationszeiten extrahiert.

Bei den elektronenbestrahlten Proben bleibt T_1 bei circa 300 µs, während die T_2 Zeit für Defektkonzentrationen über $\sim 4 \cdot 10^{14}\,\mathrm{cm}^{-3}$ linear abnimmt. Die Probe mit der höchsten Bestrahlungsdosis weicht sowohl für T_1 als auch für T_2 weiter nach unten ab. Der Grund hierfür ist vermutlich der erhöhte Kristallschaden. Die Elektronenenergie scheint keine Auswirkung zu haben, außer der erwarteten Änderung der Defektdichte.
Die T_1 und T_2 Zeiten der neutronenbestrahlten Proben sind signifikant kürzer als für die Elektronenbestrahlten mit ähnlicher erzeugten Defektdichte. Das weist auf eine höhere Beschädigung der Kristallstruktur durch die im Querschnitt größeren Neutronen und auch auf die erhöhte Erzeugung von anderen, nicht lumineszenten, paramagnetischen Defekten hin.
Allgemein kann die Schlussfolgerung gezogen werden, dass die Bestrahlung mit Elektronen der mit Neutronen vorzuziehen ist und eine erzeugte Defektdichte unter $2.6 \cdot 10^{15}\,\mathrm{cm}^{-3}$ das optimale Verhältnis zwischen der Kohärenz und der Signalintensität gewährleistet.
Anschliessend wird eine Methode zur substantiellen Verlängerung der T_2 Kohärenzzeit durch das locking der Spinpolarisation mit der Carr-Purcell-Meiboom-Gill (CPMG) Pulssequenz durchgeführt. Mit dieser Sequenz wird der Einfluss der umgebenden ^{29}Si und ^{13}C Kernspins und anderer Störstellen auf die V_{Si} Elektronenspins minimiert. Die CPMG Sequenz hält zwar nur eine Spinkomponente aufrecht, die extrahierte T_2 Zeit dient jedoch als das Ideallimit für die Erhaltung eines beliebigen Quantenzustandes [133].
Dadurch wird die T_2 Kohärenzzeit einer Spinkomponente bei Raumtemperatur und in einem Magnetfeld von 15 mT auf bis zu (230 ± 30) µs verlängert. Bei 17 K erhält man durch die Anwendung dieser Sequenz eine spin-locking Zeitspanne von (75 ± 35) ms mit der geschätzt erreichbaren Kohärenz von ~ 300 ms.
Während dieser Wert sehr nahe an den Richtwert eines NV-Zentrums im hochreinen, mit ^{12}C angereicherten Diamantkristall herankommt, muss erwähnt werden, dass die hier vorgestellten Resultate aus Messungen an einem industriell erhältlichen SiC Wafer ohne jegliche Isotoppurifikation gewonnen werden.
Alles in allem wird durch das Ausarbeiten mehrerer Quantummetrologie Techniken, durch das Aufklären der wahren eneregetischen Struktur der C_{3v} Symmetrie, durch die Bestimmung der Kohärenzeigenschaften in Abhängigkeit an die Umgebungsbedingungen, als auch an die Bestrahlung und schließlich durch das Ausdehnen der Kohärenzzeit auf mindestens 75 Millisekunden, das außerordentliche Potential der V_{Si} Defekte in SiC in Zukunft das Feld der Quantenmetrologie mitzugestalten, eindeutig legitimiert.

Bibliography

[1] F. Jelezko and J. Wrachtrup. Single defect centres in diamond: A review. *Phys. Stat. Sol*, **203**, 13, 3207 (2006). doi: 10.1002/pssa.200671403.

[2] G. Balasubramanian, P. Neumann, D. Twitchen, M. Markham, R. Kolesov, N. Mizuochi, J. Isoya, J. Achard, J. Beck, J. Tissler, V. Jacques, P. R. Hemmer, F. Jelezko and J. Wrachtrup. Ultralong spin coherence time in isotopically engineered diamond. *Nat. Mat.*, **8**, 383 (2009). doi: 10.1038/nmat2420.

[3] F. Jelezko, T. Gaebel, I. Popa, A. Gruber and J. Wrachtrup. Observation of Coherent Oscillations in a Single Electron Spin. *Phys. Rev. Lett.*, **92**, 7, 076401 (2004). doi: 10.1103/PhysRevLett.92.076401.

[4] N. Bar-Gill, L. M. Pham, A. Jarmola, D. Budker and R. L. Walsworth. Solid-state electronic spin coherence time approaching one second. *Nat. Comm.*, **4**, 1743 (2013). doi: 10.1038/ncomms2771.

[5] A. Gruber, A. Draebenstedt, C. Tietz, L. Fleury, J. Wrachtrup and C. von Borczyskowski. Scanning Confocal Optical Microscopy and Magnetic Resonance on Single Defect Centers. *Science*, **276**, 2012 (1997). doi: 10.1126/science.276.5321.2012.

[6] J. R. Maze, P. L. Stanwix, J. S. Hodges, S. Hong, J. M. Taylor, P. Cappellaro, L. Jiang, M. V. Gurudev Dutt, E. Togan, A. S. Zibrov, A. Yacoby, R. L. Walsworth and M. D. Lukin. Nanoscale magnetic sensing with an individual electronic spin in diamond. *Nature*, **455**, 7213, 644 (2008). doi: 10.1038/nature07279.

[7] J. M. Taylor, P. Cappellaro, L. Childress, L. Jiang, D. Budker, P. R. Hemmer, A. Yacoby, R. Walsworth and M. D. Lukin. High-Sensitivity Diamond Magnetometer with Nanoscale Resolution. *Nat. Phys.*, **4**, October, 810 (2008). doi: 10.1038/nphys1075.

[8] G. Balasubramanian, I. Y. Chan, R. Kolesov, M. Al-Hmoud, J. Tisler, C. Shin, C. Kim, A. Wojcik, P. R. Hemmer, A. Krueger, T. Hanke, A. Leitenstorfer, R. Bratschitsch, F. Jelezko and J. Wrachtrup. Nanoscale Imaging Magnetometry With Diamond Spins Under Ambient Conditions. *Nature*, **455**, 648 (2008). doi: 10.1038/nature07278.

[9] J.-I. Chao, E. Perevedentseva, P.-H. Chung, K.-K. Liu, C.-Y. Cheng, C.-C. Chang and C.-L. Cheng. Nanometer-Sized Diamond Particle as a Probe for Biolabeling. *Biophys. J.*, **93**, 6, 2199 (2007). doi: 10.1529/biophysj.107.108134.

[10] A. Krueger. New Carbon Materials: Biological Applications of Functionalized Nanodiamond Materials. *Chem. Eur. J.*, **14**, 5, 1382 (2008). doi: 10.1002/chem.200700987.

[11] T. M. Babinec, B. J. Hausmann, M. Khan, Y. Zhang, J. R. Maze, P. R. Hemmer and M. Loncar. A Diamond Nanowire Single-Photon Source. *Nat. Nanotech.*, **5**, 195 (2010). doi: 10.1038/nnano.2010.6.

[12] D. DiVincenzo. Quantum bits: Better than excellent. *Nat. Mat.*, **9**, 468 (2010). doi: 10.1038/nmat2774.

[13] H. Jagodzinski. Eindimensionale Fehlordnung in Kristallen und ihr Einfluss auf die Roentgeninterferenzen. *Acta Cryst.*, **2**, 201 (1949). doi: 10.1107/S0365110X49000552.

[14] P. G. Baranov, A. P. Bundakova, A. A. Soltamova, S. B. Orlinski, I. V. Borovykh, R. Zondervan, R. Verberk and J. Schmidt. Silicon vacancy in SiC as a promising quantum system for single-defect and single-photon spectroscopy. *Phys. Rev. B*, **83**, 125203 (2011). doi: 10.1103/PhysRevB.83.125203.

[15] W. F. Koehl, B. B. Buckley, F. J. Heremans, G. Calusine and D. D. Awschalom. Room temperature coherent control of defect spin qubits in silicon carbide. *Nature*, **479**, 84 (2011). doi: 10.1038/nature10562.

[16] D. J. Christle, A. L. Falk, P. Andrich, P. V. Klimov, J. U. Hassan, N. T. Son, E. Janzen, T. Ohshima and D. D. Awschalom. Isolated electron spins in silicon carbide with millisecond coherence times. *Nat. Mat.*, **14**, 160 (2015). doi: 10.1038/nmat4144.

[17] M. Widmann, S.-Y. Lee, T. Rendler, N. T. Son, H. Fedder, S. Paik, L. P. Yang, N. Zhao, S. Yang, I. Booker, A. Denisenko, M. Jamali, S. A. Momenzadeh, I. Gerhardt, T. Ohshima, A. Gali, E. Janzen and J. Wrachtrup. Coherent Control of Single Spins in Silicon Carbide at Room Temperature. *Nat. Mat.*, **14**, 164 (2014). doi: 10.1038/NMAT4145.

[18] S. Castelletto, B. C. Johnson, V. Ivady, N. Stavrias, T. Umeda, A. Gali and T. Ohshima. A Silicon Carbide Room-Temperature Single-Photon Source. *Nat. Mat.*, **12**, 11 (2013). doi: 10.1038/NMAT3806.

[19] F. Fuchs, B. Stender, M. Trupke, D. Simin, J. Pflaum, V. Dyakonov and G. V. Astakhov. Engineering Near-Infrared Single-Photon Emitters with Optically Active Spins in Ultrapure Silicon Carbide. *Nat. Comm*, **6**, 7578 (2015). doi: 10.1038/ncomms8578.

[20] D. Riedel, F. Fuchs, H. Kraus, S. Vaeth, A. Sperlich, V. Dyakonov, A. A. Soltamova, P. G. Baranov, V. A. Ilyin and G. V. Astakhov. Resonant Addressing and Manipulation of Silicon Vacancy Qubits in Silicon Carbide. *Phys. Rev. Lett.*, **109**, 226402 (2012). doi: 10.1103/PhysRevLett.109.226402.

[21] H. Kraus, V. A. Soltamov, D. Riedel, S. Vaeth, F. Fuchs, A. Sperlich, P. G. Baranov, V. Dyakonov and G. V. Astakhov. Room Temperature Quantum Microwave Emitters Based on Spin Defects in Silicon Carbide. *Nat. Phys.*, **10**, 12 (2013). doi: 10.1038/NPHYS2826.

[22] H. Kraus, V. A. Soltamov, F. Fuchs, D. Simin, A. Sperlich, P. G. Baranov, G. V. Astakhov and V. Dyakonov. Magnetic Field and Temperature Sensing with Atomic-Scale Spin Defects in Silicon Carbide. *Sci. Rep.*, **4**, 5303 (2014). doi: 10.1038/srep05303.

[23] E. G. Acheson. Production of Artificial Crystalline Carbonaceous Materials. *US Patent*, **492767** (1893).

[24] H. Moissan. Nouvelles recherches sur la meteorite de Canon Diablo. *Comptes rendus*, 773–786 (1904).

[25] S. P. Yoon, editor. *SiC Materials and Devices*, volume 52 of *Semiconductors and Semimetals*. Academic Press (1998).

[26] http://www.sglgroup.com/cms/international/products/product-groups/cc/carbon-ceramic-brake-disks/index.html?__locale=en/.

[27] K. Shenai, R. S. Scott and B. J. Baliga. Optimum Semiconductors for High-Power Electronics . *IEEE Trans. on El. Dev.*, **36**, 9, 1811 (1989). doi: 10.1109/16.34247.

[28] W. Puff, M. Boumerzoug, J. Brown, P. Mascher, D. Macdonald, P. J. Simpson, A. G. Balogh, H. Hahn, W. Chang and M. Rose. An Investigation of Point Defects in Silicon Carbide. *App. Phys. A*, **61**, 55 (1995). doi: 10.1007/BF01538211.

[29] http://www.esa.int/Our_Activities/Space_Science/The_largest_telescope_mirror_ever_put_into_space/.

[30] N. Ohtani, M. Katsuno, T. Fujimoto, H. Tsuge, T. Aigo and H. Yashiro. Large High-Quality Silicon Carbide Substrates. *Nippon Steel Technical Report*, **84**, 36 (2001).

[31] S. Davis. Schottky Diodes: the Old Ones Are Good, the New Ones Are Better. *Pow. El. Tech.*, **March**, 36 (2011).

[32] F. Shimura. *Semiconductor Silicon Crystal Technology*. Academic Press (1989).

[33] M. A. White. *Physical Properties of Materials, Second Edition*. CRC Press (2011).

[34] W. Y. Ching, Y.-N. Xu, P. Rulis and L. Ouyang. The Electronic Structure and Spectroscopic Properties of 3C, 2H, 4H, 6H, 15R and 21R polymorphs of SiC. *Mat. Sci. and Eng. A*, **422**, 147 (2006). doi: 10.1016/j.msea.2006.01.007.

[35] L. S. Ramsdell. Studies on Silicon Carbide. *Am. Min.*, **32**, 64 (1947).

[36] A. L. Falk, B. B. Buckley, G. Calusine, W. F. Koehl, V. V. Dobrovitski, A. Politi, C. A. Zorman, P. X. L. Feng and D. D. Awshalom. Polytype Control of Spin Qubits in Silicon Carbide. *Nat. Comm.*, **4**, 1819 (2013). doi: 10.1038/ncomms2854.

[37] E. Soerman, N. T. Son, W. M. Chen, O. Kordina, C. Hallin and E. Janzen. Silicon Vacancy Related Defect in 4H and 6H SiC. *Phys. Rev. B*, **61**, 4, 2613 (2000). doi: 10.1103/PhysRevB.61.2613.

[38] P. G. Neudeck. Electrical Impact of SiC Structural Crystal Defects on High Electric Field Devices. *Mat. Sci. For.*, **338-342**, 1161 (2000). doi: 10.4028/www.scientific.net/MSF.338-342.1161.

[39] J. P. Bergman, L. Storasta, F. H. C. Carlsson, S. Sridhara, B. Magnusson and E. Janzen. Defects in 4H silicon carbide. *Phys. B*, **308-310**, 675 (2001). doi: 10.1016/S0921-4526(01)00790-6.

[40] I. G. Ivanov, C. Hallin, A. Henry, O. Kordina and E. Janzen. Nitrogen Doping Concentration as Determined by Photoluminescence in 4H- and 6H-SiC. *J. of App. Phys.*, **80**, 6, 3504 (1996). doi: 10.1063/1.363221.

[41] F. Demichelis, C. F. Pirri and E. Tresso. Influence of Doping on the Structural and Optoelectronic Properties of Amorphous and Microcrystalline Silicon Carbide. *J. App. Phys.*, **72**, 4, 1327 (1992). doi: 10.1063/1.351742.

[42] J. Schneider and K. Maier. Point Defects in Silicon Carbide. *Phys. B*, **185**, 1-4, 199 (1993). doi: 10.1016/0921-4526(93)90237-Z.

[43] H. Itoh, A. Kawasuso, T. Ohshima, M. Yoshikawa, I. Nashiyama, S. Tanigawa, S. Misawa, H. Okumura and S. Yoshida. Intrinsic Defects in Cubic Silicon Carbide. *Phys. Stat. Sol.*, **162**, 173 (1997). doi: 10.1002/1521-396X(199707)162:1<173::AID-PSSA173>3.0.CO;2-W.

[44] P. Friedrichs, T. Kimoto, L. Ley and G. Pensl. *Silicon Carbide*, volume 1. Wiley-VCH (2010).

[45] D. Nakamura, I. Gunjishima, S. Yamaguchi, T. Ito, A. Okamoto, H. Kondo, S. Onda and K. Takatori. Ultrahigh-Quality Silicon Carbide Single Crystals. *Nature*, **430**, 1009 (2004). doi: 10.1038/nature02810.

[46] A. Krueger. Beyond the Shine: Recent Progress in Applications of Nanodiamond. *J. of Mat. Chem.*, **21**, 12571 (2011). doi: 10.1039/c1jm11674f.

[47] R. Yakimova, R. M. Petoral Jr., G. R. Yazdi, C. Vahlberg, A. L. Spetz and K. Uvdal. Surface Functionalization and Biomedical Applications Based on SiC. *J. of Phys. D*, **40**, 20, 6435 (2007). doi: 10.1088/0022-3727/40/20/S20.

[48] B. Somogyi, V. Zolyomi and A. Gali. Near-Infrared Luminescent Cubic Silicon Carbide Nanocrystals for in Vivo Biomarker Spplications: an ab Initio Study. *Nanoscale*, **4**, 7720 (2012). doi: 10.1039/c2nr32442c.

[49] D. Beke, Z. Szekrenyes, D. Palfi, G. Rona, I. Balogh, P. A. Maak, G. Katona, Z. Czigany, K. Kamaras, B. Rozsa, L. Buday, B. Vertessy and A. Gali. Silicon Carbide Quantum Dots for Bioimaging. *J. of Mat. Res.*, **28**, 205 (2012). doi: 10.1557/jmr.2012.296.

[50] A. Kuhn, M. Hennrich and G. Rempe. Deterministic Single-Photon Source for Distributed Quantum Networking. *Phys. Rev. Lett.*, **89**, 067901 (2002). doi: 10.1103/PhysRevLett.89.067901.

[51] E. Knill, R. Laflamme and G. J. Milburn. A Scheme for Efficient Quantum Computation with Linear Optics. *Nature*, **409**, 46 (2001). doi: 10.1038/35051009.

[52] J. Isoya, T. Umeda, N. Mizuochi, N. T. Son, E. Janzen and T. Ohshima. EPR Identification of Intrinsic Defects in SiC. *Phys. Stat. Sol.*, **245**, 7, 1298 (2008). doi: 10.1002/pssb.200844209.

[53] A. Gali. Excitation Properties of Silicon Vacancy in Silicon Carbide. *Mat. Sci. For.*, **717-720**, 255 (2012). doi: 10.4028/www.scientific.net/MSF.717-720.255.

[54] E. Condon. A Theory of Intensity Distribution in Band Systems. *Phys. Rev.*, **28**, 6, 1182 (1926). doi: 10.1103/PhysRev.28.1182.

[55] T. Wimbauer, B. K. Meyer, A. Hofstaetter, A. Scharmann and H. Overhof. Negatively charged Si vacancy in 4H SiC: A comparison between theory and experiment. *Phys. Rev. B*, **56**, 12, 7384 (1997). doi: 10.1103/PhysRevB.56.7384.

[56] N. Mizuochi, S. Yamasaki, H. Takizawa, N. Morishita, T. Ohshima, H. Itoh and J. Isoya. Continuous-Wave and Pulsed EPR Study of the Negatively Charged Silicon Vacancy with S = 3/2 and C3v Symmetry in n-type 4H-SiC. *Phys. Rev. B*, **66**, 235202 (2002). doi: 10.1103/PhysRevB.66.235202.

[57] P. G. Baranov, V. A. Soltamov, A. A. Soltamova, G. V. Astakhov and V. D. Dyakonov. Point Defects in SiC as a Promising Basis for Single-Defect, Single-Photon Spectroscopy with Room Temperature Controllable Quantum States. *Mat. Sci. For.*, **740-742**, 425 (2013). doi: 10.4028/www.scientific.net/MSF.740-742.425.

[58] L. Torpo, M. Marlo, T. E. M. Staab and R. M. Nieminen. Comprehensive ab Initio Study of Properties of Monovacancies and Antisites in 4H-SiC. *J. Phys.*, **13**, 6203 (2001).

[59] O. O. Soykal, P. Dev and S. E. Economou. Silicon Vacancy Center in 4H-SiC: Electronic Structure and Spin-Photon Interfaces. *Phys. Rev. B*, **93**, 081207 (2016). doi: 10.1103/PhysRevB.93.081207.

[60] S. B. Orlinski, J. Schmidt, E. N. Mokhov and P. G. Baranov. Silicon and Carbon Vacancies in Neutron-Irradiated SiC: A High-Field Electron Paramagnetic Resonance Study. *Phys. Rev. B*, **67**, 125207 (2003). doi: 10.1103/PhysRevB.67.125207.

[61] L. D. Landau and E. M. Lifshitz. *Quantum Mechanics: Non-Relativistic Theory*, volume 3. Elsevier (1981).

[62] H. Kraus. Optically Detected Magnetic Resonance on Organic and Inorganic Carbon-Based Semiconductors. Ph.D. thesis, University of Würzburg (2014).

[63] P. Zeeman. Ueber einen Einfluss der Magnetisirung auf die Natur des von einer Substanz emittirten Lichtes. *Verh. der Phys. Ges. zu Ber.*, **15**, 1, 127 (1896).

[64] K. Jensen, V. M. Acosta, A. Jarmola and D. Budker. Light Narrowing of Magnetic Resonances in Ensembles of Nitrogen-Vacancy Centers in Diamond. *Phys. Rev. B*, **87**, 014115 (2013). doi: 10.1103/PhysRevB.87.014115.

[65] A. M. Tyryshkin, S. Tojo, J. J. L. Morton, H. Riemann, N. V. Abrosimov, P. Becker, H. J. Pohl, T. Schenkel, M. L. W. Thewalt, K. M. Itoh and S. A. Lyon. Electron Spin Coherence Exceeding Seconds in High Purity Silicon. *Nat. Mat.*, **11**, 2, 143 (2012). doi: 10.1038/nmat3182.

[66] R. A. Frosch and H. M. Foley. Magnetic Hyperfine Structure in Diatomic Molecules. *Phys. Rev.*, **88**, 6, 1337 (1952). doi: 10.1103/PhysRev.88.1337.

[67] D. Simin. Vektormagnetometrie mit Punktdefekten in Siliciumcarbid. Master's thesis, University Würzburg (2014).

[68] R. A. Graaf. *In Vivo NMR Spectroscopy, 2nd Edition*. Wiley (2007).

[69] L. R. Liboff. *Introductory Quantum Mechanics, Fourth Edition*. Addison Wesley (2003).

[70] F. Fuchs. Optical Spectroscopy on Silicon Vacancy Defects in Silicon Carbide. Ph.D. thesis, University of Würzburg (2015).

[71] Honeywell 3-Axis Digital Compass IC HMC5883L Handbuch (2013).

[72] E. H. Hall. On a New Action of the Magnet on Electric Currents. *Am. J. of Math.*, **2**, 3, 287 (1879). doi: 10.2307/2369245.

[73] J. Janisch. Kleiner Effekt - Grosse Wirkung. *El. Ind.*, **7**, 2 (2006).

[74] D. Diaz-Michelena. Small Magnetic Sensors for Space Applications. *Sensors*, **9**, 2271 (2009). doi: 10.3390/s90402271.

[75] R. S. Popovic, J. A. Flanagan and P. A. Besse. The Future of Magnetic Sensors. *Sen. and Act. A*, **56**, 39 (1996). doi: 10.1016/0924-4247(96)01285-X.

[76] C. Degen. Nanoscale Magnetometry: Microscopy with Single Spins. *Nat. Nano.*, **3**, November, 643 (2008). doi: 10.1038/nnano.2008.328.

[77] J. Clarke and A. I. Braginski. *The SQUID Handbook: Fundamentals and Technology of SQUIDs and SQUID Systems*. Wiley (2006).

[78] C.-H. Hsieh, C.-L. Dai and M.-Z. Yang. Fabrication and Characterization of CMOS-MEMS Magnetic Microsensors. *Sensors*, **13**, 11, 14728 (2013). doi: 10.3390/s131114728.

[79] B. M. Chernobrod and G. P. Berman. Spin Microscope Based on Optically Detected Magnetic Resonance. *J. of App. Phys.*, **97**, 14903 (2005). doi: 10.1063/1.1829373.

[80] K. M. Itoh. Quantum-Assisted Sensing Using Nitrogen-Vacancy (NV) Centers in Diamond. *AAPPS*, **25**, 1 (2015).

[81] S.-Y. Lee, M. Niethammer and J. Wrachtrup. Vector Magnetometry based on S = 3/2 Electronic Spins. *Phys. Rev. B*, **92**, 115201 (2015). doi: 10.1103/PhysRevB.92.115201.

[82] P. A. M. Dirac. The Quantum Theory of the Emission and Absorption of Radiation. *Proceedings of the Royal Society A*, **114**, 767, 243 (1927).

[83] D. Simin, F. Fuchs, H. Kraus, A. Sperlich, P. G. Baranov, G. Astakhov and V. Dyakonov. High-Precision Angle-Resolved Magnetometry with Uniaxial Quantum Centers in Silicon Carbide. *Phys. Rev. Appl.*, **4**, 14009 (2015). doi: 10.1103/PhysRevApplied.4.014009.

[84] M. Bydder, A. Rahal, G. D. Fullerton and G. M. Bydder. The Magic Angle Effect: A Source of Artifact, Determinant of Image Contrast, and Technique for Imaging. *J. Magn. Reson. Im.*, **25**, 2, 290 (2007). doi: 10.1002/jmri.20850.

[85] J. Michl, T. Teraji, S. Zaiser, I. Jakobi, G. Waldherr, F. Dolde, P. Neumann, M. W. Doherty, N. B. Manson, J. Isoya and J. Wrachtrup. Perfect Alignment and Preferential Orientation of Nitrogen-Vacancy Centers during Chemical Vapor Deposition Diamond Growth on (111) Surfaces. *Appl. Phys. Lett.*, **104**, 102407 (2014). doi: 10.1063/1.4868128.

[86] M. Lesik, J. P. Tetienne, A. Tallaire, J. Achard, V. Mille, A. Gicquel, J. F. Roch and V. Jacques. Perfect Preferential Orientation of Nitrogen-Vacancy Defects in a Synthetic Diamond Sample. *Appl. Phys. Lett.*, **104**, 113107 (2014). doi: 10.1063/1.4869103.

[87] S. Y. Karpov, A. V. Kulik, I. A. Zhmakin, Y. N. Makarov, E. N. Mokhov, M. G. Ramm, M. S. Ramm, A. D. Roenkov and Y. A. Vodakov. Analysis of Sublimation Growth of Bulk SiC Crystals in Tantalum Container. *J. Cryst. Growth*, **211**, 347 (2000). doi: 10.1016/S0022-0248(99)00787-3.

[88] E. van Oort and M. Glasbeek. Fluorescence Detected Level-Anticrossing and Spin Coherence of a Localized Triplet State in Diamond. *Chem. Phys.*, **152**, 3, 365 (1991). doi: 10.1016/0301-0104(91)85011-5.

[89] J. P. D. Martin, N. B. Manson, D. C. Doetschman, M. J. Sellars, R. Neuhaus and E. Wilson. Spectral Hole Burning and Raman Heterodyne Signals Associated with an Avoided Crossing in the NV Centre in Diamond. *J. of Lumin.*, **86**, 3-4, 355 (2000). doi: 10.1016/S0022-2313(00)00179-4.

[90] P. G. Baranov and N. G. Romanov. Magnetic Resonance in Micro- and Nanostructures. *Appl. Magn. Res.*, **21**, 2, 165 (2001). doi: 10.1007/BF03162450.

[91] R. J. Epstein, F. M. Mendoza, Y. K. Kato and D. D. Awschalom. Anisotropic Interactions of a Single Spin and Dark-Spin Spectroscopy in Diamond. *Nat. Phys.*, **1**, 94 (2005). doi: 10.1038/nphys141.

[92] L. J. Rogers, R. L. McMurtrie, M. J. Sellars and N. B. Manson. Time-Averaging within the Excited State of the Nitrogen-Vacancy Centre in Diamond. *New J. of Phys.*, **11**, 63007 (2009). doi: 10.1088/1367-2630/11/6/063007.

[93] J. P. Tetienne, L. Rondin, P. Spinicelli, M. Chipaux, T. Debuisschert, J. F. Roch and V. Jacques. Magnetic- Field-Dependent Photodynamics of Single NV Defects in Diamond: An Application to Qualitative All-Optical Magnetic Imaging. *New J. of Phys.*, **14**, 103033 (2012). doi: 10.1088/1367-2630/14/10/103033.

[94] G. L. Bir and G. E. Pikus. *Symmetry and Strain-Induced Effects in Semiconductors*. Wiley (1974).

[95] D. Simin, V. A. Soltamov, A. V. Poshakinskiy, A. N. Anisimov, R. A. Babunts, D. O. Tolmachev, E. N. Mokhov, M. Trupke, S. A. Tarasenko, A. Sperlich, P. G. Baranov, V. Dyakonov and G. V. Astakhov. All-Optical dc Nanotesla Magnetometry Using Silicon Vacancy Fine Structure in Isotopically Purified Silicon Carbide. *Phys. Rev. X*, **6**, 31014 (2016). doi: 10.1103/PhysRevX.6.031014.

[96] N. S. Averkiev, V. M. Asnin, Y. N. Lomasov, G. E. Pikus, A. A. Rogachev and N. A. Rud. Radiation Polarization of a Coupled Exciton in Ge(As) in a Longitudinal Magnetic Field. *Sov. Phys. Solid State*, **23**, 1851 (1981).

[97] M. V. Durnev, M. M. Glazov, E. L. Ivchenko, M. Jo, T. Mano, T. Kuroda, K. Sakoda, S. Kunz, G. Sallen, L. Bouet, X. Marie, D. Lagarde, T. Amand and B. Urbaszek. Magnetic Field Induced Valence Band Mixing in [111] Grown Semiconductor Quantum Dots. *Phys. Rev. B*, **87**, 85315 (2013). doi: 10.1103/PhysRevB.87.085315.

[98] H. Clevenson, M. E. Trusheim, C. Teale, T. Schroeder, D. Braje and D. Englund. Broadband Magnetometry and Temperature Sensing with a Light-Trapping Diamond Waveguide. *Nat. Phys.*, **11**, 393 (2015). doi: 10.1038/NPHYS3291.

[99] T. Wolf, P. Neumann, K. Nakamura, H. Sumiya, T. Ohshima, J. Isoya and J. Wrachtrup. Subpicotesla Diamond Magnetometry. *Phys. Rev. X*, **5**, 41001 (2015). doi: 10.1103/PhysRevX.5.041001.

[100] V. Shah, S. Knappe, P. D. D. Schwindt and J. Kitching. Subpicotesla Atomic Magnetometry with a Microfabricated Vapour Cell. *Nat. Phot.*, **1**, 649 (2007). doi: 10.1038/nphoton.2007.201.

[101] S. H. Kim, J. Noh, M. K. Jeon, K. W. Kim, L. P. Lee and S. I. Woo. Micro-Raman Thermometry for Measuring the Temperature Distribution Inside the Microchannel of a Polymerase Chain Reaction Chip. *J. of Micromech. and Microeng.*, **16**, 526 (2006). doi: 10.1088/0960-1317/16/3/007.

[102] T. Beechem, S. Graham, S. P. Kearney, L. M. Phinney and J. R. Serrano. Simultaneous Mapping of Temperature and Stress in Microdevices Using Micro-Raman Spectroscopy. *Rev. Sci. Inst.*, **78**, 61301 (2007). doi: 10.1063/1.2738946.

[103] G. W. Walker, V. C. Sundar, C. M. Rudzinski, A. W. Wun, M. G. Bawendi and D. G. Nocera. Quantum-Dot Optical Temperature Probes. *Appl. Phys. Lett.*, **83**, 3555 (2003). doi: 10.1063/1.1620686.

[104] F. Vetrone, R. Naccache, A. Zamarron, A. Juarranz de la Fuente, F. Sanz-Rodriguez, L. M. Maestro, E. M. Rodriguez, D. Jaque, J. G. Sole and J. A. Capobianco. Temperature Sensing Using Fluorescent Nanothermometers. *ACS Nano*, **4**, 3254 (2010). doi: 10.1021/nn100244a.

[105] J. S. Donner, S. A. Thompson, M. P. Kreuzer, G. Baffou and R. Quidant. Mapping Intracellular Temperature Using Green Fluorescent Protein. *Nano Lett.*, **12**, 4, 2107 (2012). doi: 10.1021/nl300389y.

[106] L.-P. Yang, C. Burk, M. Widmann, S.-Y. Lee, J. Wrachtrup and N. Zhao. Electron spin decoherence in silicon carbide nuclear spin bath. *Phys. Rev. B*, **90**, 241203 (2014). doi: 10.1103/PhysRevB.90.241203.

[107] Y. Yue and X. Wang. Nanoscale Thermal Probing. *Nano Rev.*, **3**, 11586 (2012). doi: 10.3402/nano.v3i0.11586.

[108] D. M. Toyli, C. F. de las Casas, D. J. Christle, V. V. Dobrovitski and D. D. Awschalom. Fluorescence Thermometry Enhanced by the Quantum Coherence of Single Spins in Diamond. *PNAS*, **110**, 8417 (2013). doi: 10.1073/pnas.1306825110.

[109] P. Neumann, I. Jakobi, F. Dolde, C. Burk, R. Reuter, G. Waldherr, J. Honert, T. Wolf, A. Brunnert, J. H. Shim, D. Suter, H. Sumiya, J. Isoya and J. Wrachtrup. High-Precision Nanoscale Temperature Sensing Using Single Defects in Diamond. *Nano Lett.*, **13**, 6, 2738 (2013). doi: 10.1021/nl401216y.

[110] J. Wang, F. Feng, J. Zhang, J. Chen, Z. Zheng, L. Guo, W. Zhang, X. Song, G. Guo, L. Fan, C. Zou, L. Lou, W. Zhu and G. Wang. High-Sensitivity Temperature Sensing Using an Implanted Single Nitrogen-Vacancy Center Array in Diamond. *Phys. Rev. B*, **91**, 155404 (2015). doi: 10.1103/PhysRevB.91.155404.

[111] V. M. Acosta, E. Bauch, M. P. Ledbetter, A. Waxman, L.-S. Bouchard and D. Budker. Temperature Dependence of the Nitrogen-Vacancy Magnetic Resonance in Diamond. *Phys. Rev. Lett.*, **104**, 70801 (2010). doi: 10.1103/PhysRevLett.104.070801.

[112] T. D. Ladd, F. Jelezko, R. Laflamme, Y. Nakamura, C. Monroe and J. L. OBrien. Quantum computers. *Nature*, **464**, 45 (2010). doi: 10.1038/nature08812.

[113] D. D. Awschalom, L. C. Bassett, A. S. Dzurak, E. L. Hu and J. R. Petta. Quantum Spintronics: Engineering and Manipulating Atom-Like Spins in Semiconductors. *Science*, **339**, 6124, 1174 (2013). doi: 10.1126/science.1231364.

[114] A. Jarmola, V. M. Acosta, K. Jensen, S. Chemerisov and D. Budker. Temperature- and Magnetic-Field-Dependent Longitudinal Spin Relaxation in Nitrogen-Vacancy Ensembles in Diamond. *Phys. Rev. Lett.*, **108**, 197601 (2012). doi: 10.1103/PhysRevLett.108.197601.

[115] A. Abragam and B. Bleaney. *Electron Paramagnetic Resonance of Transition Ions*. OUP Oxford (2012).

[116] S. G. Carter, O. O. Soykal, P. Dev, S. E. Economou and E. R. Glaser. Spin Coherence and Echo Modulation of the Silicon Vacancy in 4H-SiC at Room Temperature. *Phys. Rev. B*, **92**, 161202 (2015). doi: 10.1103/PhysRevB.92.161202.

[117] A. L. Falk, P. V. Klimov, V. Ivady, K. Szasz, D. J. Christle, W. F. Koehl, A. Gali and D. D. Awschalom. Optical Polarization of Nuclear Spins in Silicon Carbide. *Phys. Rev. Lett.*, **114**, 247603 (2015). doi: 10.1103/PhysRevLett.114.247603.

[118] J.-M. Yang, H. Yang and L. Lin. Quantum Dot Nano Thermometers Reveal Heterogeneous Local Thermogenesis in Living Cells. *ACS Nano*, **5**, 6, 5067 (2011). doi: 10.1021/nn201142f.

[119] E. Abe, A. M. Tyryshkin, S. Tojo, J. J. L. Morton, W. M. Witzel, A. Fujimoto, J. W. Ager, E. E. Haller, J. Isoya, S. A. Lyon, M. L. W. Thewalt and K. M. Itoh. Electron spin coherence of phosphorus donors in silicon: Effect of environmental nuclei Eisuke. *Phys. Rev. B*, **82**, 121201 (2010). doi: 10.1103/PhysRevB.82.121201.

[120] http://ati.tuwien.ac.at/reactor/EN/.

[121] J. R. Maze, J. M. Taylor and M. D. Lukin. Electron Spin Decoherence of Single Nitrogen-Vacancy Defects in Diamond. *Phys. Rev. B*, **78**, 94303 (2008). doi: 10.1103/PhysRevB.78.094303.

[122] S. Meiboom and D. Gill. Modified Spin-Echo Method for Measuring Nuclear Relaxation Times. *Rev. of Sci. Instr.*, **29**, 8 (2004). doi: 10.1063/1.1716296.

[123] G. de Lange, Z. H. Wang, D. Riste, V. V. Dobrovitski and R. Hanson. Universal Dynamical Decoupling of a Single Solid-State Spin from a Spin Bath. *Science*, **330**, 60 (2010). doi: 10.1126/science.1192739.

[124] A. J. Rossini, A. Zagdoun, M. Lelli, D. Gajan, F. Rascon, M. Rosay, W. E. Maas, C. Coperet, A. Lesagea and L. Emsley. One hundred fold overall sensitivity enhancements for Silicon-29 NMR spectroscopy of surfaces by dynamic nuclear polarization with CPMG acquisition. *Chem. Sci.*, **3**, 108 (2012). doi: 10.1039/C1SC00550B.

[125] K. Oshio and F. A. Jolesz. Fast MRI by creating multiple spin echoes in a CPMG sequence. *Magn. Res. in Med.*, **30**, 2, 251 (1993). doi: 10.1002/mrm.1910300216.

[126] S. Watanabe, J. Harada, S. Sasaki and Y. Hirayama. Dynamical suppression of nuclear-spin decoherence time in Si and GaAs using inversion pulses. *J. of Magn. and Magn. Mat.*, **310**, 2, 2167 (2007). doi: 10.1016/j.jmmm.2006.11.113.

[127] W. M. Witzel and S. Das Sarma. Multiple-Pulse Coherence Enhancement of Solid State Spin Qubits. *Phys. Rev. Lett.*, **98**, 77601 (2007). doi: 10.1103/PhysRevLett.98.077601.

[128] M. B. Franzoni, P. R. Levstein, J. Raya and J. Hirschinger. Hole burning in polycrystalline C60: An answer to the long pseudocoherent tails. *Phys. Rev. B*, **78**, 115407 (2008). doi: 10.1103/PhysRevB.78.115407.

[129] D. Li, Y. Dong, R. G. Ramos, J. D. Murray, K. MacLean, A. E. Dementyev and S. E. Barrett. Intrinsic origin of spin echoes in dipolar solids generated by strong Pi pulses. *Phys. Rev. B*, **77**, 214306 (2008). doi: 10.1103/PhysRevB.77.214306.

[130] W. Zhang, V. V. Dobrovitski, L. F. Santos, L. Viola and B. N. Harmon. Dynamical control of electron spin coherence in a quantum dot: A theoretical study. *Phys. Rev. B*, **75**, 201302 (2007). doi: 10.1103/PhysRevB.75.201302.

[131] C. D. Ridge, L. F. O'Donnell and J. D. Walls. Long-lived selective spin echoes in dipolar solids under periodic and aperiodic Pi-pulse trains. *Phys. Rev. B*, **89**, 24404 (2014). doi: 10.1103/PhysRevB.89.024404.

[132] Z.-H. Wang, W. Zhang, A. M. Tyryshkin, S. A. Lyon, J. W. Ager, E. E. Haller and V. V. Dobrovitski. Effect of pulse error accumulation on dynamical decoupling of the electron spins of phosphorus donors in silicon. *Phys. Rev. B*, **85**, 85206 (2012). doi: 10.1103/PhysRevB.85.085206.

[133] Z.-H. Wang, G. de Lange, D. Riste, R. Hanson and V. V. Dobrovitski. Comparison of dynamical decoupling protocols for a nitrogen-vacancy center in diamond. *Phys. Rev. B*, **85**, 155204 (2012). doi: 10.1103/PhysRevB.85.155204.

[134] B. Naydenov, F. Dolde, L. T. Hall, C. Shin, H. Fedder, L. C. L. Hollenberg, F. Jelezko and J. Wrachtrup. Dynamical decoupling of a single-electron spin at room temperature. *Phys. Rev. B*, **83**, 81201 (2011). doi: 10.1103/PhysRevB.83.081201.

[135] N. Bar-Gill, L. M. Pham, C. Belthangady, D. Le Sage, P. Cappellaro, J. R. Maze, M. D. Lukin, A. Yacoby and R. Walsworth. Suppression of spin-bath dynamics for improved coherence of multi-spin-qubit systems. *Nat. Comm.*, **3**, 858 (2012). doi: 10.1038/ncomms1856.

[136] J. H. Shim, I. Niemeyer, J. Zhang and D. Suter. Robust dynamical decoupling for arbitrary quantum states of a single NV center in diamond. *Europhys. Lett.*, **99**, 40004 (2012). doi: 10.1209/0295-5075/99/40004.

[137] A. M. Souza, G. A. Alvarez and D. Suter. Robust Dynamical Decoupling for Quantum Computing and Quantum Memory. *Phys. Rev. Lett.*, **106**, 240501 (2011). doi: 10.1103/PhysRevLett.106.240501.

[138] B. H. Brandsen and C. J. Joachain. *Quantum Mechanics, Second Edition*. Prentice Hall (2000).

[139] I. L. Chuang and M. A. Nielsen. Prescription for experimental determination of the dynamics of a quantum black box. *J. of Mod. Phys.*, **44**, 11, 2455 (1997). doi: 10.1080/09500349708231894.

[140] M. Hirose, C. D. Aiello and P. Cappellaro. Continuous dynamical decoupling magnetometry. *Phys. Rev. A*, **86**, 62320 (2012). doi: 10.1103/PhysRevA.86.062320.

[141] M. Loretz, T. Rosskopf and C. L. Degen. Radio-Frequency Magnetometry Using a Single Electron Spin. *Phys. Rev. Lett.*, **110**, 17602 (2013). doi: 10.1103/PhysRevLett.110.017602.

[142] S. Kotler, N. Akerman, Y. Glickman, A. Keselman and R. Ozeri. Single-ion quantum lock-in amplifier. *Nature*, **473**, 61 (2011). doi: 10.1038/nature10010.

[143] H. J. Mamin, M. Kim, M. H. Sherwood, C. T. Rettner, K. Ohno, D. D. Awschalom and D. Rugar. Nanoscale Nuclear Magnetic Resonance with a Nitrogen-Vacancy Spin Sensor. *Science*, **339**, 6119, 557 (2013). doi: 10.1126/science.1231540.

[144] T. Staudacher, F. Shi, S. Pezzagna, J. Meijer, J. Du, C. A. Meriles, F. Reinhard and J. Wrachtrup. Nuclear Magnetic Resonance Spectroscopy on a (5-Nanometer)3 Sample Volume. *Science*, **339**, 6119, 561 (2013). doi: 10.1126/science.1231675.

A. Appendix

Awards and Grants

1. DAAD conference travel grant for the European Conference on Silicon Carbide and Related Materials 2016 (Neos Marmaras, Greece).

2. Wilhelm-Conrad-Roentgen Student Award of the University of Wuerzburg (2014).

Peer Reviewed Publications

1. S. A. Tarasenko, A. V. Poshakinskiy, D. Simin, V. A. Soltamov, E. N. Mokhov, P. G. Baranov, V. Dyakonov and G. V. Astakhov. Spin and optical properties of silicon vacancies in silicon carbide (a review). Submitted to *Phys. Status Solidi B* (2017).

2. D. Simin, H. Kraus, A. Sperlich, T. Ohshima, G. V. Astakhov and V. Dyakonov. Locking of electron spin coherence above 20 ms in natural silicon carbide. *Phys. Rev. B*, **95**, 161201(R) (2017). doi: 10.1103/PhysRevB.95.161201

3. H. Kraus, D. Simin, C. Kasper, Y. Suda, S. Kawabata, W. Kada, T. Honda, Y. Hijikata, T. Ohshima, V. Dyakonov and G. V. Astakhov. 3D Proton Beam Writing of Optically Active Coherent Vacancy Spins in Silicon Carbide. *Nano. Lett.*, **17**, 2865 (2017). doi: 10.1021/acs.nanolett.6b05395

4. D. Simin, V. A. Soltamov, A. V. Poshakinskiy, A. N. Anisimov, R. A. Babunts, D. O. Tolmachev, E. N. Mokhov, M. Trupke, S. A. Tarasenko, A. Sperlich, P. G. Baranov, V. Dyakonov and G. V. Astakhov. All-optical dc nanotesla magnetometry using silicon vacancy fine structure in isotopically purified silicon carbide. *Phys. Rev. X*, **6**, 31014 (2016). doi: 10.1103/PhysRevX.6.031014

5. A. N. Anisimov, D. Simin, V. A. Soltamov, S. P. Lebedev, P. G. Baranov, G. V. Astakhov and V. Dyakonov. Optical thermometry based on level anticrossing in silicon carbide. *Sci. Rep.*, **6**, 33301 (2016). doi: 10.1038/srep33301

6. G. V. Astakhov, D. Simin, V. Dyakonov, B. V. Yavkin, S. B. Orlinskii, I. I. Proskuryakov, A. N. Anisimov, V. A. Soltamov and P. G. Baranov. Spin Centres in SiC for Quantum Technologies. *Appl. Magn. Res.*, **47**, 793 (2016). doi: 10.1007/s00723-016-0800-x

7. D. Simin, F. Fuchs, H. Kraus, A. Sperlich, P. G. Baranov, G. V. Astakhov and V. Dyakonov. High-Precision Angle-Resolved Magnetometry with Uniaxial Quantum Centers in Silicon Carbide. *Phys. Rev. Appl.*, **4**, 14009 (2015). doi: 10.1103/PhysRevApplied.4.014009

8. F. Fuchs, B. Stender, M. Trupke, D. Simin, J. Pflaum, V. Dyakonov and G. V. Astakhov. Engineering near-infrared single-photon emitters with optically active spins in ultrapure silicon carbide. *Nat. Comm.*, **6**, 7578 (2015). doi: 10.1038/ncomms8578

9. V. Dyakonov, H. Kraus, V. A. Soltamov, F. Fuchs, D. Simin, S. Vaeth, A. Sperlich, P. G. Baranov and G. V. Astakhov. Atomic-Scale Defects in Silicon Carbide for Quantum Sensing Applications. *Mat. Sci. For.*, **821-823**, 355 (2015). doi: 10.4028/www.scientific.net/MSF.821-823.355

10. A. Muzha, F. Fuchs, N. V. Tarakina, D. Simin, M. Trupke, V.A. Soltamov, E.N. Mokhov, P. G. Baranov, V. Dyakonov, A. Krueger and G. V. Astakhov. Room-temperature near-infrared silicon carbide nanocrystalline emitters based on optically aligned spin defects. *Appl. Phys. Lett.*, **105**, 243112 (2014). doi: 10.1063/1.4904807

11. H. Kraus, V. A. Soltamov, F. Fuchs, D. Simin, A. Sperlich, P. G. Baranov, G. V. Astakhov and V. Dyakonov. Magnetic field and temperature sensing with atomic-scale spin defects in silicon carbide. *Sci. Rep.*, **4**, 5303 (2014). doi: 10.1038/srep05303

Conference Contributions

1. European Conference on Silicon Carbide and Related Materials (ECSCRM) 2016 (Neos Marmaras, Greece), poster presentation. D. Simin, H. Kraus, A. Sperlich, M. Trupke, T. Ohshima, G. V. Astakhov and V. Dyakonov. Coherence Properties of the Silicon Vacancy in SiC: from Ensemble to Single Defects.

2. DPG SKM spring meeting 2016 (Regensburg, Germany), oral presentation. D. Simin, H. Kraus, A. Sperlich, T. Ohshima, G. V. Astakhov and V. Dyakonov. Spin Coherence Time of Si Vacancies in Silicon Carbide Exceeding One Millisecond.

3. International Conference on Silicon Carbide and Related Materials (ICSCRM) 2015 (Giardini Naxos, Italy), poster presentation. D. Simin, F. Fuchs, A. Sperlich, M. Trupke, G. V. Astakhov and V. Dyakonov. Coherent Spin Manipulation of Si-Vacancies in Silicon Carbide.

4. DPG SKM spring meeting 2015 (Berlin, Germany), oral presentation. D. Simin, A. Sperlich, V. A. Soltamov, P. G. Baranov, G. V. Astakhov and V. Dyakonov. Coherent Spin Manipulation of Si-Vacancies in Silicon Carbide at Ambient Conditions.

5. DPG SKM spring meeting 2014 (Dresden, Germany), oral presentation. D. Simin, F. Fuchs, H. Kraus, V. A. Soltamov, A. Sperlich, P. G. Baranov, G. V. Astakhov and V. Dyakonov. Silicon Vacancies in Silicon Carbide as a Vector Magnetometer.

Danksagung

Die letzte Danksagung ist nun knapp drei Jahre her und die Menschen die ich erwähnen möchte sind größtenteils dieselben. Umso dankbarer bin ich, dass obwohl sie mich nun besser kennen, sie mich trotzdem so großartig unterstützt haben.
Vladimir bin ich sehr dankbar für sein unerschütterliches Vertrauen in meine Fähigkeiten und die Möglichkeit, frei von jeglicher Bevormundung und unnötigem Stress, aufregende Forschung zu betreiben. Und natürlich für das unvergessliche Weinfest, als wir all unser Geld ausgegeben haben. Damit auch ein Dank an **Viktor**, unseren treuen Kollaborateur und bald Kollegen aus Sankt Petersburg, dass er betrunken den Georgy durchgehend Gosha nannte und diesen Abend so witzig machte.
Franzi ist wohl die beste Kollegin die man sich vorstellen kann: obwohl always in a hurry, unendlich hilfsbereit, sowohl bei der Arbeit als auch beim Bier trinken. Nur in unseren Ski Urlauben hätte ich gerne länger geschlafen.
Ein großer Dank an **Hannes** und **Hex** für unbezahlbare Hilfe bei allen Software und Hardware Fragen, die es geschafft haben trotz immensem nerdy wissen eine coole und offene Persönlichkeit zu behalten.
Vielen Dank an alle bei EP6, die diesen Lehrstuhl zu dem machen was er ist. Nämlich ziemlich ziemlich cool. Obwohl der abnehmende Bierkonsum zugunsten von Sport ein bisschen besorgniserregend ist. Aber ich denke Vladimir wird da noch hart durchgreifen.
Vielen Dank an **Kris**, für die spannenden Diskussionen und die Vorbildrolle. Ich bin sehr froh, dass ich meine Zeit bei EP6 mit Dir zusammen verbringen durfte.
Vielen Dank an unseren Partner und Freund **Takeshi**, die gemeinsamen Konferenzen wären ein unvergessliches Erlebnis, wenn die dabei getrunkenen Unmengen Bier nicht den Großteil der Erinnerungen gelöscht hätten. Und natürlich für das Vertrauen in unsere kleine Gruppe und stetigen Nachschub an Proben. Cin-cin!
Vielen Dank an meine Familie, **Liudmila**, **Sergej**, **Nadja** und **Nastja** für stetigen Rückhalt und Freundschaft.
Danke an **Tobi** für alle verpassten Chancen, das Getrunkene und Verzockte.
Danke an **Steffen** für unseren tollen Roadtrip und die vielen vielen Mitternachtsdöner.
Danke an **Andi**, dass ich mal beim Tennis gewinnen durfte.
Danke dir, **Aljona**, dass du die beste Partnerin warst, die ich in meinem Leben haben werde.
Am meisten bin ich **Georgy** dankbar, der mich durch die drei Jahre regelrecht durchgetragen hat. Ohne Dich wäre rein gar nichts von dem hier entstanden und ich schätze mich sehr glücklich Dich als Betreuer gehabt zu haben.